

Soft X-ray Spectroscopic Study of Amino Acid and Salt Solutions



Dissertation zur Erlangung des naturwissenschaftlichen Doktorgrades
der Julius-Maximilians-Universität Würzburg

vorgelegt von

Frank Meyer
aus Würzburg

Würzburg 2015

Eingereicht am: 14.08.2015
bei der Fakultät für Physik und Astronomie

1. Gutachter: Prof. Dr. Friedrich Reinert
2. Gutachter: Prof. Dr. Jean Geurts
der Dissertation

Vorsitzender: Prof. Dr. Matthias Bode
1. Prüfer: Prof. Dr. Friedrich Reinert
2. Prüfer: Prof. Dr. Jean Geurts
3. Prüfer: Prof. Dr. Werner Porod
im Promotionskolloquium

Tag des Promotionskolloquiums: 21.12.2015

Doktorurkunde ausgehändigt am:

TABLE OF CONTENTS

	Page
1 Introduction	1
2 Methodology	5
2.1 X-ray Spectroscopy	5
2.1.1 X-ray Emission Spectroscopy	6
2.1.2 X-ray Absorption Spectroscopy	8
2.1.3 Resonant Inelastic X-ray Scattering	9
2.2 Theoretical Modeling of the Electronic Structure of Molecules and Their X-ray Spectra	11
2.2.1 Density Functional Theory (DFT)	12
2.2.2 Spectra Calculation	17
2.3 Experimental Setup	19
2.3.1 Sample preparations	22
3 X-ray Spectroscopy of Proteinogenic Amino Acid Films and Solutions	25
3.1 Spectral Signature of the Local Electronic Structure of Proteinogenic Amino Acids	28
3.1.1 An XES Building Block Approach on the Electronic Structure of Amino Acids	34
3.1.2 The Building Block Approach Applied to Histidine and Lysine .	44
3.1.3 DFT Calculations of the Electronic Structure of Histidine and Lysine	47
3.1.4 Summary	52
3.2 RIXS study of Proline and Pyrrolidine Solutions	54
3.2.1 Proline Powder	54
3.2.2 The Influence of NaOH and HCl on the Spectrum of Water . . .	60
3.2.3 The Influence of pH on the Electronic Structure of Proline . . .	62
3.2.4 The RIXS Spectra of Pyrrolidine	71
3.2.5 Comparison Between Theory and Experiment	76
3.2.6 Summary	78

TABLE OF CONTENTS

3.3	RIXS Study of Histidine and Imidazole	79
3.3.1	The Influence of pH on the Electronic Structure of Histidine . .	79
3.3.2	The RIXS Spectra of Imidazole	84
3.3.3	Summary	99
4	Ion-Solvation-Induced Molecular Reorganization in Liquid Water	101
4.1	The X-ray Spectra of Liquid Water	103
4.2	Aqueous KCl Solutions	106
4.3	Summary	116
5	Concluding Discussion	119
	Bibliography	129
	Own Publications	149

ABSTRACT

This thesis focuses on the investigation of the electronic structure of amino acids and salts in aqueous solution using X-ray spectroscopic methods. Both material groups are of fundamental importance with regards to many physiological reactions, especially for the Hofmeister effect which describes the solubility of proteins in salt solutions. Hence, the investigation of the electronic structure of amino acids and the influence of ions on the hydrogen bonding network of liquid water are important milestones to a deeper understanding of the Hofmeister series.

Besides investigating the electronic structure of amino acids in aqueous solution, the spectra were used to develop a building block model of the spectral fingerprints of the functional groups and were compared to spectral signatures of suitable reference molecules. In the framework of this thesis, it is shown that the building block approach is a useful tool which allows the interpretation of spectral signatures of considerably more complex molecules.

In this work, the focus lies on the investigation of the occupied and unoccupied electronic states of molecules in solid state, as well as in aqueous solution. Hereby, different X-ray spectroscopic methods were applied. X-ray emission spectroscopy (XES) was used to probe the occupied electronic structure of the solution, while the unoccupied electronic structure was addressed by using X-ray absorption spectroscopy (XAS). Finally, resonant inelastic X-ray scattering (RIXS) as a combination of XAS and XES measurements provides the combined information about the unoccupied and occupied molecular levels. The element specific character of the three measurement methods is a feature which allows the investigation of the local electronic structure of a single functional group. With RIXS, also non-equivalent atoms of the same element can be addressed separately.

Within this thesis firstly, a library of the XE spectra of all 20 proteinogenic amino acids in zwitterionic form is presented. From this sample-set XES fingerprints of the protonated α -amino group NH_3^+ and the deprotonated carboxylic group COO^- were evaluated and used to identify the XES fingerprints of the nitrogen and oxygen containing functional groups of the side chains of the amino acids. The data is discussed based on a building block approach. Furthermore, the XE spectra of the functional groups of lysine and histidine, namely the NH_2 group and the $\text{C}_3\text{N}_2\text{H}_4$ ring structure,

are both compared to XE spectra of suitable reference molecules (imidazole, ammonia and methylamine). It is found that the XE and RIXS spectra of the side chains of lysine and histidine show large similarities to the XE spectra of the reference molecules. This agreement in the XE and RIXS spectra allows a qualitative investigation of XE and RIXS spectra of more complex amino acids using the XE and RIXS spectra of suitable reference molecules.

The chemical structure of histidine and proline is quite different from the structures of the other proteinogenic amino acids. Due to the unique chemical structure of the side chain which in both cases consists of a heterocyclic ring structure, these two amino acids were investigated in more detail. Zubavichus *et al.* [1] have shown that amino acids are decomposing while exposed to X-ray radiation of the experiment. The damage is irreversible and molecular fragments can adsorb on the membrane of the experimental setup. This contamination can also create a spectral signature which then overlaps with the signal of the solution and which complicates the interpretation of the data. To record spectra which are free from contributions of adsorbed molecular fragments on the membrane, the adsorption behavior was investigated.

In contrast to the solid phase in which the amino acids are present as salts in one electronic conformation, the charge state of the amino acids can be manipulated in aqueous solution by tuning the pH-value. By doing this, all possible charge states are accessible (cation, anion, zwitterion). In this work it is shown that also the spectra of the different charge states can be modeled by the spectra of suitable reference molecules using the building block approach. The spectral changes occurring upon protonation and deprotonation of the functional groups are explored and verified by comparing them to theoretical calculations.

The comparison with measurements of pyrrolidine show that the electronic structure which surrounds the nitrogen atom of proline is strongly influenced by the ring structure of the side chain. Furthermore, the proline, pyrrolidine, and histidine molecules are also degrading during the liquid sample measurements. This can be observed by the detection of a new spectral component which increases with the measurement time originating from the window membrane. In all cases, the speed of the agglomeration of molecular fragments at the membrane was observed to be highly sensitive to the pH value of the solution.

To understand the Hofmeister series, also the impact of the salt ions have to be investigated. In this study the influence of potassium chloride (KCl) on the hydrogen bond network of water was studied by using non-resonantly excited XES as well as RIXS. A decreased dissociation of hydrogen molecules and changes in the molecular vibrations could be detected. These changes were interpreted with a molecular reorganization of the water molecules and a decreased number of hydrogen bonds.

ZUSAMMENFASSUNG

Im Rahmen dieser Arbeit werden Untersuchungen zur elektronischen Struktur von verschiedenen Aminosäuren sowohl in wässriger Lösung als auch als Festkörper präsentiert. Das Hauptaugenmerk liegt hierbei auf dem Erlangen eines fundamentalen Verständnisses über die elektronische Struktur der Aminosäuren in wässriger Lösung und der Entwicklung eines Baukastenprinzips für die qualitative Analyse der Röntgenemissions- und resonanten inelastischen Röntgenstreuungsspektren. In dieser Arbeit wird neben Aminosäuren auch der Einfluss von Salzionen auf das dynamische Wasserstoffbrückenbindungsnetzwerk des flüssigen Wassers untersucht. Beide Aspekte stellen wichtige Zwischenschritte auf dem Weg zu einem detaillierten Verständnis des Hofmeister-Effekts dar.

In dieser Arbeit wurden röntgenspektroskopische Methoden verwendet, um die besetzten und unbesetzten Zustände der Moleküle sowohl im Festkörper als auch in wässriger Lösung zu untersuchen. Angewandt wurde dabei die Röntgenabsorptionsspektroskopie (XAS), welche die Untersuchung der unbesetzten Zustände erlaubt. Im Gegensatz dazu liefert die Röntgenemissionsspektroskopie (XES) Informationen über die besetzten Zustände. Die resonante inelastische Röntgenstreuung (RIXS) vereint diese beiden Techniken und enthält Informationen über die gesamte elektronische Struktur eines Systems. Der elementspezifische Charakter dieser Messmethoden muss dabei gesondert hervorgehoben werden, denn dadurch ist es möglich die lokale elektronische Struktur unterschiedlicher funktioneller Gruppen getrennt voneinander zu untersuchen.

Im Rahmen dieser Arbeit wurde zunächst eine Bibliothek der XES-Spektren der zwanzig proteinogenen Aminosäuren angelegt. Daraus konnten spektrale Fingerabdrücke der einzelnen funktionellen Gruppen und der Stickstoff und Sauerstoff enthaltenden Seitenketten der Aminosäuren erstellt werden. Die Spektren der einzelnen funktionellen Gruppen von Lysin und Histidin wurden in einem zweiten Schritt mit den Spektren von kleineren Molekülen, welche die pure funktionelle Gruppe repräsentieren, verglichen. Durch die sehr gute Übereinstimmung konnte gezeigt werden, dass die Röntgenemissionsspektren der untersuchten Aminosäuren nach einem Baukastenprinzip durch die Spektren der kleineren und dadurch einfacheren Referenzmoleküle beschrieben werden können. Mit Hilfe dieses Baukastenprinzips

wurde im weiteren Verlauf dieser Arbeit die detaillierte Untersuchung der elektronischen Struktur der Aminosäuren Prolin und Histidin möglich.

Die Aminosäuren Histidin und Prolin wurden dabei wegen ihrer speziellen chemischen Struktur, welche sich durch eine Ringstruktur an der Seitenkette von der chemischen Struktur der restlichen Aminosäuren unterscheidet, für eine genauere Untersuchung ausgewählt. Sowohl Prolin als auch Histidin werden durch die starke Röntgenstrahlung während des Experiments irreparabel beschädigt, wodurch sich die spektrale Signatur der Moleküle sehr stark ändert. Um diese Beschädigungen zu erkennen und zu vermeiden wurden die Veränderungen der Spektren in Abhängigkeit der Belichtungszeit dokumentiert. Neben Festkörpermessungen, bei welchen die Aminosäuren nur in einer einzigen Konfiguration vorhanden sind (zwitterionisch), wurden die Aminosäuren auch in ihrer natürlichen Umgebung, der wässrigen Lösung, untersucht. Durch die Variation des pH-Wertes der Lösung kann die Konfiguration und damit die elektronische Struktur geändert werden (Kation, Anion, Zwitterion). Eine starke Veränderung in den Spektren in Abhängigkeit des pH-Wertes konnte festgestellt werden. Dabei fällt auf, dass die elektronische Struktur des Stickstoffs in der Aminosäure Prolin sehr stark durch die Ringstruktur der Seitenkette beeinflusst wird, was durch den Vergleich des Spektrums mit dem Spektrum des Pyrrolidin Moleküls gezeigt wurde. Des Weiteren konnte sowohl bei den Flüssigexperimenten mit Prolin als auch mit Histidin eine Kontamination der Membran festgestellt werden, welche durch Molekülfragmente entsteht. Dieser Kontaminierungsprozess konnte für Prolin und Histidin vor allem bei neutralem und hohem pH-Wert beobachtet werden.

Dennoch konnten durch das Baukastenprinzip und die Untersuchungen der Referenzmoleküle Imidazol und Pyrrolidin Erkenntnisse über die elektronische Struktur von Histidin und Prolin gewonnen werden. Mit Hilfe der resonanten inelastischen Röntgenstreuung konnten die spektralen Fingerabdrücke der beiden nicht äquivalenten Stickstoffatome des Imidazols experimentell voneinander getrennt werden. Des Weiteren wurden innerhalb der RIXS-Spektren starke resonante Einflüsse beobachtet. Mit Hilfe von berechneten Spektren von isolierten Imidazol und Imidazolium Molekülen konnten die spektralen Signaturen sowohl im nicht resonanten Spektrum als auch im resonanten Spektrum erklärt werden und im Einzelnen auf die Struktur der Valenzorbitale zurückgeführt werden.

Auf dem Weg zum Verständnis des Hofmeister-Effekts ist neben den Aminosäuren natürlich auch der Einfluss von Salzen auf die Lösung zu berücksichtigen. Im letzten Teil dieser Arbeit stehen daher die Auswirkungen der Ionen des Kaliumchlorids auf das Röntgenemissionsspektrum des Wassers im Fokus. Dazu wurden KCl Lösungen verschiedener Konzentrationen untersucht. Durch die Zugabe von Salz konnte eine Umorientierung der Wassermoleküle und des damit verbundenen Netzwerks von Wasserstoffbrückenbindungen beobachtet werden.

INTRODUCTION

In the last decades, organic and inorganic molecules pushed themselves into technological applications that traditionally were dominated by inorganic solids like solar cells, printable electronics, and light emitting devices. Besides these “new” fields of applications, these molecules are of fundamental interest for catalytic and electrochemical reactions for batteries and fuel cells, corrosion, pharmaceuticals, bio-chemistry, environmental science, and many more [2].

The interest and the growing number of potential applications require a detailed investigation of the structural and electronic properties of these molecules and their interactions with surrounding materials. Since the functionality of these molecules is determined by their geometry and their electronic structure, the investigation of both properties, is important to understand certain reaction pathways in catalytic or electrochemical reactions, or to increase the efficiency of processes in which these molecules are involved.

Although probing the electronic structure of samples in the liquid phase by using spectroscopic techniques challenges the scientific community [3], the investigation of liquids and molecules in their natural environment becomes necessary, which underlines the importance of *in-situ* experiments on these molecules in liquid phase.

In the liquid phase the system is typically much more complex than in gas or solid phase. In gas phase a good assumption is that the individual molecules are not interacting. In solid phase the interactions between the atoms or molecules are more complex, but in most cases the exact positions of the atoms or molecules are known and highly ordered systems can be fabricated. In liquid phase the interactions between the molecules are not as strong as in the solid phase but much stronger than in gas

phase and hence cannot be neglected.

Besides the complexity of the physics, also experimental challenges make it difficult to investigate the electronic structure of samples in liquid phase. In the past decades a lot of effort was devoted to the development of sophisticated setups [3–11] which close the “pressure gap” [3] and hence spectroscopic methods which require ultra high vacuum conditions can be applied. X-ray spectroscopy methods, namely X-ray absorption spectroscopy (XAS), X-ray emission spectroscopy (XES), as well as resonant inelastic X-ray scattering (RIXS), which detect the absorbed and the emitted photons became promising methods.

For the investigation of liquids and solutions, these techniques have two significant advantages over other spectroscopic methods. The inelastic mean free path of these photon-in-photon-out techniques is much larger than that of electron based spectroscopic methods [12]. Due to the increased mean free path of photons, spectra of X-ray spectroscopic methods contain more information about the near-surface and bulk region than electron based spectroscopic methods. Furthermore, the photon-in-photon-out process does not change the local charge state of a system.

The second advantage of X-ray spectroscopic methods is its element selective character. Due to the involvement of core levels which have a characteristic binding energy that is unique for each element, it is possible to selectively excite a single element as well as identify these within the emission spectrum. Additionally, within certain limits, RIXS provides the possibility to distinguish between atoms of the same element in non-equivalent chemical environment. Furthermore, core levels are strongly localized around the atom which creates a spacial sensitivity. Optical spectroscopic methods (far infrared, infrared, visible, and ultraviolet), do not involve the excitation of core levels and hence are neither element selective nor local.

These two advantages make XAS, XES, and RIXS perfect methods to analyze the electronic structure of biological molecules and salts in aqueous solution. Hence these techniques might help to shed light onto the secrets of numerous biological and chemical reactions including the Hofmeister effect [13, 14].

This thesis is organized as follows: in chapter 2, the spectroscopic techniques are briefly explained. Besides the experimental approach also the theoretical calculation of X-ray spectroscopic data is introduced and the fundamental concepts of using Density Functional Theory (DFT) are explained. Chapter 3 and 4 contain the experimental results. In section 3.1 the X-ray spectroscopy is applied to the 20 proteinogenic amino acids. From the comprehensive library, a building block model for the qualitative interpretation of the spectra is derived. The model is compared to theoretical DFT calculations. In section 3.2, the amino acid proline is investigated in more detail both in solid phase and in its natural (aqueous) environment. The spectra are compared to the spectra of pyrrolidine in aqueous solution, a molecule with a very similar structure

which serves as reference molecule for proline. In section 3.3, the investigation is extended to histidine with imidazole as a reference molecule. In chapter 4, influence of ions on the hydrogen bonding network of aqueous water was investigated on the example of potassium chloride (KCl). For this purpose, spectral fingerprints of intact, dissociated, and reorganized water molecules are evaluated. The influence of ultra-fast dissociation on the spectra is identified and used as a sensitive probe which provides information about the hydrogen bonding network of aqueous salt solutions.

METHODOLOGY

2.1 X-ray Spectroscopy

X-ray spectroscopy is widely used for elemental analysis and fundamental research in physics, chemistry, and material science. The chemical sensitivity of X-ray spectra (i.e., chemical shift) [15] was already discovered around 1920. Since then, soft X-ray emission spectroscopy (XES) has been used to study the valence electronic structure of numerous materials. The development of synchrotron radiation, and in particular third generation synchrotron facilities with monochromatic and tunable X-ray sources, allowed selective and resonant excitation as well as X-ray absorption (XAS) experiments, and resulted in a boom for X-ray spectroscopy. The (resonant) combination of both—resonant inelastic X-ray scattering (RIXS)—was first observed by C. Sparks [16], and later by Eisenberger et al. [17]. After the discovery, the RIXS community started to grow. Soft and hard RIXS has become a common tool for the investigation of the electronic structure of numerous systems world wide [2, 18].

With these three methods, X-ray absorption, X-ray emission, and the resonant combination of both (RIXS), the unoccupied and occupied states of a material are accessible. Since this work is focused on the interpretation of molecular systems, the description of the three methods is limited to the effects observable in molecules and the usage of soft X-ray radiation. The applicability of RIXS to other systems and higher photon energies is well reviewed in the article of Rueff and Shukla [19]. The detailed theoretical description of RIXS can be found in the work of Gel'mukhanov *et al.* [20].

The first theoretical description of the absorption and emission of photons was done by Dirac in 1927 [21] and is nowadays known as *Fermi's Golden Rule* [22], which is given below in equation 2.1.

$$(2.1) \quad w_{i \rightarrow f} \propto |\langle f | \mathbf{H}_i | i \rangle|^2 \delta(E_f - E_i \pm h\nu)$$

The transition probability $w_{i \rightarrow f}$ is defined by the square of the absolute value of the inner product of the initial state $|i\rangle$, the interaction operator H_i , and the final state $\langle f|$. The delta function ($\delta(E_f - E_i \pm h\nu)$) ensures the energy conservation. E_f and E_i are the energies of the initial and final states and $h\nu$ is the energy of the participating photon.

The following interaction Hamiltonian describes the interaction of photons with matter.

$$(2.2) \quad \mathbf{H}_i = \frac{e}{mc} \mathbf{p} \cdot \mathbf{A} + \frac{e^2}{2mc^2} \mathbf{A} \cdot \mathbf{A}$$

The $\mathbf{p} \cdot \mathbf{A}$ term describes a one-photon process, as it is also used as interaction Hamiltonian for the absorption and emission process (see 2.1). The $\mathbf{A} \cdot \mathbf{A}$ term on the other hand describes two-photon processes, i.e. diffraction or inelastic scattering. The resonant inelastic X-ray scattering, however, is a coherent two-photon process which is described in the *second order* of the $\mathbf{p} \cdot \mathbf{A}$ term (also used for the description of multiple absorption and emission processes).

In the following, equation 2.1 will be modified to describe the emission and absorption process of X-rays.

2.1.1 X-ray Emission Spectroscopy

X-ray emission spectroscopy (XES) is a method in which the amount of X-ray photons emitted from a sample are measured as a function of their energy (i.e., wavelength, frequency). Prior to the emission of photons, the sample has to be excited into a state of higher energy. This can either be done with the absorption of photons (e.g., X-rays) or, as it was done in the past, via electronic excitation [23–25]. In the following, the excitation will be treated as an independent step, in which a core electron is excited above the vacuum level (ionizing the sample). The subsequent relaxation follows two possible pathways. The faster and dominating process is the Auger decay, for which the core hole is filled by an electron from a higher energy level and the gained energy is used to excite a second electron into the unoccupied states (or above the vacuum level). The second process is the fluorescence decay which generates a photon of an

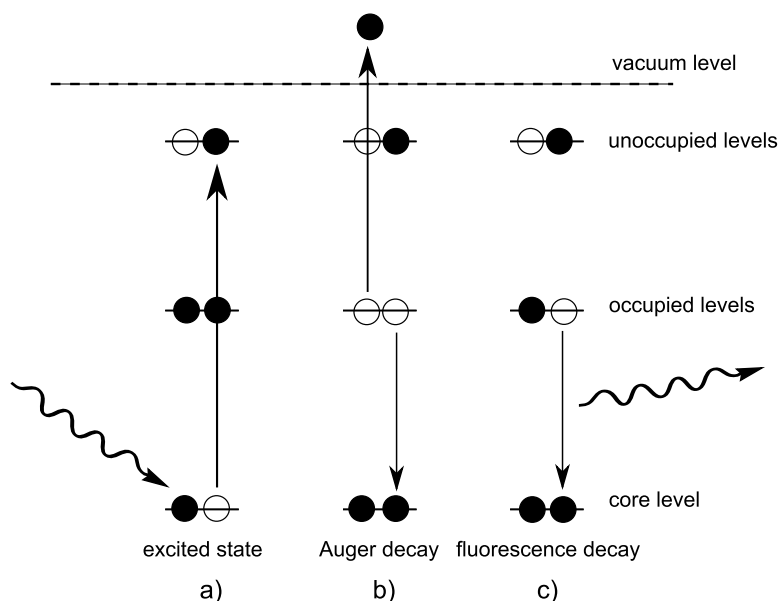


FIGURE 2.1. Schematic drawing of the excited state a), followed by the Auger decay b) creating the electron yield, and the fluorescence decay c) creating the fluorescence yield.

energy according to the energy difference between initial and final state [26, 27]. In the case of soft XES of molecular systems, the initial state $|i\rangle$ is represented by a single ionized molecule with a missing electron in one of the core levels (c^{-1}). Subsequently, a transition occurs from a valence electron level into the empty core electronic level. The final state consists of a molecule with an ionized valence electron level (v^{-1}). Since the core electron levels are strongly bound and therefore localized around the atoms, a strong local character is induced by the core levels. Hence, valence to core transitions are highly sensitive to the valence electronic structure in the direct vicinity of the core. Furthermore, based on the dipole approximation, the perturbation operator H_i induces a set of dipole selection rules imposing restrictions on the states involved. The dipole selection rules impose selectivity with respect to symmetry of the participating levels (orbitals). In molecular systems these orbitals are usually described in terms of a linear combination of atomic orbitals (LCAO). The selective character of X-ray emission spectroscopy offers a possibility to study the *composition* of molecular orbitals of complex multi-atomic compounds with respect to their atomic components [18].

In conclusion, XES contains information about the occupied valence electron levels of a system in the direct vicinity of the excited atom by measuring the energy dependent intensity of the emitted X-rays. Hence, XES is probing the *local partial density of states* (LDOS) in a sample.

2.1.2 X-ray Absorption Spectroscopy

The first absorption spectra were electronically excited and accordingly named inner shell electron energy loss spectroscopy (ISEELS) [28]. At the beginning of the 1980s, the availability of tuneable X-ray sources boosted the investigation of the excitation process and the newly called X-ray absorption spectroscopy (XAS) became a standard tool for investigations in physics, chemistry, and material science. XAS can be divided into the investigation of the *near edge X-ray absorption fine structure* (NEXAFS) and the *extend X-ray absorption fine structure* (EXAFS). In this thesis all XAS experiments are performed in the NEXAFS region.

XAS can be described by Fermi's Golden Rule in the same way as XES, with the difference that X-rays are absorbed and not emitted. Hence, equation 2.1 is still valid and only the initial and final state have to be adjusted. The initial state $|i\rangle$ describes the electronic ground state of the system. The final state $\langle f|$ is thus an excited state in which a core electron is excited into an unoccupied level of the system (c^{-1}, u^1), a so called absorption resonance, or into the vacuum (c^{-1}, e^{-}). The $\delta(E_f - E_i - h\nu)$ term again ensures the energy conservation with E_f and E_i being the energies of the initial and the final states and $h\nu$ the energy of the absorbed photon. The perturbation operator H_i is identical to the XES case and introduces the same dipole selection rules as for XES.

The participation of core levels imposes a strong localization of the transition. Hence, XAS is probing the *local partial unoccupied density of states*.

The recording of an XA spectrum can be done directly or indirectly:

- The most direct way of measuring an XA spectrum is a measurement in *transmission mode*. Hereby, X-rays are shed through a thin sample and the intensity of the beam is measured before and after the sample. This is the most direct measurement but it has the disadvantage that only a limited type of samples are suitable (e.g. the sample has to be very thin, the exact thickness has to be known).
- Alternatively, secondary processes can be used to measure the XAS intensity. In this case, the intensity of decay processes is measured and normalized by the intensity of the initial X-ray beam. Since there are two decay pathways, it is necessary to distinguish between the *fluorescence yield* (FY) XAS and the *electron yield* (EY) XAS (see Fig. 2.1b and c). Both measurement methods can be subdivided once more, whether the entire yield, or only parts are used (total-, partial-yield). The spectra recorded from these indirect methods, especially FY spectra, suffer from spectroscopic artifacts. *Self absorption* also known as *saturation effects* are a very prominent "problem" occurring in FY-XA spectra [12].

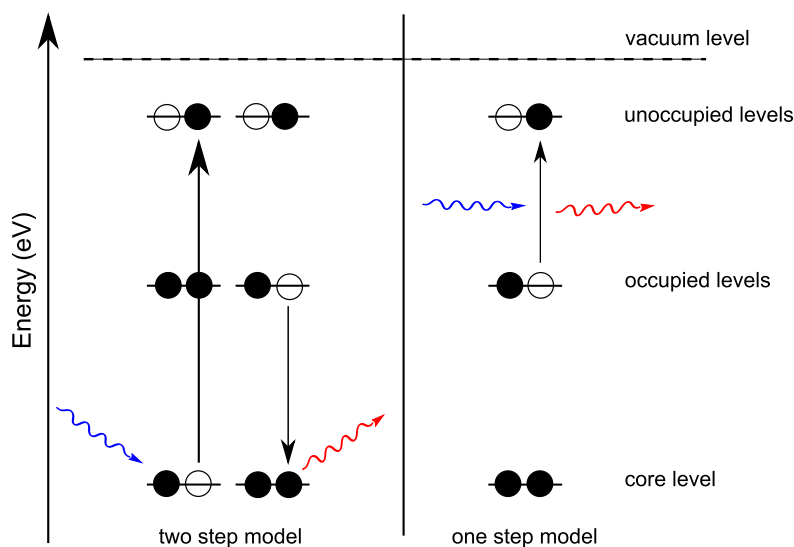


FIGURE 2.2. Schematic drawing of the two step model (left) and the simplified one step model (right).

Yet with FY-XAS and EY-XAS the sample thickness is no longer a limiting factor which allows the investigation of a much wider range of samples is possible.

As seen above, XAS and XES are closely related. However, the nice and illustrative two-step model of an independent absorption and emission processes comes to its limit if the excitation does not ionize the sample. In this case, the absorption and emission processes are coherent and a one-step scattering model has to be considered. In this one-step model, the process is no longer divided into an excitation and a decay process. Moreover, the incident X-ray light is scattered inelastically within the sample. The process is illustrated schematically in Fig. 2.2.

2.1.3 Resonant Inelastic X-ray Scattering

Resonant inelastic X-ray scattering (RIXS) describes the coherent absorption and emission of an X-ray photon within a sample and shows large similarities to Raman spectroscopy and whereby it is sometimes referred to as *Resonant X-ray Raman scattering* [29].

The description of the RIXS process as a scattering process requires second order perturbation theory. The scattering cross section $d\sigma/d\Omega$ of a typical inelastic scattering experiment, in which a photon of energy $h\nu_1$ interacts with a sample and the scattered photon with energy $h\nu_2$ is detected with a spectrometer, can be derived from the Born Oppenheimer approximation [30] and the Kramers-Heisenberg equation [31].

$$\begin{aligned}
 (2.3) \quad \frac{d\sigma}{d\Omega} \propto \sum_f & \left| \langle f | \frac{e^2}{2mc^2} \mathbf{A}_2 \cdot \mathbf{A}_1 | i \rangle \right. \\
 & + \frac{e}{mc} \sum_m \left(\frac{\langle f | \mathbf{p} \cdot \mathbf{A}_2 | m \rangle \langle m | \mathbf{p} \cdot \mathbf{A}_1 | i \rangle}{E_m - E_i - h\nu_1 - i\Gamma_m/2} + \frac{\langle f | \mathbf{p} \cdot \mathbf{A}_1 | m \rangle \langle m | \mathbf{p} \cdot \mathbf{A}_2 | i \rangle}{E_i - E_m + h\nu_2} \right) \Big|^2 \\
 & \cdot \delta(h\nu_1 - h\nu_2 - E_f + E_i)
 \end{aligned}$$

Equation 2.3 can be divided into three terms, each describing a different scattering process. The first term gives rise to the normal elastic scattering also known as Thompson scattering. The second term describes the normal resonant scattering process complying with the ordinary time sequence (absorption before emission). Since the intermediate state is essentially virtual, the non-resonant and time inverted scattering process must also be possible, which is described by the third term. The δ -expression preserves the energy conservation rule.

Focusing on the resonant inelastic scattering term only, equation 2.3 can be rewritten as

$$(2.4) \quad \frac{d\sigma(v_{in})}{dv_{out}d\Omega} \propto \sum_f \sum_m \frac{|\langle f | \mathbf{p} \cdot \mathbf{A}_2 | m \rangle \langle m | \mathbf{p} \cdot \mathbf{A}_1 | i \rangle|^2}{(E_m - E_i - h\nu_1)^2 + \Gamma_m^2/4} \cdot \delta(h\nu_1 - h\nu_2 - E_f + E_i)$$

The uniqueness of this RIXS process lies within the description of the intermediate state. The formula above (2.4) describes the fact that more than one intermediate state can exist and that for a complete description all intermediate states have to be taken into account. This includes the possibility that these intermediate states can interfere with each other, which then can have a large effect on the total scattering cross section. Examples for such effects are the parity selection rules in centro-symmetric systems (molecules) or the preservation of momentum in solid state samples. However, for the sake of a more pictorial representation, the one step model can be described step by step. Note that the step by step picture is only valid if the intermediate and final states are not interfering.

In this step by step picture, the RIXS process consists of an independent absorption and an independent emission process which are both regulated by the dipole operator $\mathbf{p} \cdot \mathbf{A}$ happening on the timescale of the intermediate state Γ_m . The energy of this process has to be conserved, whereby the following equation has to be fulfilled $h\nu_1 - h\nu_2 = E_f - E_i$. Although this step-wise picture is a strong simplification which ignores all interference effects, this picture is able to explain many resonant effects like site-, species-, and symmetry-selection.

Dynamics

As mentioned above and also visible in the RIXS equation 2.4, the process happens on a time scale that is mainly defined by the core hole lifetime. The core hole lifetime of light elements is in the order of several femto seconds (6.6 fs for C 1s, 5.5 fs for N 1s, 3.5 fs for O 1s, and 11.0 fs for S 2p [27]). During this time, the system can react to the excitation (vibrate, dissociate) and the decay characteristics are significantly influenced by the dynamical processes. In this case the core hole lifetime can be seen as a stopwatch for dynamical processes which is the reason it is sometimes referred to as “core hole clock”. By tuning the excitation energy below the resonant condition, the lifetime of the intermediate state decreases [29]. The core hole lifetime introduces a feature to the measurement technique that is usually not accessible by other soft X-ray spectroscopic methods. Spectral feature in the RIXS spectrum which can be related to the time dependency are described in more detail in [32], and in [29]. Observable effects are, e.g., the symmetry-breaking vibronic coupling and the dissociation of the excited molecule.

2.2 Theoretical Modeling of the Electronic Structure of Molecules and Their X-ray Spectra

The theoretical description of molecules and chemical bonds is addressed by quantum chemistry and computational chemistry. The fundamental goal of this field of research is solving the Schrödinger equation with the molecular Hamiltonian which determines the *electronic structure* of a molecular system. The electronic and geometric structure of a molecule is responsible for its chemical properties. An analytical solution for the Schrödinger equation can only be obtained for the hydrogen atom. All other molecular systems consist of more than three particles (i.e. H₂) and cannot be solved analytically. The solution can only be obtained by using suitable approximations and/or iterative numerical calculations. In the past, several approximations have been developed to treat this problem.

- **The Valence Bond Theory (VB)** was developed by the two physicists Walter Heitler and Fritz London. It was the first approximation to describe the bonding in multi-electron systems and was designed to describe the H₂ molecule. According to this model, a covalent bond between two atoms is formed by the overlap of valence atomic orbitals each filled with a single electron. The atomic orbitals are combined to a molecular orbital and the energy of the bond is defined by the location of the electrons and thus the wave function of the orbital. This

approach gives good results of the binding energy of the orbitals but lacks in the description of the location of the electrons [33].

- **The Molecular Orbital Theory (MO)** was developed by Friedrich Hund, Robert Mulliken, John C. Slater, and John Lennard-Jones. In this approach, the electrons are not treated simultaneously but rather one by one. The multi-electron wave function is then described as the product of the two single-electron wave functions and the spin function. This method is also known as the *linear combination of atomic orbitals* (LCAO) and is the basis for the *Hartree-Fock* method and the *density functional theory* [33].
- **The Hartree-Fock Method** was developed by Douglas Rayner Hartree and Wladimir Alexandrowitsch Fock. This method uses the LCAO product of single-electron wave functions (described by the *slater determinant*) to solve the time-independent Schrödinger equation for multi-electron systems. The quantum mechanical variation principle states that by using the wrong molecular wave function, the energy of the ground state is always higher than the real ground state energy (exact wave function). This opens the possibilities for an iterative approach. The so called *self consistent field* method [33].
- **Density Functional Theory (DFT)** is a theory independent of the Hartree-Fock approach and based on the *Hohenberg-Kohn* theorem [34] which means that for a hamiltonian with a certain potential $V(\vec{r})$ only one electron density $n(\vec{r})$ exists. With this formulation a N-electron problem with $3N$ variables can be reduced to 3 variables, allowing a much faster numerical calculation [35].

The development of the individual theories and the used approximations can be found in quantum chemical textbooks (like [36] or [37]) and thus will not be discussed here in detail. However, DFT became a very common tool for the description of the electronic structure of atoms, molecules, clusters, and solids and is extensively used for the interpretation of spectroscopic measurements. With keeping this in mind, the next part will give a short introduction to DFT and the StoBe-deMon package, a computational program for the simulation of X-ray absorption and emission spectra.

2.2.1 Density Functional Theory (DFT)

The StoBe-deMon code used for the simulation of XE and XA spectra is based on the solution of the Kohn-Sham DFT equations with a linear combination of Gaussian type orbitals. Thus a short introduction to density functional theory will be given on the next pages. For a more detailed description of DFT and as starting point for a

literature review, the publication of Tom Ziegler [38], the Nobel lecture of Walter Kohn [35], and other review articles can be recommended [39].

Density functional theory is a theoretical description which has the goal to solve the non-relativistic many-body Schrödinger equation. In contrast to the Hartree-Fock method, which is based on the many-body wave functions, DFT translates the Schrödinger equation in a density form. In this formulation, the ground state of the system can be expressed by an electron density $n(r)$. The transformation from a wave function based description to a density based description results in a dramatically reduced dimensionality of the problem. The density $n(r)$ describes the probability to find an electron with arbitrary spin at the position of r , while $N-1$ electrons have the same spin as the electron at position r but are located at arbitrary positions.

The development of DFT can be divided into three steps. The basis of this theory was built by Llewellyn Thomas and Enrico Fermi [40]. The Thomas-Fermi method represented a fundamentally different approach compared to Hartree-Fock in which the system is described by means of the electron density $n(r)$ and in which the system of electrons is seen as a classical liquid.

The second stage of the DFT theory was reached by the work of Hohenberg and Kohn. In their work from 1964 [34] they showed that there exists a universal functional $F[n(r)]$ for the ground-state density $n(r)$ of an interacting electron gas in an external potential $v(r)$. Furthermore, they showed that this functional $F[n(r)]$ fulfills the expression $E = \int v(r)n(r)dr + F[n(r)]$ in a way that it reproduces—when minimized—the correct ground-state energy associated with the external potential $v(r)$. The Rayleigh-Ritz principle allows to calculate the ground-state energy by means of minimizing the energy

$$(2.5) \quad E = \min_{\tilde{\Psi}} (\tilde{\Psi}, H\tilde{\Psi})$$

where $\tilde{\Psi}$ is a normalized trial wave function for a given number of electrons and corresponds to a trial density $\tilde{n}(r)$. Translated into the density formalism, equation 2.5 becomes the fundamental Hohenberg-Kohn (HK) minimal principle.

$$(2.6) \quad E = \min_{\tilde{n}(r)} \left[\int v(r)\tilde{n}(r)dr + F[\tilde{n}(r)] \right] = \min_{\tilde{n}(r)} E_v[\tilde{n}(r)]$$

This formula ensures that the minimum is only attained when $\tilde{n}(r)$ is the ground-state density or if $\tilde{n}(r)$ is any of the degenerated ground-state densities.

With this method “finding the minimum of $(\tilde{\Psi}, H\tilde{\Psi})$ with respect to the $3N$ -dimensional trial functions $\tilde{\Psi}$ is transformed into a trivial problem of finding the minimum of $[E_v[\tilde{n}(r)]]$ with respect to the 3-dimensional trial function $\tilde{n}(r)$ ” [35].

The third milestone in the development of modern DFT was the realization of the Kohn-Sham equations. The Kohn-Sham equations are based on the self-consistent single-particle equations of Hartree proposed in 1929. Kohn and Sham translated the description of Hartree, who modeled a non-interacting many-particle problem, in which a single particle (electrons) moves in an effective single-particle potential, into a model in which interacting particles move in an effective external potential $v_{eff}(r)$ instead of $v(r)$. By solving the single-particle Schrödinger equation

$$(2.7) \quad \left(-\frac{1}{2}\nabla^2 + v_{eff}(r) - \epsilon_f \right) \phi_f(r) = 0$$

with the effective external potential,

$$(2.8) \quad v_{eff}(r) = v(r) + \int \frac{n(r')}{|r-r'|} dr' + v_{xc}(r),$$

in which $v_{xc}(r)$ is defined as the *local* exchange-correlation potential and depends on the entire density distribution $\tilde{n}(r)$,

$$(2.9) \quad v_{xc}(r) = \frac{\delta}{\delta \tilde{n}(r)} E_{xc}[\tilde{n}(r)]|_{\tilde{n}(r)=n(r)}$$

the minimizing density

$$(2.10) \quad n(r) = \sum_{f=1}^N |\phi_f(r)|^2,$$

$n(r)$ is obtained.

The ground-state energy is given by

$$(2.11) \quad E = \sum_j \epsilon_f + E_{xc}[n(r)] - \int v_{xc}(r)n(r)dv - \frac{1}{2} \int \frac{n(r)n(r')}{|r-r'|}$$

If E_{xc} and v_{xc} are neglected, the Kohn-Sham equations 2.7-2.11 transform back into the self-consistent Hartree equations.

Some remarks to the Kohn-Sham Theory:

- “With the *exact* E_{xc} and v_{xc} all many-body effects are in principle included” [35]. However, “the practical usefulness of ground-state DFT depends entirely on whether approximations of the functional $E_{xc}[\tilde{n}(r)]$ could be found which are at the same time sufficiently simple and sufficiently accurate” [35].

- If the physical density $n(r)$ is known, either for small systems from wave function based calculations, or from experiment, $v_{eff}(r)$ and $v_{xc}(r)$ can be directly calculated from the density $n(r)$. This is possible since the effective single-particle potential $v_{eff}(r)$ of KS theory (see eq. 2.8) which describes a fictitious external potential leads for non-interacting particles to the same physical density $n(r)$ as the physical external potential $v(r)$ for interacting electrons [41].
- The KS single particle wave functions $\phi_f(r)$ and the Hartree-Fock HF wave functions $\phi_f^{HF}(r)$ can be seen as two different classes in which the first is the optimal fit with regard to the density $n(r)$ while the second is the optimal fit regarding the total-energy of the system.
- Despite two exceptions, the exact KS wave functions ϕ_f , as well as the energies ϵ_f , have no directly observable (physical) meaning. The first exception says that, if $n(r)$ represents the true, physical density, then also the KS orbitals ϕ_f have a physical meaning linked with $n(r)$ via equation 2.10. Secondly, the highest occupied ϵ_f DFT eigenvalue is free from relaxation correlation and thus the energy difference to the vacuum corresponds to the ionization energy [42].

Approximations for $E_{xc}[n(r)]$

Although the mathematical theory described above has been motivated by physical considerations, effective approximations for $E_{xc}[n(r)]$ have to be formulated to make a practical use of it. “*These approximations reflect the physics of electronic structure and come from outside of DFT*” [35].

The most common and most important approximations for $E_{xc}[n(r)]$, which will also be used in this work, have a quasi-local form. In this approach $E_{xc}[n(r)]$ can be expressed as

$$(2.12) \quad E_{xc}[n(r)] = \int e_{xc}(r;[n(\tilde{r})])n(r)dr.$$

In this equation $e_{xc}(r;[n(\tilde{r})])$ represents an exchange-correlation energy/particle at point r , which is a functional of the density distribution $n(\tilde{r})$. The exchange-correlation energy/particle mainly depends on the density $n(\tilde{r})$ at points \tilde{r} near the point of interest r . This concept of “nearest-sightedness” was mentioned by Kohn in 1996 [43]. This concept also results in equation 2.12, where $e_{xc}(r;[n(\tilde{r})])$ is a nearsighted function of $n(\tilde{r})$.

The “mother” of all approximations for $E_{xc}[n(r)]$ is the so-called *local density approximation* (LDA)

$$(2.13) \quad E_{xc}^{LDA} = \int e_{xc}(n(r))n(r)dr$$

where $e_{xc}(n)$ is the exchange-correlation energy per particle of a uniform electron gas of density n [44]. While the exchange part is fix, the correlation part was first estimated by E.P. Wigner (1938) [45] and later by D.M. Ceperley (1978) [46].

Remarks:

- LDA was expected to be useful for slowly varying densities only. In atomic systems, however, these conditions are rarely satisfied. Nevertheless, LDA had proven to give quite useful results.
- Physical properties such as ionization energies of atoms and dissociation energies of molecules are typical in reasonable agreement with experiments, while bond length and thus the geometries of molecules and solid are typically very well described.
- The analogy to a non-interacting electron gas is simultaneously the reason why LDA fails for systems dominated by strong electron-electron interaction effects.

Common LDA functionals are the Perdew-Zunger (PZ) [47], Perdew-Wang (PW) [48], and Vosko-Wilk-Nusair (VWN) [49].

A more sophisticated approximation uses the concept of an average exchange-correlation hole distribution instead of a uniform electron gas and is called the *generalized gradient approximation* (GGA). The physical exchange-correlation hole density is given by $n_{xc}(r, r') = g(r, r') - n(r')$, where $g(r, r')$ is the density at r' caused by an electron located at r . “It describes the ‘hole’ dug into the average density $n(r')$ by the electron at r ”[35]. The exchange-correlation functional E_{xc} obtained from this Ansatz can be expanded around the point r leading to the following equations:

$$(2.14) \quad E_{xc}^0 = \int \epsilon(n(r))n(r)dr \quad (LDA)$$

$$(2.15) \quad E_{xc}^{(1)} = \int f^1(n(r), |\nabla n(r)|)n(r)dr \quad (GGA)$$

$$(2.16) \quad E_{xc}^{(2)} = \int f^2(n(r), |\nabla n(r)|)\nabla^2 n(r)dr$$

While the LDA approximation in equation 2.14 only requires the calculation of a function of only one variable $n(r)$ (density), the GGA approximation 2.15 requires the calculation of a function of two variables, $n(r)$ (density), and $|\nabla n(r)|$ (gradient of the density).

Popular representatives of GGA exchange functionals are Perdew-Burke-Enzerhof (PBE [50]) and Becke88 (B88 [51]). The parameters used in PBE are obtained from physical constraints, while the B88 parameters are obtained empirically. The most popular GGA correlation functionals are PBE [50], PW91 (Perdew in [52] pp. 11-20), Lee-Yang-Parr (LYP [53]), and Perdew86 (P86 [54]).

The widely used B3LYP exchange-correlation functional [55] is a member of the third class of functions, also called hybrid functionals. These functionals have the form:

$$(2.17) \quad E_{xc}^{hyb} = \alpha E_x^{KS} + (1 - \alpha) E_{xc}^{GGA}$$

E_x^{KS} is the exchange energy calculated with the exact Kohn-Sham orbitals (see 2.10). E_{xc}^{GGA} is an appropriate GGA functional, and α is a fitting parameter [56, 57].

2.2.2 Spectra Calculation

As described above, the intensity of an X-ray absorption and an X-ray emission is described by Fermi's "Golden Rule". To compute a theoretical XA or XE spectrum, a set of energy levels with their corresponding wave function and oscillator strength has to be calculated and the cross section between the wave functions has to be evaluated. Up to this point all these steps were in the ground state configuration and no final state effects (core hole, or valence hole) are considered. Since the final state effects affect the two processes independently, these effects have to be implemented differently.

All theoretical spectra created in this thesis are generated with the StoBe-deMon DFT program [58]. The StoBe-deMon program solves the Kohn-Sham DFT equations 2.7-2.11 with a linear combination of Gaussian type orbitals. Details of the computational realization can be found in Refs. [59, 60].

XAS Spectra

Historically, theoretical XA spectra were generated by using the Z+1 or, in other words, the full core-hole (FCH) approximation. The implementation into the calculation can be done either by replacing the excited atom by an atom of the element following in the periodic table, or by removing a core electron [61, 62]. This approach consequently neglects all initial state effects.

The half core hole (HCH) approximation is a description that at least partially includes both, the initial and final state effects. Within this method "half" an electron is removed from the excited core state [62, 63]. This approximation is easily implemented in the Kohn-Sham theory. It turns out that this approximation describes the relaxation

effects correctly up to the second order. This results in a good description of the relative energies and a very good description of the transition probabilities.

XES Spectra

For calculated XE spectra, the use of HCH and FCH does not significantly improve the quality of the spectrum. The best description can be achieved by using the so called “frozen orbital” approach, in which the transition matrix elements are calculated with the ground state Kohn-Sham orbitals. With this approach, both core and valence relaxation effects are not considered. Luckily, the errors partially cancel out [64].

However, the negligence of vibrational information and nuclear dynamics can result in a severe disagreement between theory and experiment [65]. Nuclear dynamics can be included by *ab initio* molecular dynamics.

Theoretical Framework Used in this Thesis

In this thesis the exchange functional of Becke (B88) [51] and the GGA correlation functional of Perdew and Wang (PW91) were used [54]. It was shown that these exchange and correlation functions result in a good agreement to experiments of free and chemisorbed molecules [62, 64, 66–68].

The XAS oscillator strengths were calculated within the HCH approximation for which half an electron is removed from the core level of the excited atom. Good transition energies can be obtained by using different approaches. In this thesis the transition energy was calculated using the HCH approximation, subsequently the core level binding energy and therefore also the transition energy was corrected, by the Δ KS method plus a correction term accounting for relativistic effects [62].

The Δ KS core level binding energies (ionization potential) are achieved by calculating the energy difference between the ground state total energy and the core excited state total energy.

The XES oscillator strength was calculated using the ground state “frozen orbital” approach [64]. The transition energies on the other hand were then calculated separately using the HCH method for each of the valence orbitals. Subsequently, the core level binding energy was extracted from the Δ KS calculation.

As molecular basis set a triple-zeta valence plus polarization basis [69] was used. In order to obtain a better description of relaxation effects, the ionized atom was described by the IGLO-III basis of Kutzelnigg *et al.* [70]. To define the excitation center and prevent intermixing of electronic levels, atoms equivalent to the excitation center were described by effective core potentials (ECP) [71].

This combination of theoretical level and basis sets is well tested for x-ray spectroscopy calculations and gives reliable results for many systems [72].

2.3 Experimental Setup

The availability of bright X-ray light sources was a milestone for the usability of soft X-ray experiments and particularly for soft x-ray emission spectroscopy experiments. Due to the low cross section of the process, bright 3rd generation synchrotron light sources are required to achieve appropriate measurement times. Furthermore, tunable X-ray light sources allow resonant excitation and absorption measurements. The experiments presented in this thesis were recorded at beamline 8.0 of the Advanced Light Source (ALS), Lawrence Berkeley National Laboratory in Berkeley, California. Beamline 8.0 is a specially designed beamline to gain the maximum of photon flux out of an 1.9 GeV electron beam (storage ring). To do so, the insertion device, a 5-cm-periodic undulator, and a minimal number of optical elements were used (four in total). The beamline consists of a first condensing mirror, a monochromator equipped with three interchangeable spherical gratings, and two refocusing mirrors (one horizontally directly after the exit slit of the monochromator and one vertically directly in front of the experimental chamber). The beamline can operate at photon energies between 80 and 1400 eV, covered by the three gratings, and reaches a photon flux of $\approx 10^{11} - 6 \times 10^{15}$ photons/s and a resolution of $E/\Delta E > 8000$. With the two refocusing mirrors, a spotsize of $30 \mu\text{m} \times 100 \mu\text{m}$ is achieved. The SALSA (Solid And Liquid Spectroscopic Analysis) endstation is equipped with a custom-built soft X-ray spectrometer and a spherical electron analyzer (SPECS Phoibos 150 MCD) [73]. A DN 150CF flange allows the optional use of a liquid flow through cell, a gas cell, an electrochemistry cell, as well as a motorized solid state manipulator. For further details, please refer to the doctoral theses of Monika Blum [73] and Oliver Fuchs [74] and corresponding publications [10, 11, 75].

Within the liquid flow through cell, the sample liquid is passing a thin window membrane which separates the liquid and the ultra-high vacuum. Fig. 2.3 schematically shows the arrangement of the liquid cell.

In this setup the sample liquid is separated from the vacuum by a 100–200 nm thin membrane. Several materials can be used for the membrane but certain requirements have to be fulfilled. The membrane has to withstand the pressure difference, the material should not degrade in an intense X-ray beam, and the elements in the membrane should have absorption edges far away from the excitation edge of interest (should be transparent or semi-transparent in the region of interest). The membrane materials used in this thesis were Si_3N_4 for measuring the OK-edge and SiC for measuring the NK-edge. Simulated transmissions for different membrane materials were illustrated by Monika Blum [73].

The sample liquid is pumped through the measuring region behind the membrane. The channel cross-section is 0.13 mm^2 and typical pump rates of about 6 ml/min were

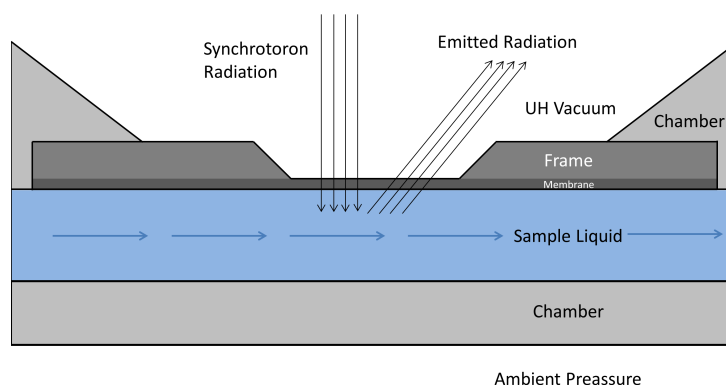


FIGURE 2.3. Schematic illustration of the membrane and the liquid behind.

used. Together with a beam size of $30 \times 150 \mu\text{m}$, the probing volume is replenished about $5000\times$ per second. The actual replenishing rate might be a bit lower due to the bulging of the membrane which increases of the pumping cross section. This bulging can be kept to a minimum by decreasing the “window” size. Best results were achieved by using membranes with a height of 0.1 mm and a width of 1 mm .

Details about the liquid flow through cell, including technical sketches, can be found in the article of Blum *et al.* [10].

Using a membrane instead of a liquid “Jet”, as it is used in some other experimental setups [5] has many advantages. The main advantage of the liquid flow through cell is that the sample is during the measurement in thermodynamic equilibrium, while in the jet setup the liquid evaporates as soon as it enters the vacuum chamber. A downside of this cell approach is that only photon-in-photon-out techniques can be used as a probe. This disadvantage is simultaneously the advantage of this method since it provides pure bulk information and is not limited to the surface like photoelectron spectroscopy (PES). Especially because the properties of the water molecules at the surface of the liquid are expected to be different from its bulk [4].

However, the membrane involves some potential problems which have to be carefully taken into account. Firstly, The degradation of the membrane material. The used materials (Si_3N_4 and SiC) are under a high level of thermal stress caused by the intense X-ray beam. The cooling is usually done by the sample liquid. With a large reservoir (50 ml) and a measurement time of about one hour, a small increase in the reservoir temperature of about 4 to 5°C can be detected. For sensitive experiments the entire DN 150CF flange is connected to a temperature controller regulating the temperature of the liquid cell between 4°C and 70°C . The intense X-ray radiation can lead to the oxidization of the membrane resulting in a characteristic spectrum. Careful measurements and a regular replacement of the membrane prevent these artifacts

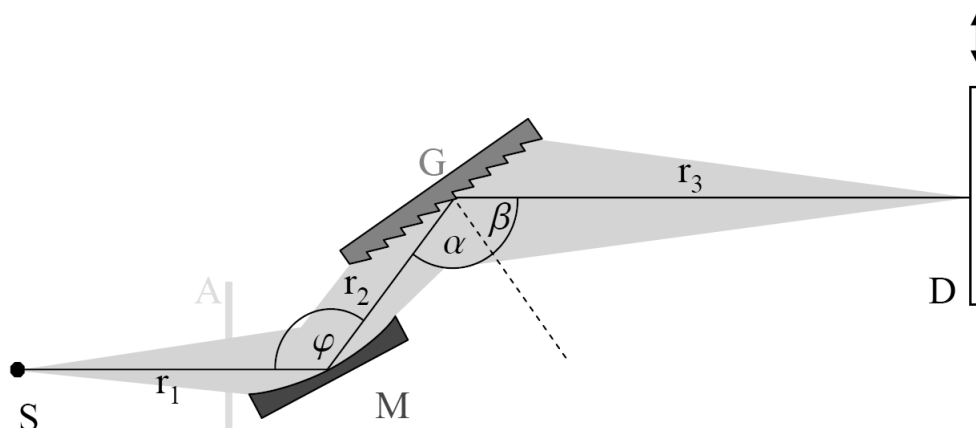


FIGURE 2.4. Schematic illustration of the spectrometer with X-ray spot **S**, aperture **A** to block visible light, spherical mirror **M**, variable line space grating **G**, and CCD detector **D** [74].

[11, 76]. Secondly, the agglomeration of solute or fractions of solute on the membrane. The intense X-ray beam damages the molecules either during the emission process [65, 77], or afterwards via auto ionization [78]. These molecules or the fractions of these molecules can be “baked” to the membrane as well. This effect is discussed in more detail in chapter 3.2.3.

The soft X-ray spectrometer is a custom designed variable line space spectrometer (VLS) designed by Oliver Fuchs. Details about the construction can be found in his doctoral thesis [74] and in literature [75]. The spectrometer is designed to achieve a maximum transmission in an energy range of 130 to 650 eV with an energy resolution of $E/\Delta E > 1200$. The low energy limit is set by to the geometry of the optical elements and the detector. Recent modifications lowered this limit to 85 eV. The upper limit is defined by the reflectivity of the nickel coated optical elements. The spectrometer consists of three optical elements and has no entrance slit, thus the X-ray spot defines the source and has to be smaller than $30 \mu\text{m}$ in dispersive direction. The first optical element is a spherical mirror which focuses the source spot onto the second optical element, a blazed plane variable line space grating. Finally the X-rays are detected with an uncoated back-illuminated CCD-camera with 2048×2048 pixels. The non-dispersive direction of this two-dimensional picture is then integrated, generating a one-dimensional spectrum.

The high transmission of the spectrometer reduces the exposure time dramatically and allows to record spectra with a good signal to noise ratio in times as short as ten seconds. The high efficiency gives the possibility to record hundreds of emission spectra at different excitation energies in an acceptable time. With this spectrometer, an emission spectrum can be recorded at each excitation step in a regular X-ray

absorption experiment. The data is then presented best in a so called RIXS-map [73, 74, 79].

Since the spectrometer has no entrance slit which defines the source, the focus position of the spectrometer and the focus position of the beamline have to be aligned. For the liquid cell this can be achieved using a standardized calibration procedure (see [74]). For solid state experiments, the sample surface is carefully placed in the focus position defined by the beamline and the spectrometer by aligning the elastic lines at an incoming photon energy of 400.88 eV to their original pixel positions.

To calibrate the energy axis of the spectra, two methods are used depending on the type of data (1d-spectrum, 2d-RIXS-map). Two dimensional RIXS maps are calibrated using the elastically scattered X-rays causing a sharp intensity feature at equal emission and excitation energy (Rayleigh line). If the exact energy of the beamline is known, the map can be calibrated by fitting the position of the elastic line with the VLS spectrometer function [74]. With this procedure the error of the absolute energy can be estimated to be of about 0.1 eV and uncertainties in the relative energy scale are about 0.05 eV.

For calibrating beamline 8.0, reference measurements of TiO_2 for the oxygen K-edge, N_2 for the nitrogen K-edge, and HOPG for the carbon K-edge were performed and compared to literature [80–82]. For calibrating single spectra, the beamline is tuned to the first absorption resonance of gaseous N_2 which has a defined absorption energy of 400.88 eV. The detector of the VLS is then aligned in a way that the elastic line appears at specific pixels on the CCD (detailed information can be found in [74]). The elastic line of 400.88 eV appears on the CCD twice. This allows to correct small errors in the hardware calibration by fitting the two positions with the VLS spectrometer equation.

Since the liquid flow-through cell is directly connected to the SALSA chamber, the position of the membrane is well defined and the focus of the beamline and the spectrometer onto the same spot of the membrane can be achieved with a standardized calibration procedure (see [74]). For solid state experiments, the sample manipulator is carefully moved to place the sample surface in the focus position by aligning the elastic lines at an incoming energy of 400.88 eV to their original pixel positions.

2.3.1 Sample preparations

The different organic and inorganic molecules, which are addressed in this thesis, were measured in different environmental conditions depending on the physical condition of the molecule. All chemicals were used without further purification.

Methylamine is a gas and was also measured in gas phase. The chemical was provided from the Advanced Light Source and had a purity of $\geq 98\%$. The molecule

was measured as reference to the amino acid lysine (see Fig. 3.15).

At atmospheric pressure pyrrolidine is a liquid and was purchased from sigma aldrich with a purity of $\geq 99\%$. Typical impurities within the sample are traces of water. Pyrrolidine was measured as reference molecule to the amino acid proline. To study the different chemical configurations of the molecule, an aqueous solution of 2 M pyrrolidine was made. To achieve the desired pH-values of 1.4 and 13.6, hydrochloric acid (HCl) and sodium hydroxide (NaOH) were added to the solution.

Acetic acid was measured as reference molecule for the OK emission of the different amino acids. The acetic acid was purchased from sigma aldrich as aqueous solution (50 wt%). For the measurements the solution was diluted to a 25 wt% solution. At this concentration a pH-value of 0.2 was observed. To create a solution with pH 12.8, NaOH (50 %) was added to the base solution.

Pure imidazole comes as a crystalline powder and was purchased from alfa aesar (purity $\geq 98\%$) and is only contaminated by traces of water. The low vapor pressure prevents the measurement of pressed powder samples in ultra-high vacuum. Nevertheless, due to the very good solubility of imidazole in water the molecule could be investigated in an aqueous solution. Again a base solution of was created (5 M, pH 10.3). To lower the pH-value, 20 ml of HCl was added to the solution. This reduced the concentration to 2.78 M and the pH-value to 1.8.

All investigated amino acids were purchased from sigma aldrich. The amino acids come as white, mostly odorless powder crystals. The purity varies, but was always chosen to be greater than $\geq 98\%$. Typical impurities are water ($\leq 2\%$), ammonia ($\leq 0.1\%$), chloride ($\leq 0.1\%$), sulfate ($\leq 0.1\%$) other amino acids ($\leq 0.1\%$) and metals (1 – 100 ppm).

The library of XE spectra presented in chapter 3.1 as well as the resulting spectral fingerprints (3.1.1) were measured on pressed powder samples. To form the pallets, a small amount of the amino acid was evenly distributed between two Teflon sheets and pressed with a hydraulic press (5 tons/cm²) into smooth chips. The chips were about 0.5-1 mm thick, 1 cm² large, and were glued with carbon tape on the SALSA sample holder. The entire procedure was done under ambient conditions. Some amino acids are hydrophilic, which was the reason why the exposure of the samples to air was kept to a minimum. Furthermore, for degassing purposes, before the measurement the samples were stored in the loadlock at high vacuum conditions ($\approx 10^{-6}$ mbar) for at least 30 minutes.

To keep the heat and the radiation induced damages of the organic molecules to a minimum all solid state samples were moved in the X-ray beam. By scanning the samples, the exposure time per sample spot was reduced to 0.15 s. Details on the scanning parameters can be found in [83]. However this requires a homogeneous and smooth sample surface. The pressed powder pallets were still showing slight

variations within the sample. Due to these variations the pressed powder samples were only used for non-resonant exited XES measurements.

The RIXS investigations of solid proline (see section 3.2.1) were performed on ultra-high vacuum (UHV) evaporated thin films, which show a much higher purity and better homogeneity than the pressed powder samples. However, the preparation of UHV evaporated samples is much more time consuming. A detailed description is given in section 3.2.1.

The amino acids proline and histidine are also investigated in their natural, aqueous environment. For studying the pH dependent changes in the electronic structure of these amino acids, solutions of different pH-values were created.

In section 3.2.3 proline is investigated at pH 1, 6.8, and 13. The desired pH-values were achieved by firstly solving 6.9 g of proline in 20 ml ultra-pure water, which results in a 3 mol/l solution with pH 6.8. To set the pH-value to 13, 3.0 ml of NaOH (50 %) was added to the base solution, resulting in a proline concentration of 2.6 mol/l. For the low pH sample the initial concentration of proline was reduced to about 1 mol/l (2.3 g in 20 ml) before 3.85 ml of HCl (50 %) were added to the solution and a pH-value of 1 was achieved. The final concentration of this solution was about 0.8 mol/l.

For the investigation of histidine four sample solutions with pH-values of 0.1, 2.8, 7.9, and 13.0 were created. As for proline a base solution of histidine was created, in which then NaOH (50 %) and HCl (50 %) was added, respectively. Due to the lower solubility of histidine the concentration of the base solution was set to 0.13 M (1 g in 50 ml). Hence only small amounts of HCl and NaOH were necessary to adjust the pH to the desired values, which had only minor effects on the net concentration of the solutions.

X-RAY SPECTROSCOPY OF PROTEINOGENIC AMINO ACID FILMS AND SOLUTIONS

Amino acids are the most important biomolecules for all living creatures on earth. Firstly discovered in 1806, today over 500 different amino acids are known [84]. 23 of these amino acids are known as proteinogenic amino acids, since these 23 amino acids form all peptides and proteins needed for life on earth. Three out of these 23 proteinogenic amino acids are rather rare whereas the other 20 form the building blocks of all common proteins. Amino acids are named like this, because they all are composed of a carboxylic acid group (COOH), an amine group (NH₂), and a specific side-chain attached to the same carbon atom. This class of amino acids are also known as α -amino acids. Since the amine group is a strong proton acceptor and the carboxylic group is a strong proton donor, the amino acids are in a zwitterionic conformation in a physiological relevant pH region. In this conformation, for most of the amino acids the carboxylic group is deprotonated (COO⁻) and the amine group is protonated (NH₃⁺). This zwitterionic configuration is also the dominating configuration for crystalline amino acids. Furthermore, for 19 of the 20 standard amino acids the α -C atom is

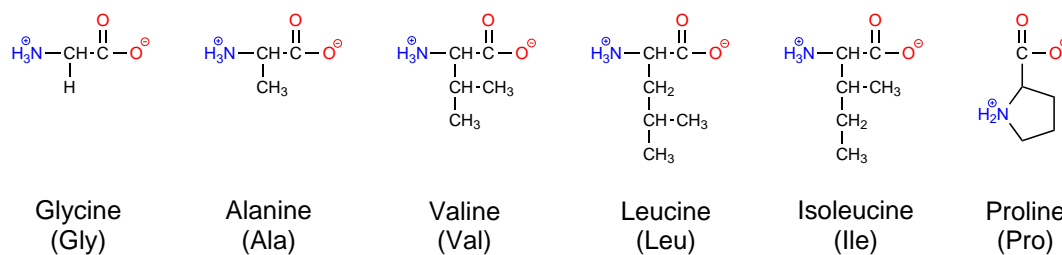


FIGURE 3.1. Amino acids with aliphatic side chain.

an asymmetric carbon atom causing these molecules to be chiral. Since all standard amino acids used for protein formation are in L-configuration, this work focuses on the L-amino acids. The character and properties of the amino acids is closely related to its specific side chain which also allows the classification of the amino acids according to the chemical properties of the side chains. The six groups of side chains are displayed in Fig. 3.1-3.4.

The five amino acids alanine, valine, leucine, isoleucine, and proline have non-aromatic carbon and hydrogen side chains (aliphatic). These side chains are also famous for their hydrophobic character.

Proline, however, is very special among the 20 standard amino acids. Its aliphatic side chain is back connected to the α -amine group. Due to this back connection of the side chain, the amine group is in a secondary configuration instead of a primary, as it is the case for all the other 19 amino acids. Furthermore, the flexibility of proline is strongly limited by this back connection and thus is often the cause of kinks in the shape of proteins and peptides. Due to these unique characteristics of proline, this amino acid will be discussed in more detail in chapter 3.2.

Amino acids with an aromatic side chain form the second group (see Fig. 3.2a). Representatives of this group are phenylalanine, tyrosine, and tryptophan. The delocalized π -orbital system of the side chain allows all three amino acids to absorb UV light.

Methionine and cysteine are the only two standard amino acids hosting a sulfur atom (Fig. 3.2b). The sulfur atoms provide the two amino acids with special abilities. Methionine is very proteinogenic and is often the starting point of the protein formation. Cysteine on the other hand is able to form disulfide bonds between two cysteine molecules. The di-cysteine molecule with a disulfide bond is called cystine. The disulfide bonds also occur within proteins ensuring and enhancing the stability of the geometric shape (tertiary structure). The most famous protein with disulfide bonds is the peptide hormone insulin regulating the human blood sugar concentration.

The amino acids with an alkaline side chain are shown in Fig. 3.3a. Histidine,

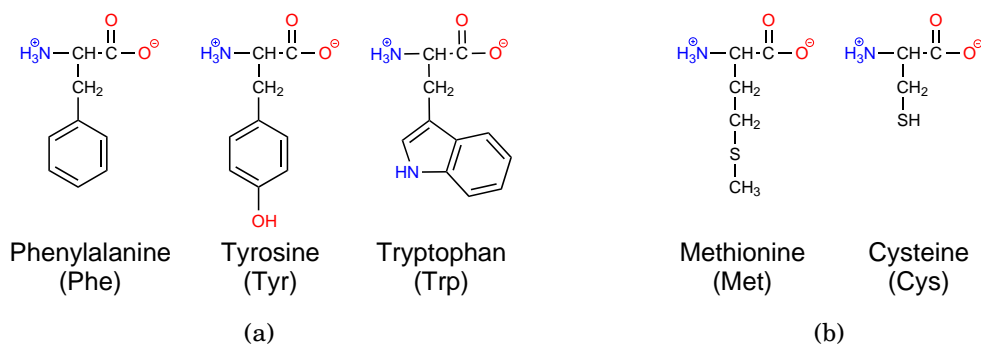


FIGURE 3.2. (a) Aromatic amino acids. (b) Amino acids hosting a sulfur atom.

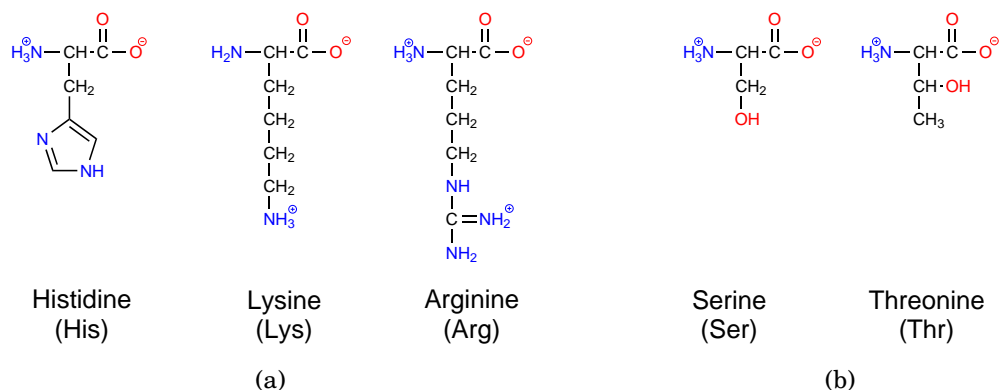


FIGURE 3.3. (a) Amino acids with an alkaline side chain. (b) Alcoholic amino acids.

lysine, and arginine have hydrophilic nitrogen groups embedded in their side chains. For lysine the zwitterionic configuration is different. The side chain is protonated instead of the α -amine group. At neutral pH (pH 7) both amino groups are positively charged which gives the molecule a net charge of +1. The side chain of histidine comprises of an imidazole ring. The properties of imidazole and its ion imidazolium will be examined in more detail in chapter 3.3.2. Serine and threonine are amino acids with an alcoholic functional group within the side chain. Unlike the carboxylic group, the alcohol group is harder to ionize and hence neutral at neutral pH.

The last four amino acids are: aspartic acid, glutamic acid, and their amid derivatives asparagine and glutamine (Fig. 3.4). The additional carboxylic groups of aspartic acid and glutamic acid are deprotonated at pH 7, which means aspartic acid and glutamic acid participate in the net-charge of proteins and peptides. The most famous representative of this group is the monosodium salt of glutamic acid, well known as glutamate and often used as flavor enhancer. The amide group of asparagine and glutamine is highly polar and often the source of hydrogen bonds within a protein as well as between a protein and the surrounding water. The above given introduction about the 20 proteinogenic amino acids is based on the biochemistry textbook of Robert H. Horton *et al.* [85, pp. 75-114].

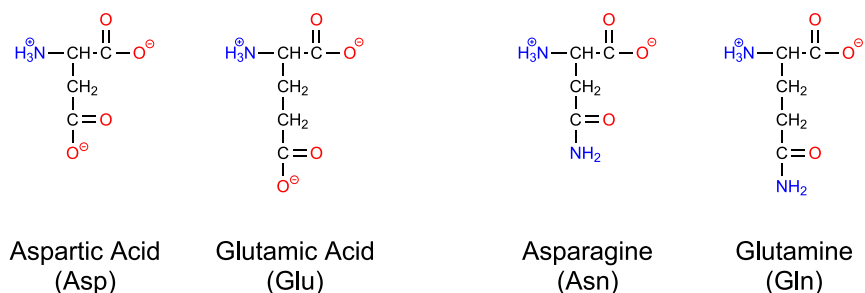


FIGURE 3.4. Amino acids with acid side chain and its amid derivatives.

3.1 Spectral Signature of the Local Electronic Structure of Proteinoigenic Amino Acids

On the following pages a library of the X-ray emission spectra of the 20 proteino-genic amino acids in solid phase at all relevant emission edges (OK, NK, CK) will be shown and discussed. It can be easily seen that the oxygen emission spectra and the nitrogen emission spectra can be grouped by their overall shape. The grouping underlines the local probing character of XES and implies that a description of the spectra using a qualitative spectral fingerprint analysis is possible. By exciting the molecules with different photon energies, the location of the excitation can be pinned to either an oxygen, nitrogen, or and carbon atom. The resulting emission spectra are then strongly weighted by the shape of the orbitals surrounding the excitation site. Hence, an oxygen emission spectrum directly probes the orbital structure surrounding the carboxylic group, while the nitrogen emission spectrum determines the electronic structure surrounding the amino group. The carbon atoms form the backbone of the molecules and thus a carbon emission spectrum contains information about the entire electronic structure of the molecule. The selection can be further specified by using resonant excitation. With resonant excitation (RIXS), it is experimentally possible to distinguish between atoms of the same element in different chemical environments. As described in the theoretical part above (see chapter 2.1.3), the RIXS process is more complicated than a regular emission process and the spectra can be highly influenced by resonant effects resulting in more complicated spectrum. On this basis, the library will be limited to regular non-resonantly excited emission spectra (XE spectra).

Fig. 3.5 shows the NK edge emission spectra of the 20 amino acids which are already grouped with respect to their spectral shape. All spectra displayed in Fig. 3.5a. are very similar and show a distinct peak at around 394.8 eV. The exact position of this feature varies from molecule to molecule but lies within a 0.2 eV window. The second characteristic peak of the spectra is a small feature located around 393.1 eV. The low-energy part of all spectra is dominated by a broad feature at around 390 eV and extends in a tail down to 380 eV. In case of alanine, glycine, and serine very weak, an additional weak feature at 386.5 eV and 384 eV can be observed, respectively. All amino acids displayed in Fig. 3.5a have one common ground. All host only one nitrogen atom which forms the α -amino group (see Fig. 3.1 - 3.4). The large similarities imply that the electronic structure surrounding the nitrogen atom of the α -amino groups are only little influenced by the molecular configuration of the side chain. In other words, this nicely demonstrates the local probing character of X-ray emission spectroscopy.

The spectral shape of the second group of spectra (depicted in figure 3.5b) differs

3.1. SPECTRAL SIGNATURE OF THE LOCAL ELECTRONIC STRUCTURE OF PROTEINOGENIC AMINO ACIDS

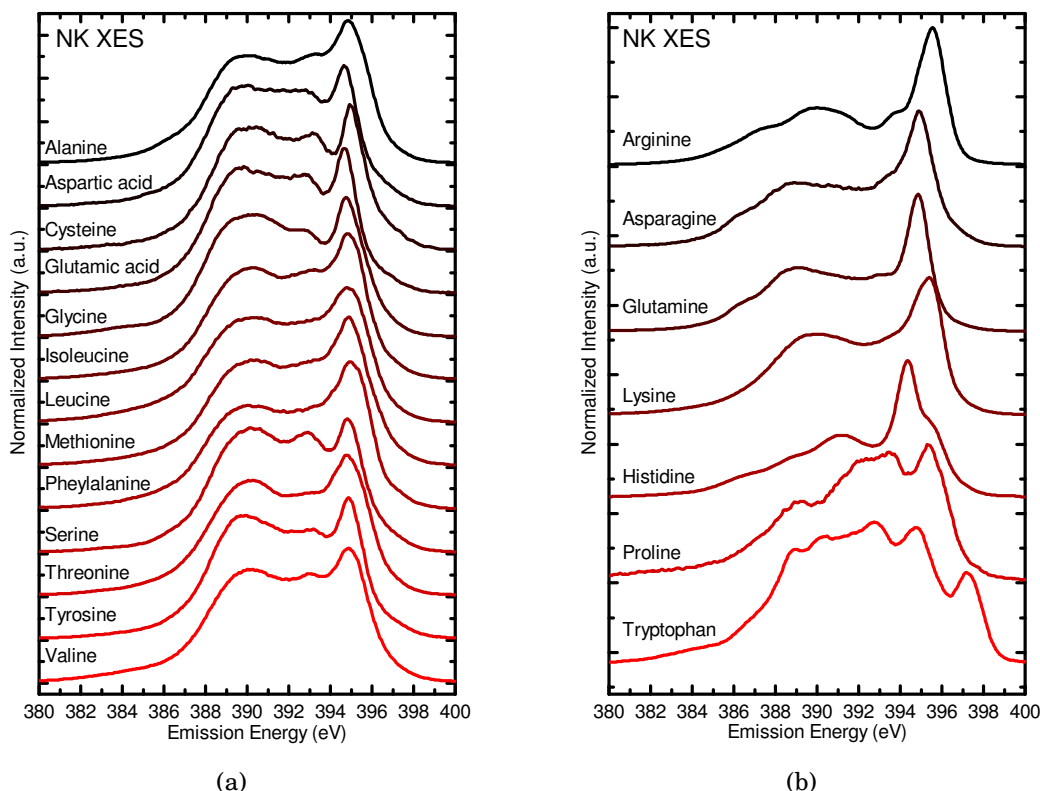


FIGURE 3.5. (a) NK XE spectra ($E_{\text{Exc}} = 424 \text{ eV}$) of amino acids with only one nitrogen atom except proline. (b) NK XE spectra ($E_{\text{Exc}} = 424 \text{ eV}$) of amino acids with more than one nitrogen atom and proline.

significantly from the first group. Furthermore, the spectral shapes are not just different from the spectra shown in 3.5a, but also differ largely among themselves. These differences become plausible since all amino acids displayed in this graph (except proline) have more than one chemically inequivalent nitrogen atom (see Fig. 3.1 - 3.4). Nevertheless, these spectra can also be divided into a high-energy, and a low-energy region.

The top four spectra illustrated in Fig. 3.5b all show an high energy peak which is much more intense compared to 3.5a. The molecular structure of asparagine, glutamine (Fig. 3.4), arginine, and lysine (Fig. 3.3) reveals that these amino acids have at least two chemically inequivalent nitrogen atoms, while one is present in a neutral amino configuration (NH_2). Hence the high intensity feature located between 394 eV and 396 eV can be attributed to this nitrogen configuration. Besides the high intensity feature in the high energy part of the spectrum, also the low energy part of the NK spectrum of arginine, asparagine, and glutamine is different compared to the spectra shown in Fig. 3.5a. In case of lysine, this energy region shows rather large similarities with the spectra shown in Fig. 3.5a. A hint, why these similarities are observed, can

be found again in the chemical structure of the molecules. Besides the neutral amino group (NH_2), which is related to the intense feature at the high energy side of the spectrum, lysine hosts only one additional, protonated amino group (NH_3^+) which is identical to the protonated amino groups of the amino acids shown in Fig. 3.5a. In accordance to the interpretation of Monika Blum [73], one can conclude that the high energy part of the lysine NK XE spectrum is dominated by the neutral amino group (NH_2) and the low energy side is dominated by the protonated amino group (NH_3^+).

The molecular structures of glutamine and asparagine show that the neutral amino group is located in the direct vicinity of a double bond oxygen atom. This combination of amino group and carboxylic group is called *amide*. It seems that the oxygen has a significant influence on the electronic structure of the nitrogen and therefore causes the appearance of an additional emission feature in the low energy region of the NK XE spectra of glutamine and asparagine ($E_{\text{em}} = 386.0\text{eV}$). Moreover, the similarities between glutamine and asparagine are quite astonishing which confirms the local probing character of X-ray emission spectroscopy.

With four chemically different nitrogen atoms, the chemical structure of arginine is very complex. Besides the protonated α -amino group, the side chain consists of three nitrogen atoms. A neutral *primary amine* (endgroup), a neutral *secondary amine* (in the chain), and a *protonated imine* (double bond nitrogen). The entire group is called *guanidine*. Due to the large number of chemically different nitrogen atoms, the contributions of each nitrogen atom to the NK XE spectrum can only be speculated.

The second group of spectra in this graph are the NK XE spectra of histidine, proline and tryptophan. All three molecules show a completely different NK emission spectrum. Among these amino acids, proline has the simplest molecular structure. The aliphatic side chain is back connected to the α -amino group. This incorporates the amino group in a heterocyclic ring structure. Hence, it can easily be assumed that the observed spectrum is largely influenced by the ring structure. Histidine and tryptophan have an even more complicated ring structure than proline. Histidine hosts in total three nitrogen atoms. One in the α -amino configuration and two inequivalent nitrogen atoms as a part of the heterocyclic side chain, also known as *imidazole*. The third amino acid tryptophan hosts only two nitrogen atoms. One is again present as the α -amino group, while the second is incorporated in a complex aromatic ring structure consisting of a six atom and a five atom ring. This aromatic side chain is called *indole*. Due to the extended π orbital structure of the aromatic rings, tryptophan shows the emission feature with the highest emission energy which indicates that this feature ($E_{\text{emis}} = 397.2\text{eV}$) represents the weakly-bonded aromatic π orbital. Since the emission patterns of proline and histidine are quite different from the spectra of the other amino acids, these spectra are investigated in detail in chapter 3.2.3 and 3.3, respectively.

3.1. SPECTRAL SIGNATURE OF THE LOCAL ELECTRONIC STRUCTURE OF PROTEINOGENIC AMINO ACIDS

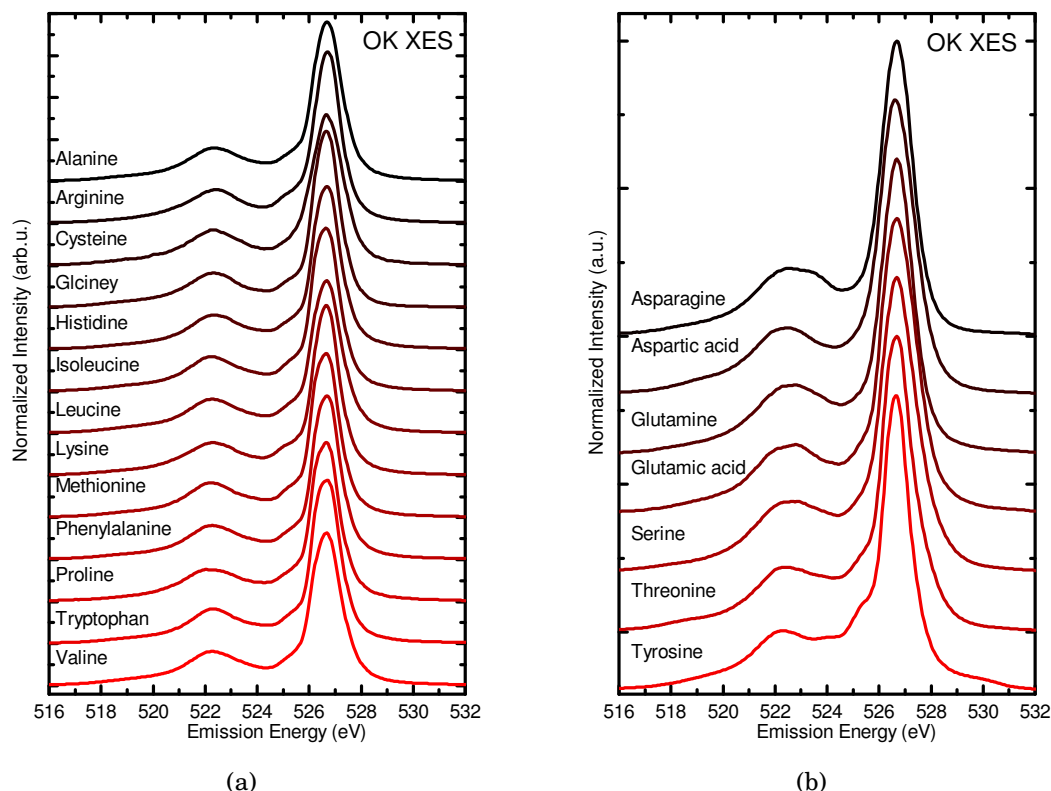


FIGURE 3.6. (a) OK XE spectra ($E_{\text{Exc}} = 557 \text{ eV}$) of amino acids hosting only one carboxylic group with two oxygen atoms. (b) OK XE spectra ($E_{\text{Exc}} = 557 \text{ eV}$) of amino acids with more than two oxygen atoms (one carboxylic group). All spectra were aligned with respect to the energy position of the high intensity features at $E_{\text{em}} = 526.7 \text{ eV}$.

A similar classification of spectra can also be done for the OK XE spectra shown in Fig. 3.6. To achieve a better comparability, the spectra were aligned to the energy position of the dominating feature. Fig. 3.6a shows all amino acids hosting only two oxygen atoms which form the carboxylic group, while Fig. 3.6b illustrates all amino acids with more than two oxygen atoms. The spectra of the carboxylic group displayed in Fig. 3.6a is dominated by the intense emission feature centered at 526.7 eV and accompanied by a small low energy shoulder at 525.1 eV . The low energy part of the spectrum shows a broad feature at about 522.2 eV . The spectra depicted in Fig. 3.6b show a similar overall shape, but as at the NK emission edge, the additional oxygen atoms within these amino acids contribute to the XE spectra and thus have to be considered.

Asparagine and glutamine host an additional oxygen in the amide side-chain. Aspartic acid and glutamic acid show a second carboxylic group within the side-chain and serine, threonine, and tyrosine have an additional alcohol group, respectively.

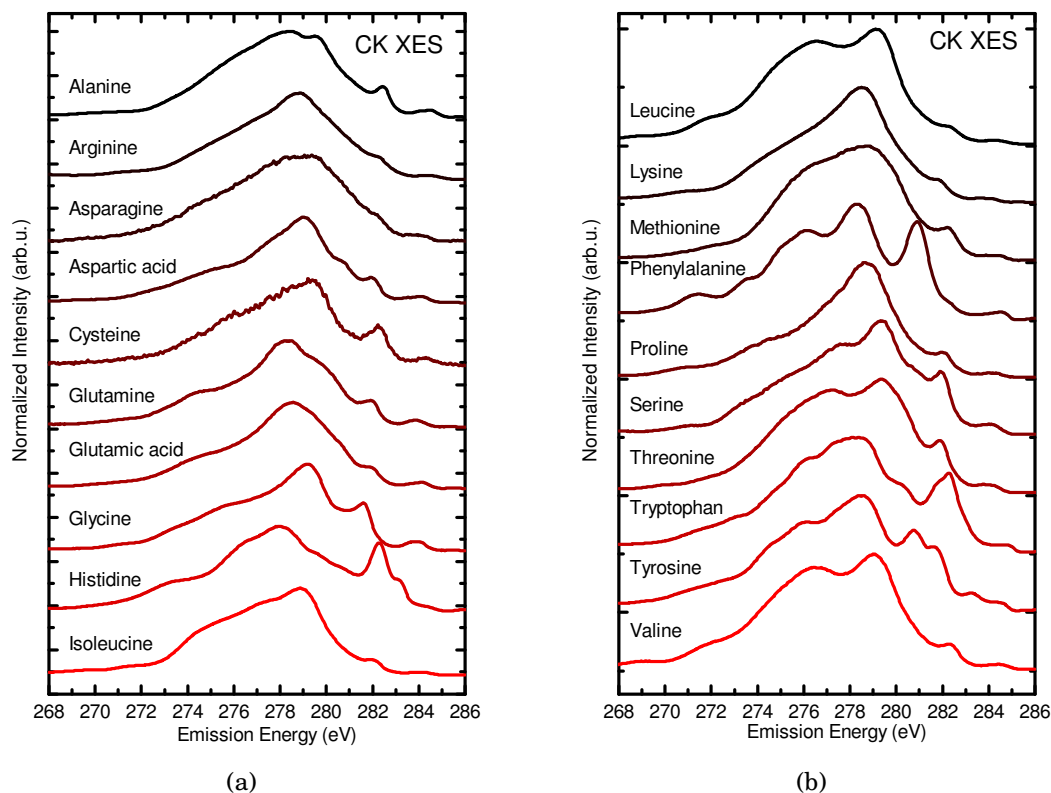


FIGURE 3.7. CK XE spectra ($E_{\text{Exc}} = 322 \text{ eV}$) of the carbon backbone of the 20 standard amino acids.

In spite of the multiple oxygen atoms, the OK spectra of these two groups look astonishingly similar. This implies that the local electronic structure surrounding the oxygen atoms is less specific for the molecule than it is the case for the nitrogen atoms. In other words, the oxygen emission spectra might be too insensitive to be used to create individual fingerprints of the 20 amino acids, which could subsequently be used to identify the specific amino acid and a larger molecular compound, as it is the case in peptides and proteins. On closer inspection an intensity ratio altered with respect to the spectra in Fig. 3.6a can be observed in the OK XE spectra in figure 3.6b. Furthermore, the width of the high-energy feature varies and additional contributions within this feature can be expected.

Not only the functional groups of the amino acids are spectroscopically accessible. The carbon atoms which are the backbone of the functional groups can also be investigated using X-ray emission spectroscopy. The CK XE spectra are displayed in Fig. 3.7. In contrast to the OK and NK XE spectra, the CK spectra show much less similarities. All spectra show the same triangular shape centered around 287 eV, but multiple unique high and low energy features are visible. Since the carbon spectra show an individual spectral fingerprint for all 20 amino acids, the fingerprints might

3.1. SPECTRAL SIGNATURE OF THE LOCAL ELECTRONIC STRUCTURE OF PROTEINOGENIC AMINO ACIDS

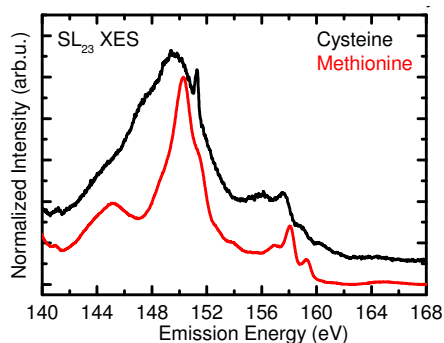


FIGURE 3.8. SL XE spectra of Methionine ($E_{\text{Exc}} = 182\text{eV}$) and Cysteine ($E_{\text{Exc}} = 202\text{eV}$).

be used to identify the amino acids in peptides or proteins.

To complete the amino acids database the sulfur $L_{2,3}$ XE spectra of methionine and cysteine are depicted in Fig. 3.8. Although both molecules host only a single sulfur atom, the sulfur $L_{2,3}$ emission spectra are quite complicated. This is due to the spin-orbit splitting of the sulfur L core level. At non-resonant excitation both states are excited creating an emission spectrum for each L core level. Hence, the spectra are the superposition of L_2 and the L_3 emission, which are basically identical, but weighted 2:1 and shifted by the spin-orbit splitting. Upon resonant excitation the L_3 emission can be excited separately from the L_2 emission which was demonstrated in [86].

All these amino acid spectra were recorded from amino acid powders (purity of 98% and higher). Therefore, the amino acids were measured in their zwitterionic configuration as it is depicted in the Fig. 3.1-3.3. The large similarities of some of the spectra imply that a spectral fingerprint of the protonated amino group and the deprotonated carboxylic group can be determined. Furthermore, by subtracting these fingerprints from the NK and OK spectra also fingerprints of the side-chains might be possible. In the following the possibility of determining unique spectral fingerprints of all functional groups of the amino acids is investigated.

3.1.1 An XES Building Block Approach on the Electronic Structure of Amino Acids

As discussed above, the spectral shapes of the emission spectra show a strong local character. This suggests that the spectra can be used as fingerprints of functional groups and that more complex amino acids like histidine or asparagine can be described as a sum of spectral fingerprints of the single functional groups.

The concept of deconvoluting complex spectra into several spectral contributions is widely used in X-ray absorption spectroscopy and photoelectron spectroscopy. In the following, this concept will be adopted and a qualitative interpretation of the spectra shown above will be given by using the building block concept.

The book, “NEXAFS Spectroscopy”, from Joachim Stöhr [28] shows comprehensively how NEXAFS spectra can be used to investigate molecular systems and how a building block model for the quantitative interpretation of the XA spectra can be applied. The book extends the usage of the model to larger and thus more complicated molecules and describes these spectra with a combination of XA spectra of much smaller molecules (building blocks). It is shown how energy position, peak intensity, and peak shape can be used as a signature for the bonding characteristics of the excited atom. The building-block method links characteristic features in the spectrum to specific bonding constellations (e.g., π^* or σ^* bonds). The XA building blocks consist of quasi diatomic “molecules” characterizing these bonds by ignoring all hydrogen atoms. Thus, in a first approximation larger molecules can be seen as an agglomeration of such diatomic building blocks.

This model was proven to “work best if adjacent ‘localized’ bonds have characteristic anti-bonding orbitals of a given symmetry that are well separated in energy, such that first-order bond-bond interactions within the π^* and σ^* manifolds are absent and second-order interactions are weak” [28, S.179]. Simultaneously, these conditions define the limits of the model. First-order bond-bond interactions are also known as “conjugation” or “delocalization”. Stöhr shows the capabilities and limits of this model. Nowadays, the building block model became a standard tool for the analysis of X-ray absorption spectra.

As described in chapter 2.1.1, X-ray emission spectroscopy (XES) and especially non-resonantly excited XES can be described as a reversed XA process. Both follow the same dipole selection rules and show the same local probing character. Thus applying a similar building-block model to XES is reasonable.

As discussed above, all amino acids shown in Fig. 3.5a and 3.6a have the same two functional groups (carboxylic and amino). However, the side-chains of all amino acids are unique, but the influence on the spectrum seems to be very small which makes this set of spectra ideal to generate a universal spectral fingerprint representing the amino

3.1. SPECTRAL SIGNATURE OF THE LOCAL ELECTRONIC STRUCTURE OF PROTEINOGENIC AMINO ACIDS

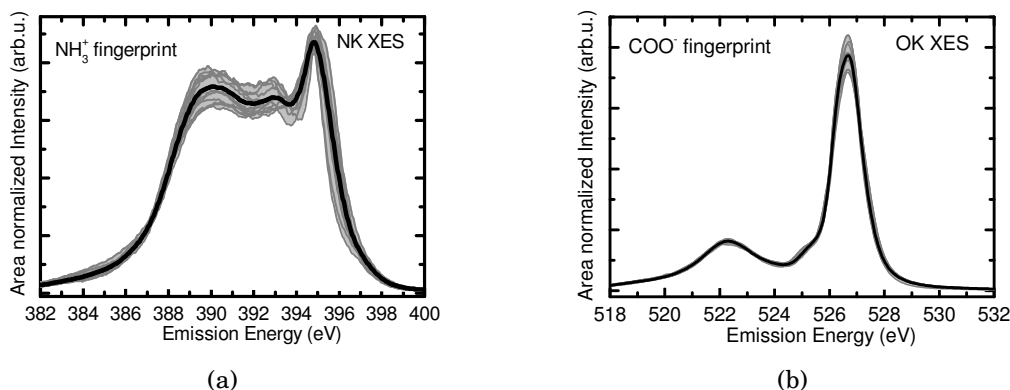


FIGURE 3.9. The black graph shows: (a) spectral fingerprint of a protonated primary amine group (NH₃⁺), (b) spectral fingerprint of a deprotonated carboxyl group (COO⁻). Determined from the superposition of all NK ($E_{\text{Exc}} = 424 \text{ eV}$) and OK ($E_{\text{Exc}} = 557 \text{ eV}$) XE spectra of Fig. 3.5a and 3.6a, respectively (dark grey).

and the carboxylic group. The fingerprint was elaborated by summing up the area-normalized spectra in Fig. 3.5a and 3.6a. The result is presented in Fig. 3.9. Fig. 3.9a displays the averaged NH₃⁺ fingerprint (black) and the individual, area normalized NK XE spectra (grey). Fig. 3.9b illustrates the same for the OK XE spectra.

The similarities within the spectra are astonishing. It can be stated that these two spectra now represent the X-ray emission fingerprint of a protonated amino group (NH₃⁺) and a deprotonated carboxylic group (COO⁻). In the following the details of these two spectra will be discussed on the example of the glycine molecule which is the amino acid with the smallest side-chain. The amino acid glycine was extensively investigated by Monika Blum *et al.* [65], which set the foundation of understanding the characteristics of the NK XE spectrum of the NH₃⁺ group.

Fig. 3.10a illustrates the NK XE spectrum of glycine (red) measured by Blum *et al.* [65]. As in literature, the spectrum was compared to ground state calculations of zwitterionic glycine in aqueous solution (black). It becomes obvious that the agreement between experimental measurement and the theoretical predictions is not very good. Only the low energy part of the spectrum is, at least partly, described by the calculation. The time-dependent DFT calculation (blue) which includes the core-hole lifetime, is in a much better agreement and also qualitatively describes the high energy side of the spectrum. Based on this findings, Blum *et al.* concluded that this disagreement is the result of an ultra-fast dissociation process on the timescale of the core-hole lifetime. In the core-excited state, the NH₃⁺ group is unstable and a proton gets ejected from the NH₃⁺ group. This ejection results in a distortion of the electronic structure surrounding the NH₃⁺. Blum *et al.* found out that within the first 5 fs the N-H bonds are elongated and within the following 5-15 fs the proton detaches from the functional

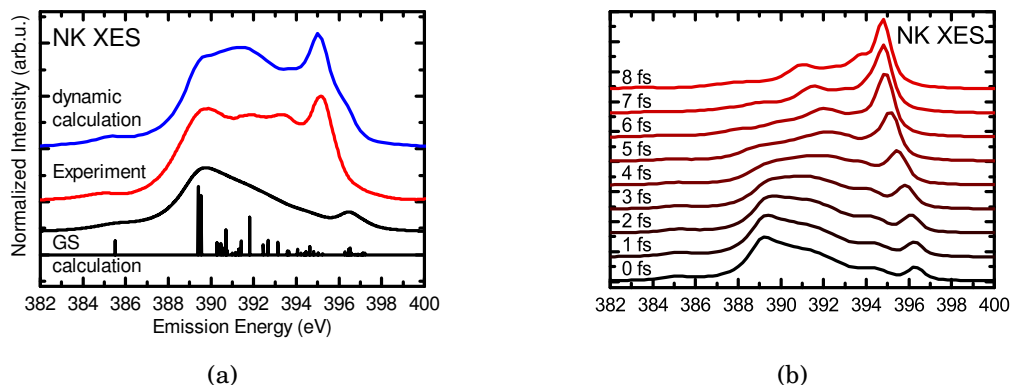


FIGURE 3.10. a) NK emission spectrum ($E_{\text{Exc}} = 420\text{ eV}$) of glycine in zwitterionic configuration (red) compared to a ground state DFT calculation (black) and a dynamic, time-dependent DFT calculation (blue). b) dynamical DFT calculations of zwitterionic glycine for different core-hole lifetimes (0-8 fs). The dynamic calculation shown in a) represents the averaged lifetime. The graphs are adopted from [65].

group and a neutral NH_2 group is formed. Fig. 3.10b shows the “snapshots” of the time-dependent DFT calculation. It nicely demonstrates the evolution of the spectrum during the dissociation process. For the dynamic calculation shown in Fig. 3.10a a weighted sum of the “snapshot” spectra with an average core-hole lifetime of 5.7 fs was estimated [65].

Besides this quantitative theoretical description, also a qualitative approach can be made. By summing up the GS calculation for the NH_3^+ spectrum and the NH_2 Blum *et al.* achieved also a very good agreement between theory and experiment. With this approach the peak observed at 395.3 eV could be identified as an emission from the NH_2 lone pair orbital [65].

The deviation from the average spectrum appears to be much larger for the NK spectra than for the OK spectra, indicating that the NK XE spectra are more sensitive to the “attached” molecule than the OK XE spectra. Fig. 3.11 shows the OK XE spectrum of glycine (black) together with a calculated spectrum of an isolated zwitterionic glycine created with the StoBe-deMon code and with the parameters introduced in the chapter above (2.2.2). The coordinates evaluated by powder diffraction measurements from Schreyer *et al.* [87] were used as geometric input. The blue spectrum shows the calculation broadened by Gaussians. For a better agreement the calculation was shifted by -0.5 eV. Black and red bars indicate the transitions into the two oxygen core levels. The calculation (red and black bars) is in a quite good agreement to the experimental spectrum (black). The calculated emission lines nicely describe the experimental spectrum. It can be seen that the intense high energy feature is the result of transitions from the HOMO orbital into the O 1s core levels. Furthermore, it can be

3.1. SPECTRAL SIGNATURE OF THE LOCAL ELECTRONIC STRUCTURE OF PROTEINOGENIC AMINO ACIDS

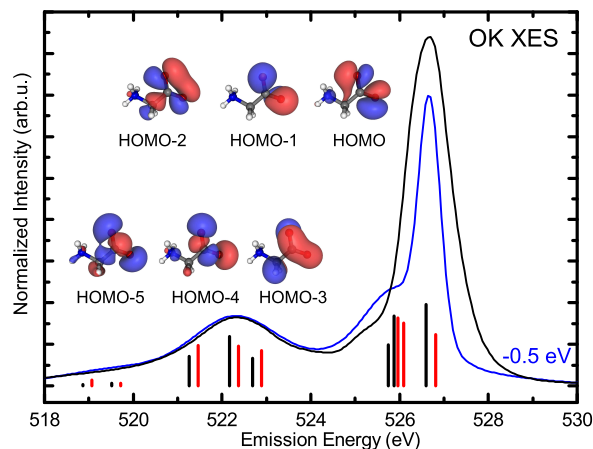


FIGURE 3.11. OK XE spectrum ($E_{\text{Exc}} = 557 \text{ eV}$) of glycine in powder form (black), calculated XE spectrum using DFT in the frozen orbitals approximation. Isodensity surfaces of the highest occupied molecular orbitals (HOMO) in ground state configuration.

seen that the weak shoulder at about 525.2 eV is formed by the HOMO-1 and HOMO-2 orbitals and the low energy feature centered at 522.2 eV represents transitions from the HOMO-3, -4, and -5. However, by broadening the calculated emission lines the experimental spectrum cannot be described completely. The intense high energy peak is much more intense and also much broader than in the DFT calculation. A reason for these differences can be the vibrational coupling of these levels which are not included in the DFT calculation

The calculation is in a fairly good agreement to the experimental spectrum. However, no averaging over different GS configurations was made, which can be seen as another explanation for the discrepancy in the width of the high energy emission feature ($E_{\text{emiss}} = 527 \text{ eV}$). The graph also shows isodensity surfaces of the 6 highest occupied molecular orbitals (HOMO). It can be seen that the 6 HOMO orbitals which form the OK XE spectrum are mainly localized at the carboxylic group and do hardly extend to the amino group. This correlates nicely with the NK GS calculation of Fig. 3.10a which shows a very low transition probability for the higher occupied molecular orbitals and a higher transition probability for the deeper bound molecular orbitals which are obviously mainly localized at the amino group.

By averaging many XE spectra (Fig. 3.9), the influence of the different side-chains is reduced and a spectral fingerprint is created that can be used to decompose the NK and OK XE spectra of amino acids which contain more oxygen and nitrogen species than just the NH_3^+ and COO^- functional groups.

In the following the determined fingerprint will be used to extract the spectral

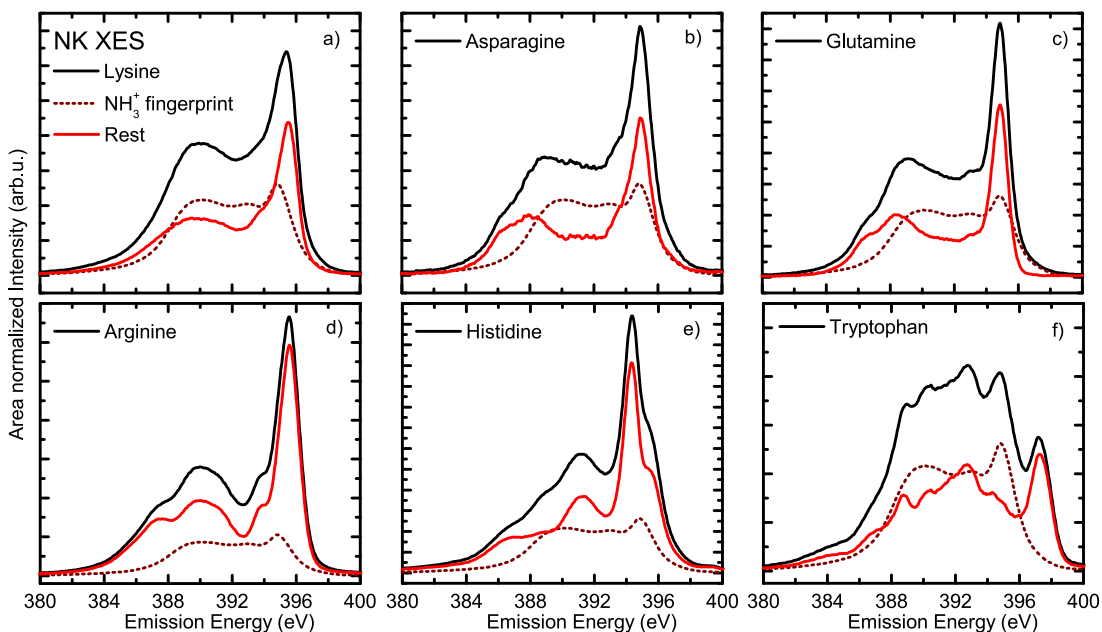


FIGURE 3.12. Evaluation of the spectral fingerprints of the non- NH_3^+ nitrogen atoms by subtracting the NH_3^+ spectral contribution (dark red) from the NK XE spectra ($E_{\text{Exc}} = 424 \text{ eV}$) of arginine, asparagine, glutamine, lysine, histidine, and tryptophan. The result is shown in red.

signatures of the nitrogen and oxygen atoms which are not present in either a NH_3^+ or a COO^- functional group, respectively. For the spectral decomposition of the different nitrogen or oxygen species, the following assumptions have to be made: Firstly, it is assumed that the single emission spectra are independent. Secondly, the integrated transition probability into the different core levels is very similar. This second assumption is not utterly true, but XES calculations of lysine and histidine have shown that this is a good first approximation and the deviation lies within 5%.

With this assumptions, the evaluated average NH_3^+ spectrum (3.9a) was subtracted from the NK XE spectra of arginine, asparagine, glutamine, lysine, histidine, and tryptophan (see Fig. 3.12). All spectra were area normalized according to their spectral weight (the number of excited atoms of the same element per functional group). For example, asparagine hosts two nitrogen atoms of which one forms the NH_3^+ amino group and the second the NH_2 group within the amide endgroup. Following this model, the area of the total spectrum is normalized to an area twice as large as the area of the NH_3^+ fingerprint. The result of the subtraction is depicted in Fig. 3.12 (red). The original NK XE spectrum is always shown in black. The subtracted NH_3^+ fingerprint is shown as a dashed, dark red line.

Within the group of spectra displayed in Fig. 3.12, lysine is the amino acid with the easiest chemical structure (see Fig. 3.12a). As already mentioned above, lysine

3.1. SPECTRAL SIGNATURE OF THE LOCAL ELECTRONIC STRUCTURE OF PROTEINOGENIC AMINO ACIDS

has only two nitrogen atoms which are both forming an amino group. In zwitterionic conformation the α -amino group is neutral while the amino group at the end of the aliphatic side-chain is protonated [73]. By subtracting the NH_3^+ fingerprint, the remaining spectrum is expected to represent the neutral amino group (NH_2). Hence, the subtraction directly produces a new spectral fingerprint. This is also the case for asparagine b) and glutamine c), which also have only one additional nitrogen atom. The subtraction of the NH_3^+ fingerprint from the asparagine and glutamine spectra. However this results in a spectrum that shows some similarities to the NH_2 spectrum of lysine but features much more intensity on the low energy side of the spectrum than lysine. These differences were already visible in the total spectra. Yet, after the subtraction they are much more pronounced. As already mentioned above, the neighboring oxygen atom can be seen as possible source of this additional intensity. Due to the double bond oxygen, the electronic structure of the NH_2 amino group seems to be highly influenced. The combination of amino group and a carbonyl group (double bond oxygen) is also known as amide group. From the chemical point of view amides create a much stronger hydrogen bonding network than amines. Although they are also easily soluble in water, *amides* are much harder to ionize than amines which results in a hardly measurable basicity. In other words, amides are only very weak bases [88].

Arginine (Fig. 3.12d), histidine (Fig. 3.12e), and tryptophan (Fig. 3.12f) have a much more complex side-chain. Starting with arginine, the functional group attached to the end of the side-chain consists of three nitrogen atoms, two amines (one primary and one secondary) and a primary *ketimine*. The entire functional group is also called *guanidine*. Due to the complexity of this functional group, the observed spectral feature cannot be assigned to a single atom. Nevertheless, the corrected spectrum of arginine shows similarities to both, lysine and asparagine/glutamine.

The side-chains of histidine and tryptophan are even more complex than the side-chain of arginine. Both show a heterocyclic ring structure. In case of tryptophan, the side-chain consists of a so called *indole* group, a heterocyclic, aromatic, double ring structure. By subtracting the NH_3^+ fingerprint, the high emission energy feature gains in intensity compared to the rest of the spectrum. The aromatic ring structure changes the spectrum dramatically and no similarities to the other amino acid spectra can be observed. The same is valid for histidine. Here the ring structure is called imidazole. Upon subtracting the NH_3^+ fingerprint, the spectrum gets more detailed, but in contrast to the other four amino acids discussed above, the intense high energy feature is red-shifted and a weaker shoulder on the high energy side of the peak is visible. Furthermore, the low energy part of the spectrum is continuously decreasing in intensity with decreasing emission. As for proline and tryptophan, the NK XE spectra cannot be compared to the other amino acids. Since the fingerprint analysis does not

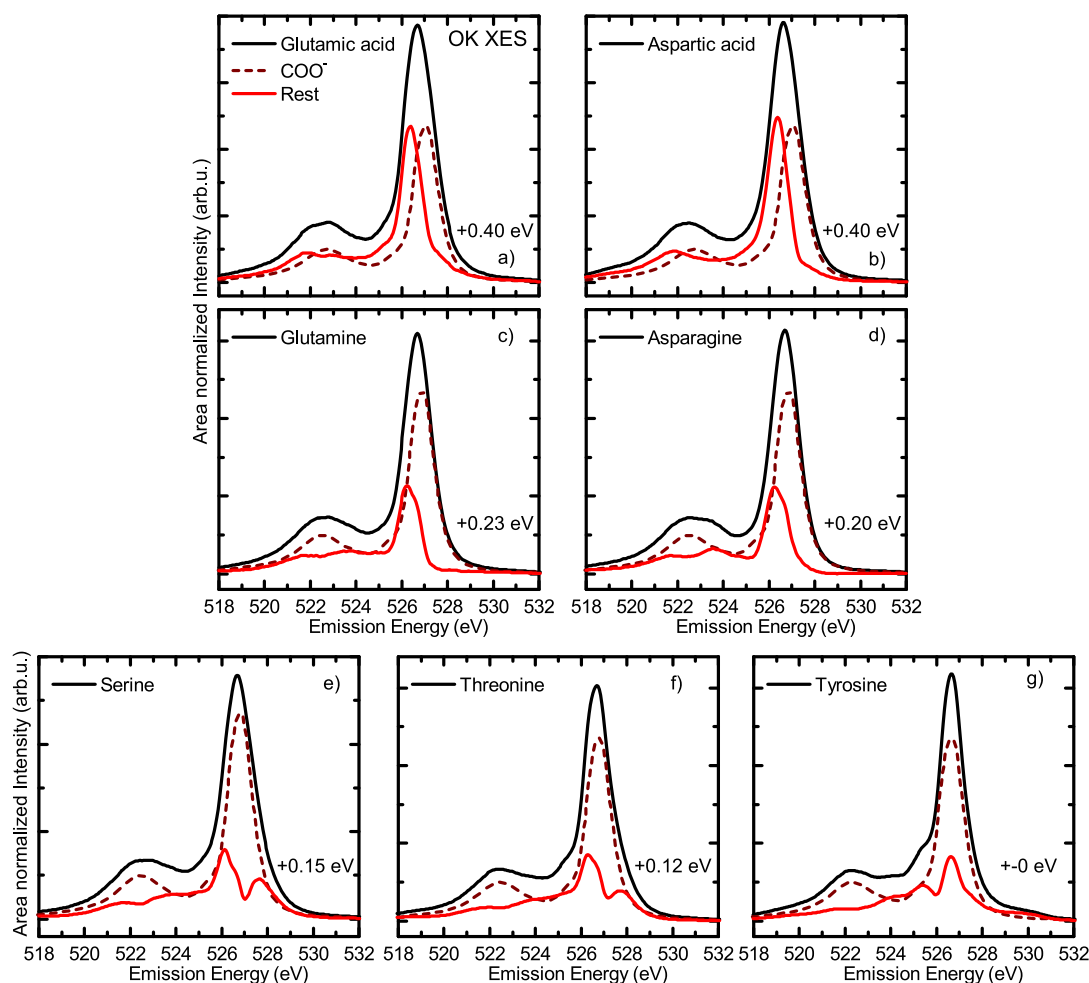


FIGURE 3.13. Evaluation of the spectral fingerprints of the non- COO^- oxygen species by subtracting the COO^- spectral contribution (dark red) from the OK XE spectra ($E_{\text{Exc}} = 557 \text{ eV}$) of asparagine, glutamine, aspartic acid, glutamic acid, serine, threonine and tyrosine. The result is shown in red.

work on histidine, proline, and tryptophan, these amino acids should be investigated in more detail. Tryptophan, however, is quite big and hardly soluble in water, which is why an in-depth analysis of these “anomalous” amino acids focuses on proline and histidine only.

A similar subtraction can now be done for the OK XE spectra of the amino acids which host more oxygen atoms than just the two within the carboxylic group. Fig. 3.13 shows the original spectra in black. The subtracted COO^- fingerprint is depicted as a dotted, dark-red line, and the result of the subtraction—a fingerprint of the side-chain—is shown in red. Again, the spectra were normalized according to the number of excited atoms (i.e., asparagine has three oxygen atoms while the COO^- fingerprint has two). To achieve a meaningful result, the COO^- fingerprint was shifted

3.1. SPECTRAL SIGNATURE OF THE LOCAL ELECTRONIC STRUCTURE OF PROTEINOIGENIC AMINO ACIDS

in energy. The energetic shifts are written in the graphs.

The top two graphs illustrate the amino acids glutamic acid a) and aspartic acid b). The COO^- fingerprint was shifted by +0.40 eV. This results in a spectrum that is, apart from a red shift of about -0.7 eV, almost identical to the COO^- fingerprint. These similarities are easily understandable since the side-chains of both amino acids consist of a deprotonated carboxylic group similar to the α -carboxylic group. The energetic shift between these two functional groups might be seen as an indicator for the functional group's acidity (its possibility to lose a proton), which is lower for the side-chain than for the α -carboxylic group.

Fig. 3.13c and 3.13d show the spectra of glutamine and asparagine. Introducing the energetic position of the COO^- fingerprint as additional parameter makes the data evaluation more complicated. For both amino acids two meaningful solutions could be obtained. Solution one is achieved by shifting the COO^- fingerprint by +0.23 eV and +0.20 eV, respectively. They are also depicted in Fig. 3.13. The second solution is obtained when no shift is applied (not shown). In both cases, the side-chain of glutamine and asparagine is an amide group (CONH_2). Due to the broad features obtained, both solutions show significant similarities with photoemission spectroscopy data on gas phase acetamide [89]. For an in-depth evaluation of the constructed side-chain fingerprints, a comparison to calculations or OK XE spectra of acetamide has to be done. Nevertheless, similar to the spectra of glutamic acid and aspartic acid, the spectra of glutamine and asparagine are almost identical, which again supports the validity of the building block approach.

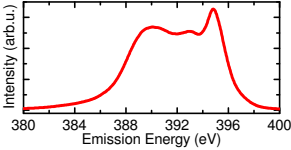
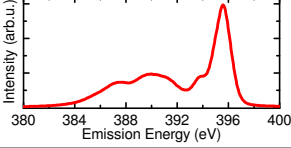
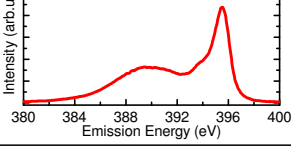
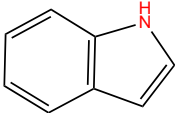
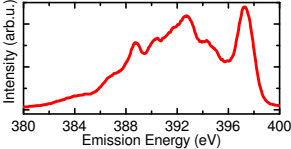
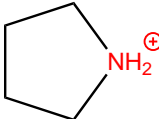
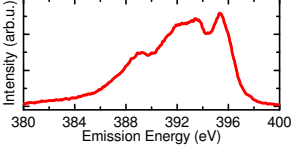
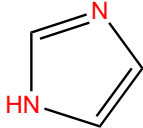
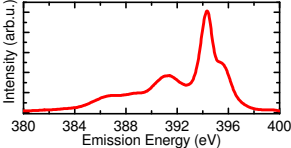
The bottom row of graphs depicted in Fig. 3.13 illustrates the OK XE spectra of serine (3.13e), threonine (3.13f), and tyrosine (3.13g). The side-chains of all three amino acid host, besides carbon atoms, only a single hydroxide group (OH). However, two different spectral fingerprints are obtained for the side-chains. For serine the subtracted COO^- fingerprint was shifted by +0.15 eV and for threonine by +0.12 eV. In case of tyrosine the best result was obtained when no shift was applied. In case of serine and threonine the resulting spectra are almost identical showing a pronounced double peak structure. Tyrosine shows a similar spectrum but the intensity ratio within the double-peak structure is reversed. The comparison of the side-chain spectrum (R-OH) to simpler molecules hosting a hydroxide group (methanol, water) exhibits large deviations. Especially serine and threonine, for which the highest intensity is obtained at around 526.3 eV, show only minor similarities with a non-resonantly excited OK XE spectrum of methanol measured by Benkert *et al.* [90] and Nordgren *et al.* [91]. These differences are an interesting starting point for further investigations of the spectral fingerprints and the validation of the building block model.

Although the subtraction is prone to errors and the obtained fingerprints of the different functional groups have to be validated in an in-depth analysis, the building

CHAPTER 3. X-RAY SPECTROSCOPY OF PROTEINOGENIC AMINO ACID FILMS AND SOLUTIONS

block model proofs to be a quite useful tool for qualitative analysis of x-ray emission spectra.

These spectral fingerprints can now also be summarized in a library by linking them to the respective functional groups. Table 3.1 summarizes all fingerprints including the molecular configuration surrounding the probing atom(s) and proposes possible smaller reference molecules representing the bare functional group. The zwitterionic configuration of the amino acids leads to the fact that the comparison to possible reference molecules is not straight forward, since these molecules are usually electronically neutral. The easiest way to change the charge state of amino acids is by solving them in an aqueous solution and adjusting the pH-value. By adjusting the pH-value all possible charge states become experimentally accessible (see Chapter 3.1.2 below).

Amino Acids	Functional Group	Spectral Fingerprint	Potential Reference Molecule
All	$R-NH_3^+$		Methylammonium Salt
Arginine	$R-NH-C(=NH_2^+)-NH_2$		Guanidine Guanidinium cation
Lysine	$R-NH_2$		Methylamine
Tryptophan			Indole
Proline			Pyrrolidine
Histidine			Imidazole

3.1. SPECTRAL SIGNATURE OF THE LOCAL ELECTRONIC STRUCTURE OF PROTEINOGENIC AMINO ACIDS

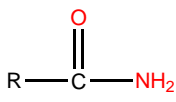
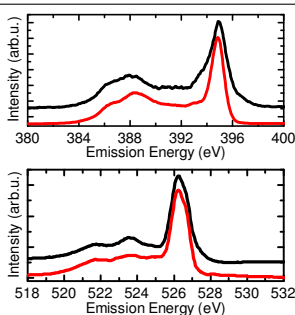
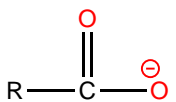
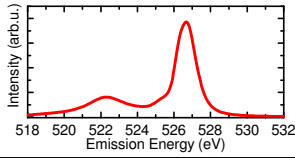
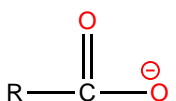
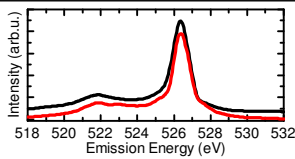
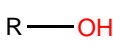
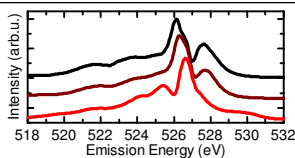
Amino Acids	Functional Group	Spectral Fingerprint	Potential Reference Molecule
Asparagine Glutamine			Acetamide
All			Formate ion Acetate ion
Aspartic acid Glutamic acid			Formic acid
Serine Threonine Tyrosine			Methanol

Table 3.1: Summary of the functional groups of the 20 proteinogenic amino acids shown with its respective XE fingerprint extracted from the XE library using the building block approach. To each functional group, chemically suitable reference molecules are proposed.

3.1.2 The Building Block Approach Applied to Histidine and Lysine

In this chapter the applicability of the building block model and the spectral fingerprints will be examined in the example of the NK XE spectrum of lysine and histidine.

As already mentioned in the introduction of this chapter, the zwitterionic state of lysine is different from the zwitterionic state of most of the other amino acids. As depicted in Fig. 3.14a, the α -amino group is neutral, while the amino group of the side-chain is protonated (NH_3^+). This, however is only valid in aqueous solution. In crystalline form also the complementing configuration is observed (b, [92]). The characteristics of a protonated and a deprotonated amino group was already addressed in several studies, including work done in our group [65, 73, 74, 93].

It was found out by Messer *et al.* [93] that the NK XA spectrum of lysine is a superposition of two contributions. By applying the XAS building block principle, they could nicely show that the XA spectrum of lysine can be described by the average sum of an XA spectrum of protonated and one neutral glycine. The XE building block approach introduced above suggests that also the XE spectrum of lysine can be separated into two contributions and compared separately to suitable reference molecules. In the following, suitable reference molecules for the description of the neutral amino group spectrum will be identified.

The NK emission spectrum of histidine is much richer in spectral details than the spectrum of lysine. Nevertheless, in this chapter it will be shown that the spectral fingerprint method can be used successfully to separate the contribution of the side-chain and the α -amino group. The side-chain of histidine belongs to the chemical group of aromatic heterocycles and is named imidazole. A more detailed description of the molecule is given in chapter 3. Below, the building block approach will be tested by comparing the spectrum of lysine to spectra of methylamine, glycine at pH 12, and

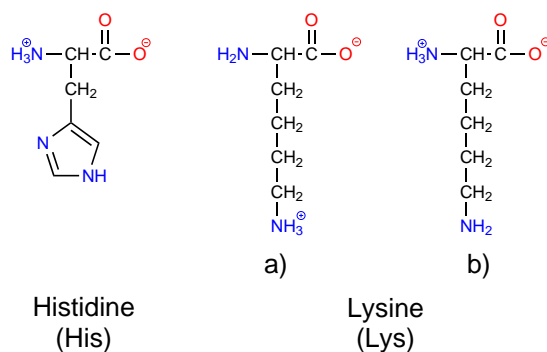


FIGURE 3.14. Structure of the two amino acids histidine (His) and lysine (Lys).

3.1. SPECTRAL SIGNATURE OF THE LOCAL ELECTRONIC STRUCTURE OF PROTEINOGENIC AMINO ACIDS

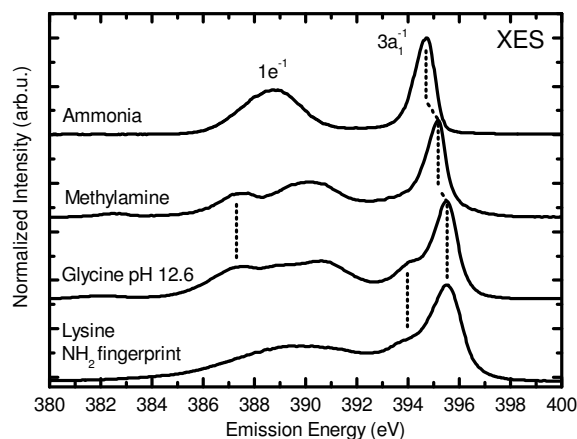


FIGURE 3.15. NK XE spectra ($E_{\text{Exc}} \approx 420 \text{ eV}$) of liquid ammonia, gas phase methylamine, aqueous glycine at pH 12.6 adopted from [65], and the NH_2 fingerprint of Lysine.

ammonia (as reference molecule), as well as histidine to the spectrum of imidazole (as reference molecule). The reference molecules were chosen by the chemical structure of their functional groups, even though this means that the reference molecule has a different phase than the solid amino acid.

Lysine

Fig. 3.15 shows the NK emission spectra of aqueous ammonia (NH_3) [77], gas-phase methylamine ($\text{CH}_3 - \text{NH}_2$), aqueous glycine at pH 12.6 ($\text{C}_2\text{H}_3\text{O}_2 - \text{NH}_2$), and the NH_2 group of solid lysine after the subtraction of the NH_3^+ fingerprint. The ammonia spectrum was recorded by Weihardt *et al.* [77] measuring a saturated aqueous solution in the liquid cell described above. Methylamine was measured in the gas phase in the framework of this thesis using the custom-built gas cell [9]. The glycine was measured by Blum *et al.* [65]. The NH_2 spectrum of lysine was extracted from the solid state measurements by subtracting the NH_3^+ fraction.

The ammonia spectrum shows emission from only two valence orbitals, namely with $1e^{-1}$ and $3a_1^{-1}$ valence hole final state. The $3a_1^{-1}$ emission line corresponds to the lone pair orbital which is less vibrationally coupled and hence narrower than the two $1e^{-1}$ bonding orbitals. The lower lying $2a_1^{-1}$ orbital is not shown. The emission energies of the two visible valence orbitals are 394.72 eV ($3a_1^{-1}$) and 388.73 eV ($1e^{-1}$).

In a second step the reference molecule will now be extended. Besides the local geometry, also the right nearest neighbors are now included. The smallest molecule that fulfills these conditions is methylamine CH_5N , in which the amino group is attached to a methyl group. The NK emission spectrum of methylamine consists of

four clearly visible emission lines located at 395.2 eV, 390.2 eV, 387.4 eV, and 382.5 eV. The highest intensity is observed for the high energy line at 395.2 eV.

In a third step the reference molecule also includes the carboxylic group. For glycine pH 12.6 the energetic position of the high energy peak shifts again to higher emission energies (395.5 eV) and a shoulder at 394.0 eV appears. Furthermore, since the number of atoms is increased also the number of orbitals and thus the number of transitions (between ≈ 392 eV and ≈ 382 eV) increases which results in a broader intensity in this energy region. However, a single feature stands out of this broad intensity (387.4 eV) and matches with a similar feature in the methylamine spectrum.

In a last step the spectra can now be compared to the NH_2 fingerprint of lysine. The intensity between ≈ 392 eV and ≈ 382 eV is even broader than for glycine and the feature at 387.4 eV vanishes. Nevertheless, the high energy feature is almost identical to glycine (high intensity at 395.5 eV and a weak shoulder at 394.0 eV).

On the one hand, “increasing” the reference molecule—from ammonia to glycine—has several effects on the NK XE spectrum. Firstly, the high energy peak, which can be related to the lone pair orbital (for ammonia), shifts successively to higher emission energies. Secondly, for the two amino acids which also host a carboxylic group a shoulder appears at 394.0 eV. Thirdly, the broad low energy part of the spectrum associated with the $1e^{-1}$ orbitals broadens and splits up into several features. On the other hand, some spectral features are “preserved” throughout the measurement series.

Hence, the features visible in the lysine spectrum can be assigned the following. The high energy features (395.5 eV) corresponding to the highest occupied molecular orbital (HOMO) is strongly influenced by the “lone pair orbital” or the nitrogen. The shoulder at 394.0 eV can be seen as an indication for the presence of a carboxylic group (in the direct vicinity). The broad feature centered at about 390.0 eV can be attributed to orbitals with a local $1e^{-1}$ - like symmetry at the nitrogen atom.

Histidine

The side-chain of histidine is much more complex than the side-chain of lysine hosting two nitrogen atoms with a very different local environment compared to that of lysine. As it could already be observed in Chapter 3.1.1, the delocalized ring structure strongly influences the spectrum. As a consequence of the influence and the complexity of the side-chain, the entire imidazole molecule has to be considered as reference molecule.

Fig. 3.16 shows the NK emission spectra of histidine and imidazole in aqueous solution at pH 10.3, as well as the NH_3^+ spectral fingerprint. By subtracting the NH_3^+ fingerprint from the spectrum of histidine, the spectral contribution of the imidazole functional group (side-chain) can be separated. The comparison of the

3.1. SPECTRAL SIGNATURE OF THE LOCAL ELECTRONIC STRUCTURE OF PROTEINOGENIC AMINO ACIDS

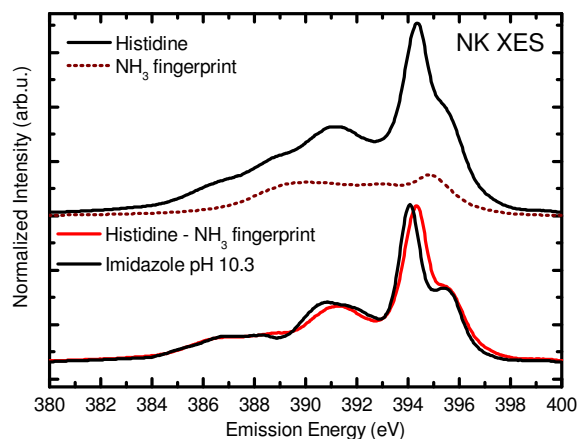


FIGURE 3.16. NK emission spectra ($E_{\text{Exc}} = 424 \text{ eV}$) of histidine, the NH_3^+ fingerprint, and imidazole in aqueous solution at $\text{pH}=10.3$. The difference between the spectrum of histidine and the NH_3^+ fingerprint is shown in comparison with the spectrum of imidazole.

imidazole spectrum (black) with this spectrum of the histidine side-chain (red) shows remarkable similarities. Apart from a 200 meV shift in the energy position of the dominating emission feature and some additional intensity around 390 eV, the spectra are almost identical.

This example demonstrates the applicability of the fingerprint approach and validates the NH_3^+ spectral fingerprint. Note that due to its delocalized electronic structure, the hetero-cyclic imidazole side-chain of histidine has to be treated as a unity and cannot be subdivided into smaller building blocks. This is similar to the XAS building block approach, where delocalized π -systems and degenerated orbitals have to be treated as one unit [28].

3.1.3 DFT Calculations of the Electronic Structure of Histidine and Lysine

The previous chapter shows that the fingerprint approach works very well for the qualitative description of the NK emission spectra of lysine and histidine. As expected, the fingerprint analysis has its limitations. One limitation becomes obvious at the oxygen emission spectra of lysine and histidine. The formate ion or the acetate ion both are only stable in aqueous solution. While such solutions were measured by Monika Blum in the SALSA setup [73], the OK emission of water dominates the spectrum and “buries” the spectra of the ions. Furthermore, the CK emission spectrum is quite complicated and unique for all amino acids. In both cases, the interpretation of the spectra cannot be done by experimental results alone. Here, computational methods

are very helpful to draw information from oxygen and carbon emission spectra in order to assign spectral features to single orbitals and determine their symmetries. The XE spectra were generated using the StoBe-deMon code (see chapter 2.2.2).

Histidine

In the framework of this thesis a first principle calculation of an isolated histidine molecule in zwitterionic configuration was performed. Since the zwitterionic configuration of histidine is not present in the gas phase, an isolated zwitterionic molecule does not represent the relaxed ground state. To prevent the calculation from relaxing into the ground state during the geometry optimization process, the relative positions of the nitrogen and the three hydrogen atoms of the protonated α -amino group (N1) were kept fix. The relative coordinates of the NH_3^+ was determined by calculating the geometry optimization for an isolated ammonia molecule (NH_4^+).

The zwitterionic configuration with labeled atoms is depicted in 3.17a. Carbon atoms are shown in grey, oxygen atoms in red, nitrogen atoms in blue, and hydrogen atoms in white. Fig. 3.17b shows the NK XE spectrum of histidine (black). Calculated transition energies and oscillator strengths are plotted as colored bars underneath the spectrum. The bars are color coded with respect to the excitation site. N1 (blue) represents the oscillator strength for the transition into the nitrogen atom of the α -amino group, while N2 (black) and N3 (red) represent the oscillator strength for the transitions into nitrogen atoms of the imidazole ring. The agreement between calculation and experiment is good, but the theory either strongly underestimates the intensity of the high energy features, or strongly overestimates the low energy part of the spectrum. The reason for the disagreement becomes visible by deconvoluting the single spectral components.

Fig. 3.17d shows the spectral fingerprint of the α -amino group together with the calculation of the α -amino group of histidine (N1). It can be observed that the calculation does not describe the high energy part of the spectrum. Only the low energy part is covered by the calculation. As it was discussed in Fig. 3.10, Blum *et al.* explained the lack of agreement with dynamical processes occurring during the measurement process. This interpretation is supported by experimental [73] as well as theoretical work [65]. The disagreement observed in Fig. 3.17 is not surprising since dynamical processes are not included in this level of theory.

In contrast, the agreement between the N2 and N3 calculation and the fingerprint of the side-chain of histidine is again very good (Fig. 3.17f), which indicates that this part of the spectrum is not influenced by dynamical processes. The calculation also reveals that the two dominant features of the spectrum belong to transitions from valence orbitals into two energetically non-equivalent nitrogen 1s core levels of

3.1. SPECTRAL SIGNATURE OF THE LOCAL ELECTRONIC STRUCTURE OF PROTEINOGENIC AMINO ACIDS

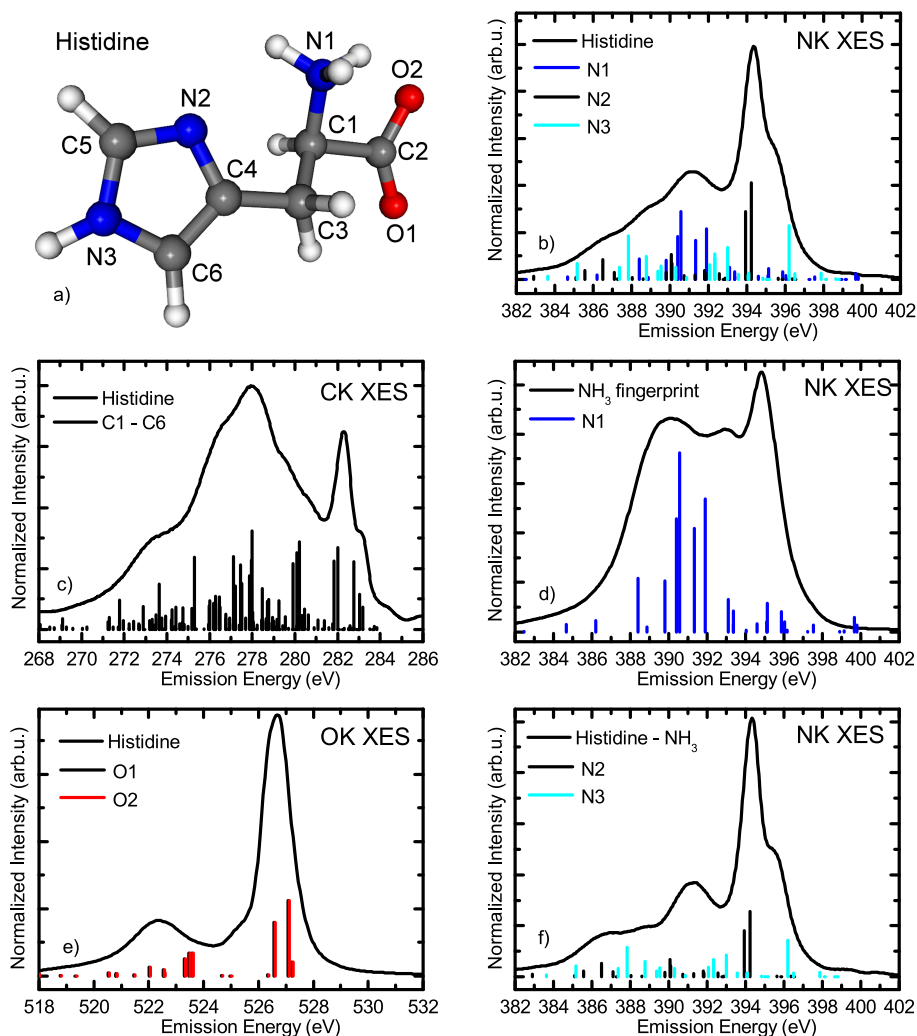


FIGURE 3.17. a) Geometry of histidine used for the calculation. XES spectra of histidine (b, c, e) and calculated transition probabilities (bars). d) Spectrum of the NH_3 -fingerprint with calculation of the α -amino group of histidine (blue bars). f) NK XE spectrum of Histidine corrected by the NH_3 -fingerprint with calculated transition probabilities into nitrogen 1s core levels of the imidazole ring (N2, N3). Excitation energies of the experimental spectra: OK: $E_{\text{Exc}} = 557 \text{ eV}$, NK: $E_{\text{Exc}} = 424 \text{ eV}$, CK: ($E_{\text{Exc}} = 322 \text{ eV}$).

the imidazole ring. Furthermore, the calculation shows that the feature at 395.5 eV originates from a single HOMO-4 to N 1s transition at the N3 site, while the sharp feature at 394.3 eV is caused by two transitions (HOMO-4 and HOMO-5 to N 1s of the N2 site).

Spectra and calculations of the CK and OK emission are depicted in Fig. 3.17c and 3.17e, respectively. In both cases, calculation and experiment are in a good agreement. The calculation of the CK spectrum consists of 6 independent calculations, one for

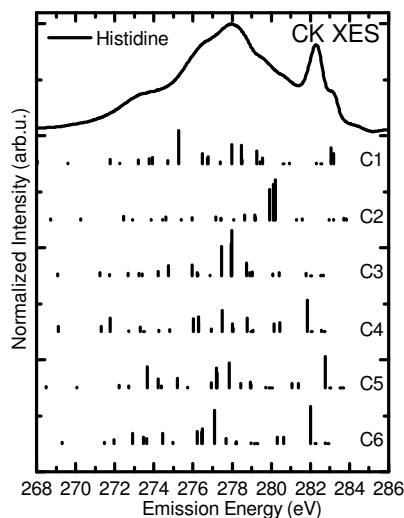


FIGURE 3.18. CK XE spectrum ($E_{\text{Exc}} = 322 \text{ eV}$) of solid zwitterionic histidine (black line) compared to calculated transition probabilities into the different carbon core holes.

each of the 6 non-equivalent carbon atoms. The strong dependency of the transition probabilities on the chosen core level site implies a strong orbital localization. This can nicely be seen in Fig. 3.18, which shows the CK XE spectrum of histidine and the calculated emission lines for transitions into the different carbon core holes. The calculation indicates that the high energy part of the spectrum (between 281 eV and 284 eV) is dominated by transitions into the C1, C4, C5, and C6 core levels. Furthermore the calculation also reveals that only the HOMO and the HOMO-1 orbitals have a significant non-zero transition probability with the C1 atom. Moreover, the sharp features at 282.3 eV and 283.0 eV can be solely attributed to the HOMO-4 orbital, which is highly localized on the imidazole side-chain. This is in accordance to the findings in the NK XE spectrum.

Fig. 3.17e illustrates the OK emission of histidine (black), with the black and red bars indicating the calculation of the O1 and O2 oxygen atoms. Both atoms are almost identical, which is also reflected in the calculation. The calculation describes the experiment quite well, although the energy position of the main features slightly deviates from the experiment. The main emission feature located at 526.7 eV can be assigned to transitions of the HOMO-1 and HOMO-2 orbitals into the two O 1s core levels. The low energy shoulder at 525.4 eV is not described in the calculation and the energies of the transition with lower emission energies are about 1 eV too high.

The discrepancies in the OK emission spectrum are most likely related to the calculation of an isolated molecule for which interactions with neighboring atoms are neglected. In solid phase the amino acid form salt crystals for which hydrogen bonds are present between the COO^- and the NH_3^+ group, which might already explain the

3.1. SPECTRAL SIGNATURE OF THE LOCAL ELECTRONIC STRUCTURE OF PROTEINOIGENIC AMINO ACIDS

deviations. Furthermore, the deprotonated carboxylic group is known to be a very good hydrogen bond acceptor [94, 95]. Hence the differences between calculation and experiment might be an indicator for a hydrogen bond linked to the carboxylic group of histidine.

Lysine

Fig. 3.19 shows the results of the calculations for the lysine molecule. The calculated geometry is depicted in Fig. 3.19a and reflects the zwitterionic lysine molecule in crystalline form. The atomic positions were determined by Williams *et al.* using powder diffraction [92]. The atoms show the same color code as for histidine (carbon grey, nitrogen blue, oxygen red, and hydrogen white).

As for histidine, an isolated zwitterionic molecule was calculated. The NK XE spectrum of lysine and the corresponding calculations are depicted in Fig. 3.19b. The calculation shows several transitions for the low energy region of the spectrum, but only a single transition for the high energy peak at $E_{em}=395.4$ eV. The spectrum of the NH_3^+ -fingerprint is again depicted in Fig. 3.19d. The calculation of the protonated (N1) nitrogen of lysine shows the same result as the protonated (N1) nitrogen of histidine. For both molecules the calculations are not able to successfully describe the high energy part of the spectrum. The lack of agreement can be explained by the static calculation, which does not account for dynamical processes. Fig. 3.19f shows the NK emission of lysine with the subtracted NH_3^+ fingerprint. Following the building block model, the resulting spectrum is attributed to the neutral amino group (NH_2 , N2). The calculated transition energy for the dominating feature is about 0.4 eV smaller than observed for the experiment. Furthermore, the low energy part of the spectrum is a bit underestimated by the calculation. However, the fair agreement supports the building block method.

The carbon emission spectrum of lysine is illustrated in Fig. 3.19c. Black bars indicate the calculated oscillator strength for transitions into the six carbon 1s core levels (C1- to C6). The calculation reveals that the small but distinct feature at $E_{em}=284.0$ eV originates from transitions of the HOMO-2 orbital C2 core level. The shoulder at $E_{em}=281.9$ eV is rather the result of multiple transitions. The calculation describes the overall shape of the experimental spectrum very well.

Fig. 3.19e shows the OK emission spectrum of lysine (black) with the calculated transition probabilities of the O1 (black bars), and the O2 (red bars). The HOMO, HOMO-1, and HOMO-2 orbitals show strong transition probabilities for both core holes (O1, O2), which nicely fit to the observed strong emission feature. By shifting the calculation by about -0.3 eV the agreement becomes even better. The HOMO-5 emission seems to be overestimated by the calculation.

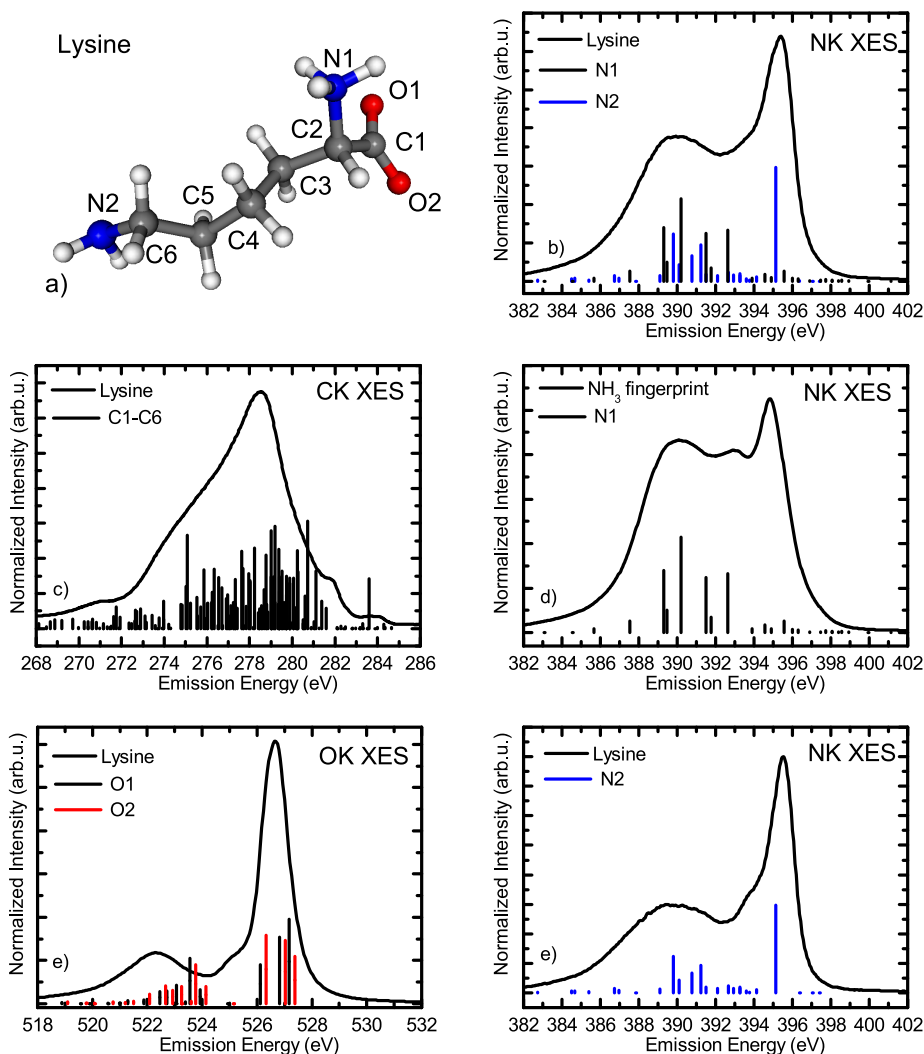


FIGURE 3.19. a) Geometry of lysine used for the calculation [92]. XE spectra of lysine (b, c, e) and calculated transition probabilities (bars). d) Spectrum of the NH_3^+ -fingerprint with calculation of the protonated amino group of lysine (blue bars, N2). f) NK XE spectrum of lysine corrected by the NH_3^+ -fingerprint with calculated transition probabilities into nitrogen 1s core level of the α -amino group (N2).

3.1.4 Summary

In this chapter a non-resonantly excited XES database of all 20 proteinogenic amino acids at all relevant emission edges is presented. Due to large similarities between the spectra at the different emission edges, a building block model for the qualitative description of the XE spectra is introduced. A spectral fingerprint of the protonated amino group NH_3^+ and the deprotonated carboxylic group COO^- could be acquired. By subtracting these fingerprints from the NK and OK XE spectra, the fingerprints

3.1. SPECTRAL SIGNATURE OF THE LOCAL ELECTRONIC STRUCTURE OF PROTEINOGENIC AMINO ACIDS

of the side-chains which also contain nitrogen and oxygen atoms could be acquired. By this procedure, a small library of spectral signatures of the functional groups of the 20 proteinogenic amino acids and suitable reference molecules could be proposed. On the example of lysine and histidine the subtraction procedure was tested by comparing the resulting side-chain spectra to suitable reference molecules (imidazole, methylamine). In both cases the spectra of the suitable reference molecule are in a very good agreement to the spectra of the amino acids confirming the applicability of this building block model. It could be shown that the XE spectra of the amino acids can be described by a superposition XE spectra of suitable reference molecules representing the bare functional groups of the amino acid. Furthermore, the NH₂ fingerprint of lysine was compared to reference molecules of different size, symmetry, and nearest neighbors. It was found that the spectral fingerprint of a large molecule like lysine is already well described if all neighboring atoms to the excitation site are present in the molecule.

In a second step the XE spectra of histidine and lysine were compared to spectral DFT calculations of isolated zwitterionic molecules. By modeling the experimental spectrum, the calculation allows to identify single orbitals which create specific features in the experimental spectrum. This method completes the qualitative analysis of the XE spectra using the building block model. Moreover, the time-independent DFT calculation does not account for any dynamical processes which are often present in the XE spectra (see Fig. 3.19d). Only sophisticated and challenging theoretical calculations are able to describe such processes. In this case the building block approach combined with time-independent DFT calculations provides a rather easy method to analyze the XES data in a qualitative way.

3.2 RIXS study of Proline and Pyrrolidine Solutions

The amino acid proline exhibits an α -amino group which is different from the other α -amino groups because it is connected to the aliphatic side-chain.

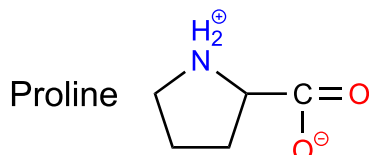


FIGURE 3.20. Zwitterionic configuration of the amino acid proline.

The back-connection of the side-chain creates a hetero-cyclic carbon hydrate structure. This nitrogen containing ring structure is also called pyrrolidine. In the following chapter the amino acid proline will be subject of detailed investigations. It will be examined as a solid and in aqueous solutions. While the previous sections are based on the non-resonant excitation, this study includes XAS and RIXS allowing the investigation of occupied and unoccupied electronic states. The XPS data was measured in the laboratory in Würzburg using an ultra-high vacuum chamber with a base pressure of $< 2 \cdot 10^{-10}$ mbar. The used electron analyzer was a VG CLAM 4. As X-ray source the Mg K_{α} line of a non-monochromatized twin-anode was used. All XPS data was recorded with the help of Judith Thoma and Dirk Hauschild.

3.2.1 Proline Powder

For the detailed study of the electronic structure proline, the samples were not prepared as pressed powders as it was done for the library shown above. To ensure a highly homogeneous sample, the amino acid was evaporated in ultra high vacuum ($10^{-6} - 10^{-8}$ mbar) with a Knudsen type evaporator onto a polished copper sample holder. The sample holder has the size of 1×0.5 inch. Such a large sample size is mandatory since the organic film has to be moved within the synchrotron beam to reduce the exposure time. The thickness of the film was chosen to be of about $1.2 \mu\text{m}$. At this thickness nearly all radiation will be absorbed within the sample. As evaporation temperature, 413 ± 1 K was chosen.

The thickness and surface roughness of the evaporated films were verified by profilometer measurements (DEKTAK 150 from Veeco) on test samples with a thickness of about 400 nm. These samples showed a surface roughness of less than 10% of the total film thickness.

To verify that the molecule is not destroyed during the evaporation (at 413 K) and

no contamination of the sample film occurred, the stoichiometry of the sample was measured with X-ray photoelectron spectroscopy (XPS). XPS offers two possibilities to verify a successful evaporation.

Firstly, by measuring the intensity ratio of the XPS signals (C1s, N1s, O1s) and performing a stoichiometric analysis. The stoichiometric analysis of the sample gives a C/N ratio of 5.3 ± 0.5 , a N/O ratio of 0.54 ± 0.05 , and an O/C ratio of 0.35 ± 0.04 . Theoretically expected ratios are: C/N = 5, N/O = 0.5, and O/C = 0.4. The oxygen to carbon ratio slightly exceeds the measurement error indicating a too small oxygen content.

Secondly, by measuring the chemical shift within the carbon 1s core level spectrum. Each of the carbon 1s core levels has a specific energy position according to the chemical bonding partners. The carbon 1s XPS spectrum (black) is depicted in Fig. 3.21 and is fitted with four Gaussian shaped peaks (grey). Features 1, 2, and 4 represent the emission from the carbon atoms 1, 2, and 4, while feature 3 represents the emission of the two chemically equivalent carbon atoms 3 (double intensity). The width, shape, and intensity ratio of all features were kept fix during the fit, whereas the peak position was variable. The sum is shown in red. The fitted energy positions of the single carbon peaks are : $C_1 = 289.5$ eV, $C_2 = 287.7$ eV, $C_4 = 287.5$ eV, and $C_3 = 286.6$ eV. The energy positions are in good agreement to other solid state measurements [1], but are shifted with respect to gas phase measurements [96].

The excellent agreement between experiment and fit indicates a successful evaporation process. For the RIXS studies, the samples were sealed in nitrogen atmosphere and shipped to the Advanced Light Source (ALS), where they were directly transferred into the measurement chamber.

Exposing an organic film to intense X-ray radiation causes an irreversible decomposition of the molecules, especially with an intense and highly focused synchrotron

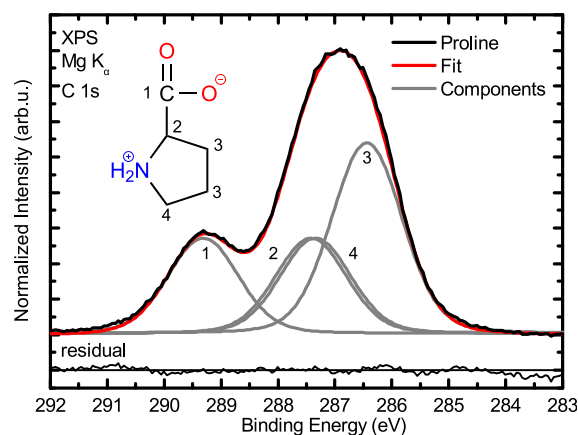


FIGURE 3.21. C1s XPS spectrum of proline. Fit of the spectrum with four Gauss profiles according to the four individual carbon species.

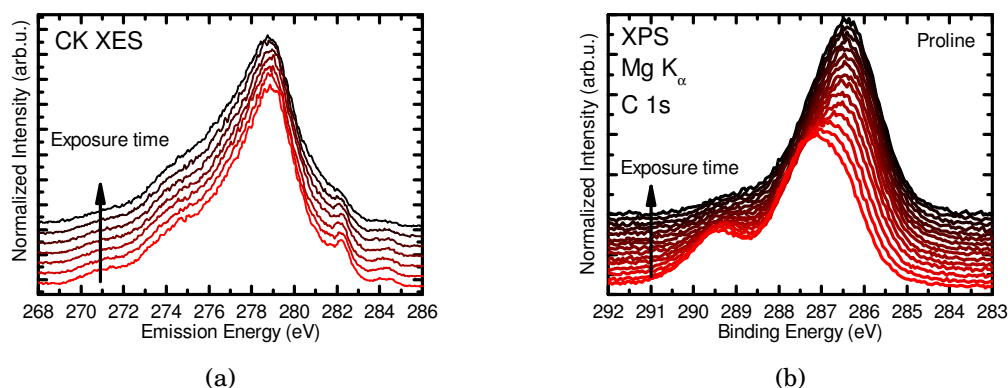


FIGURE 3.22. a) CK XES ($E_{\text{Exc}} = 322 \text{ eV}$) spectrum of proline as a function of exposure time. b) C1s XPS spectra of proline as a function of exposure time.

beam like at beamline 8.0 at the ALS. To avoid an influence of this “beamdamage” on the measurement, the amino acid film was continuously scanned. By scanning the sample, the exposure time per sample spot can be reduced to 0.1 s.

Fig. 3.22a shows the evolution of the carbon emission spectrum with increasing exposure time (exposing the sample to the intense synchrotron radiation). The red line corresponds to an exposure time of 0.14 s and the black line to an exposure time of 1 s per sample spot. Within the measurement series, the changes in the overall spectral shape are small, but it can be clearly seen that for large exposure times the fine structure at 282 eV vanishes. The triangular shape of the black spectrum indicates that the molecule is not completely destroyed. For a complete destruction it is expected that only amorphous carbon remains on the sample plate, while all the other elements leave the sample as gas. Long term exposure measurements have shown that the triangular shape transforms after 50 s and is vanished after 100 s (spectra not shown) [97].

Fig. 3.22b shows the evolution of the C1s core levels as a function of exposure time to a regular Mg K_{α} laboratory source. The red line was measured after 14 min, while the black line shows the sample after 266 min. The measurement series shows a clear trend. The spectrum of the “fresh” sample reveals the same chemical shift as it was discussed in Fig. 3.21. The carboxylic carbon (1) and the carbon nitride carbon (2, 4) lose in intensity, while the carbon hydrate carbon (3) gains in intensity with increasing exposure time. The changes indicate a breaking of C–O and C–N bonds and the formation of carbon hydrates. XPS measurements of the nitrogen 1s core levels indicate that nitrogen does not leave the sample but changes its chemical environment (not shown). Similar experiments were performed by Zubavichus *et al.* [1, 98], supporting this interpretation.

In the following all solid state RIXS maps of proline were measured with an

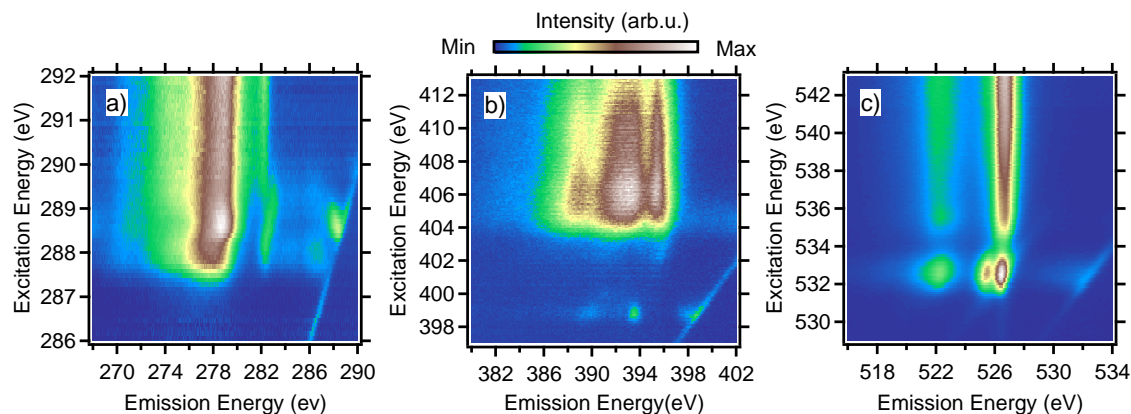


FIGURE 3.23. a) CK, b) NK, and c) OK RIXS maps of an evaporated proline layer. The X-ray emission intensity is plotted as a function of emission and excitation energy.

exposure time of 0.17 s.

The RIXS maps of proline at the C (a), N (b), O (c) K-edges are depicted in Fig. 3.23. The x-axis (abscissa) indicates the emission energy E_{Em} and the y-axis (ordinate) indicates the excitation energy E_{Exc} . The intensity of the X-ray emission is color coded. Blue represents zero intensity and white indicates high intensity. Each horizontal cut through the map represents a single resonant inelastic soft X-ray scattering (RIXS) spectrum excited with a photon energy according to the excitation axis. Vertical cuts through the map represent partial fluorescence yield X-ray absorption spectra (PFY-XAS). A structure visible in all three maps is a sharp line (bottom right corner of the maps). This line represents equal emission and excitation energies and is caused by elastic scattered photons (Rayleigh line).

An increase in the intensity of the “elastic line” for a particular excitation energy is an indicator for resonant excitation. In this case the photon energy (excitation energy) is equal to the energy difference between a 1s core state and an unoccupied state. In this resonant case the elastic transition has a very high probability and the intensity is increased. The effect is well described by the Kramer-Heisenberg formula [31]. Simultaneously to the increased elastic intensity, inelastic processes occur. Intensity close to the elastic line result from quasi-elastic transitions, for which the final state is again the electronic ground state but with an excited vibronic state. These vibrational losses (comparable to Stokes losses in Raman spectroscopy) can extend over several electron volts [77, 99]. As it can be observed in Fig. 3.23c, the vibrations can transform into an increased background signal several eV away from the elastic line extending into the regular inelastic transitions. This increased background is an indicator for an increased possibility to end in a continuum of final states, which is possible if

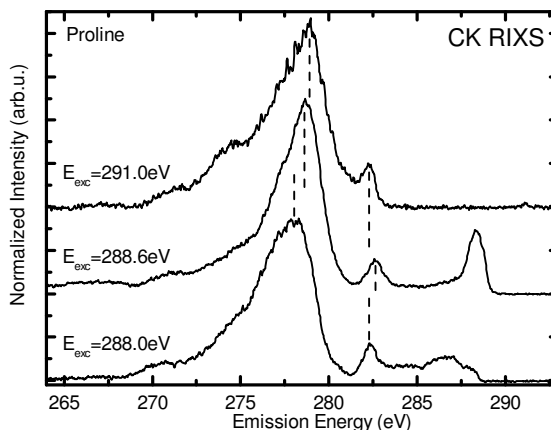


FIGURE 3.24. CK RIXS spectra of zwitterionic proline films excited at 288.0 eV, 288.6 eV, and 291.0 eV.

the molecule, or parts of the molecule, dissociate. A continuous amount of energy can then be transferred to the kinetic energy of the fragments. This indicates that the intermediate state (the state after the absorption but before the emission of the photon) is dissociative.

The observation of dynamical processes is only possible if these happen during the core hole lifetime. In the study of Weinhardt *et al.* [77], these features were identified as rapid proton movement on the timescale of the “core hole clock” (see chapter 2.1.3) of aqueous ammonia.

The bright intensity in the center of all three maps is the result of the inelastic scattering process in which the final state is a valence excited electronic state with a “hole” in the valence orbitals and an electron in the unoccupied orbitals. As already mentioned in chapter 2.1.3, this scattering process can be described in a two-step model with an absorption of a photon via the excitation of a core electron into an unoccupied orbital and the subsequent emission of a photon by the relaxation of a valence electron into the empty core level.

The CK RIXS map of solid proline is depicted in Fig. 3.23a. The RIXS map shows a strong excitation dependence in the region below an excitation energy of 290.0 eV. Above an excitation energy of 290 eV the emission pattern is constant and does no longer change as a function of excitation energy. The emission of X-rays starts at an excitation energy of 287.2 eV (in the following always referred to as absorption onset). The emission has a local maximum at $E_{\text{exc}} = 288.0\text{ eV}$ and becomes strongest for an excitation energy of 288.6 eV. At the same excitation energies strong vibrational structures appear at the elastic line, which indicates that a strong absorption resonance with vibronic coupling is located at these energies. At the first resonance ($E_{\text{exc}} = 288.0\text{ eV}$) the vibrational structure is even more intense than the Rayleigh line.

At $E_{\text{exc}} = 288.6 \text{ eV}$ the vibrational progression is also very strong but very close to the Rayleigh line. With increasing excitation energy, the progression shifts to lower emission energies and fades out (see Fig. 3.23a). The emission pattern at this excitation energy ($E_{\text{exc}}=288.6 \text{ eV}$) is quite different from the emission pattern below and above this resonance. Going from excitation energy of $E_{\text{exc}}=288.0 \text{ eV}$ to $E_{\text{exc}}=288.6 \text{ eV}$ the spectral weight is shifted from about $E_{\text{em}}=278.0 \text{ eV}$ to $E_{\text{em}}=278.7 \text{ eV}$. The small intensity at $E_{\text{em}}=282.3 \text{ eV}$ is also blue shifting to $E_{\text{em}}=282.6 \text{ eV}$. At higher excitation energies (above $E_{\text{exc}} = 290.0 \text{ eV}$) the small feature “jumps” back to $E_{\text{em}}=282.3 \text{ eV}$, while the overall maximum of the spectrum shifts further to $E_{\text{em}}=278.9 \text{ eV}$ (see Fig. 3.24). The absorption resonance ($E_{\text{exc}} = 288.0 \text{ eV}$) is in very good agreement to XAS studies of Zubavichus *et al.* [100], who attributed this resonance to a $\pi^*(\text{COO})$ transition [101].

The NK RIXS map of solid proline is displayed in Fig. 3.23b. The X-ray absorption onset at about 404.0 eV and the maximum at 405.7 eV are again in a very good agreement to the XAS studies from Zubavichus *et al.* [100]. The RIXS map also reveals a small unexpected absorption resonance at 398.8 eV . The emission signature of the resonance is very different from the “regular” NK emission pattern. The resonance might originate from contaminations. The signal is very weak and since proline is “transparent” at these excitation energies, a very small degree of contamination is sufficient to cause such a signal. Comparing the energy and shape of the contamination resonance with the spectral fingerprint of N_2 , N_2 can be excluded as the contamination [73]. The energy position and shape of the resonance, however, indicate that the resonance is a π^* resonance. One possible molecule with a similar XA resonance energy is NO [28].

Fig. 3.23c displays the OK RIXS map of solid proline. The map exhibits a clear and well separated absorption resonance at $E_{\text{exc}}=532.6 \text{ eV}$, which is again in perfect agreement to the work of Zubavichus *et al.* [100]. The emission fingerprint of the resonance is dramatically different from the emission at higher excitation energies. At the excitation energy of $E_{\text{exc}}=532.6 \text{ eV}$ three well separated emission features at emission energies of 522.3 eV , 525.4 eV , and 526.5 eV can be observed, while for excitation energies higher than $E_{\text{exc}}=535 \text{ eV}$ only two features at 522.3 eV and 526.7 eV occur.

3.2.2 The Influence of NaOH and HCl on the Spectrum of Water

One additional parameter relevant for investigating molecules and especially amino acids in their natural aqueous environment is the pH- value. By changing the pH-value, amino acids are modified by adding or removing protons at its functional groups and they can function as an acid (proton donor) or a base (proton acceptor). Other pH sensitive molecules, like for example phenolphthalein, change the color as a function of pH. Furthermore, in many other reactions the hydrogen protons (H^+) act as catalyst regulating the speed of the reaction.

By changing the pH-value of a solution, all possible charge states of an amino acid are accessible, whereas the amino acids are always present in a zwitterionic configuration in solid phase[102, 103], and in a neutral configuration in the gas phase [104].

The pH-value is defined as the negative decimal logarithm of the hydrogen proton activity, a_{H^+} [105]. Since the definition of the ion activity is quite complicated, the formula can be simplified and a_{H^+} is approximated by the concentration of the hydrogen ions (H^+). In reality these ions are not free, but they exist as hydronium ion (H_3O^+) and the formula can be written as:

$$(3.1) \quad \text{pH} = -\log_{10}(a_{H^+}) \approx -\log_{10}\left(\frac{c(H_3O^+)}{\text{mol/l}}\right)$$

In analogy to the pH-value also a pOH value can be defined. Both values are connected via the auto-ionization process of water ($2H_2O \rightleftharpoons H_3O^+ + OH^-$) with the equilibrium constant K_w , which is defined by the activity of the products. For highly diluted water solutions and at a temperature of about 22°C, the relation can be simplified to $\text{pH} + \text{pOH} = 14$. Thus the OH^- concentration can be expressed as:

$$(3.2) \quad \text{pOH} \approx 14 - \text{pH} \approx -\log_{10}\left(\frac{c(OH^-)}{\text{mol/l}}\right)$$

With equation 3.1 and 3.2, the concentrations of the H_3O^+ and OH^- ions can be calculated. The concentrations at pH 0 and pH 14 are then around 1 mol/l. For comparison, 1 l of water consists of about 55.4 mol H_2O . As a consequence, the spectral influence of the H_3O^+ and OH^- species on the X-ray spectra of water (XAS, XES, RIXS) can be considered as rather small (< 2%).

Although this “contamination” of the water spectrum with the spectral contribution of H_3O^+ and OH^- are rather small within the pH range of 0 and 14, upon resonant excitation the signature of the ions can be enhanced, which makes it visible in the spectrum.

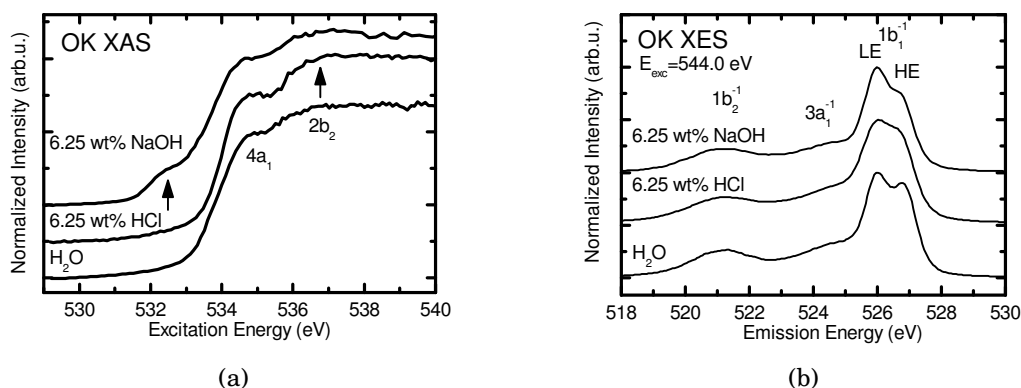


FIGURE 3.25. a) OK partial fluorescence yield X-ray absorption spectra (PFY-XAS) and OK X-ray emission ($E_{\text{Exc}} = 544\text{ eV}$) spectra (b) of water, water with 6.25 wt% HCl, and water with 6.25 wt% NaOH (taken from [73]).

The OK RIXS signature of NaOH was already mentioned by Oliver Fuchs [74] and discussed in detail in the work of Monika Blum [73]. Fig. 3.25a shows the partial fluorescence yield X-ray absorption spectra (PFY-XAS) of pure water (ultra pure water from Alfa Aesar), water solution with 6.25 wt% (weight percent) hydrochloric acid (HCl), and water solution with 6.25 wt% (weight percent) sodium hydroxide (NaOH).

The water spectrum shows two well-known absorption resonances [106]: The pre-edge at around 534.6 eV, which corresponds to transitions into the $4a_1$ orbital, and a main-edge at approx. 536 eV, which corresponds to transitions into the $2b_2$ orbital. Upon the addition of 6.25 wt% of HCl the overall spectral shape of the absorption edge does not change, but a small increase of the main-edge intensity in comparison to the pre-edge intensity is recognizable (see arrow in Fig. 3.25a). The changes upon the addition of 6.25 wt% of NaOH are more pronounced. The water absorption onset becomes less steep and a new pre-edge feature arises at about 532.5 eV. The rest of the XA spectrum is identical to the spectrum of pure water. Both changes are marked with an arrow.

Besides the OK XA spectrum also the OK XE spectrum shows changes caused by the presence of H_3O^+ and OH^- . The OK X-ray emission spectra of these three solutions is depicted in Fig. 3.25b. The water spectrum consists of four spectral features which can be assigned to three transitions arising from the three highest occupied molecular orbitals ($1b_2$, $3a_1$, $1b_1$). The interpretation and assignment of the spectral features are still discussed controversially in literature [79, 106–113] and discussed in more detail in chapter 4.1.

By the addition of 6.25 wt% of HCl or 6.25 wt% NaOH, changes mainly occur in the $1b_1^{-1}$ emission. By adding 6.25 wt% of HCl, the spectrum becomes essentially broader but apart from that the spectrum stays unchanged.

As for the XA spectrum, the addition of 6.25 wt% of NaOH has a much larger effect

on the water spectrum. The LE peak of the $1b_1^{-1}$ emission is slightly increased, which is in literature assigned to the increased number of OH^- ions in the solution [106].

The concentration of H_3O^+ and OH^- in a solution with 6.25 wt% amounts to 1.71 mol/l and 1.56 mol/l, respectively. The expected spectral contribution of H_3O^+ and OH^- at pH 0 and pH 14 (corresponding to 1 mol/l) should be smaller than the changes observed in Fig. 3.25. For the investigation of amino acids and other molecules in aqueous solution, the influences of H_3O^+ and OH^- on the OK RIXS spectra are present but small and well defined and can be separated from spectral signatures of the solved molecules.

Besides the effects of H_3O^+ and OH^- on the OK spectra, the OK emission of the amino acid is overlapping with the OK emission of water. The carboxylic group shows an XA resonance below the absorption onset of water [114]. In this energy regime the water is “transparent“ and the spectral fingerprint of the amino acid can be investigated without any influences caused by the water. In the following chapter the influence of pH on the spectra of proline is investigated.

3.2.3 The Influence of pH on the Electronic Structure of Proline

The chemical reactivity of an amino acid is determined by the ionic states of their functional groups, which are directly related to the pH-value of the solution. Each ionizable functional group (α -carboxylic group, α -amino group, and some side-chains) has a specific pK_a -value, indicating the ionizability. The pK_a -value corresponds to the pH-value for which the concentration of protonated and deprotonated conformation of a functional group is equal. For a pH smaller than the pK_s -value of one of the functional groups, the amino acid acts as an acid donating hydrogen protons. For a pH-value higher than the pK_a -value of a functional group, the amino acid acts as a base collecting hydrogen protons. Each amino acid has at least two pK_a -values, one for the α -carboxylic group and one for the α -amino group. The pK_a -values vary from amino acid to amino acid and depend strongly on the direct environment of the functional group.

Since the α -carboxylic group is a rather weak acid, the ratio between protonated and deprotonated species of a functional group can be calculated with the Hendersson-Hasselbach equation [115–117].

$$(3.3) \quad \text{pH} = \text{pK}_a + \log_{10} \left(\frac{c(A^-)}{c(HA)} \right)$$

Hereby, $c(A^-)$ denotes the concentration of the deprotonated anionic rest, and $c(AH)$ the concentration of the neutral (or protonated) functional group. If the pK_a -

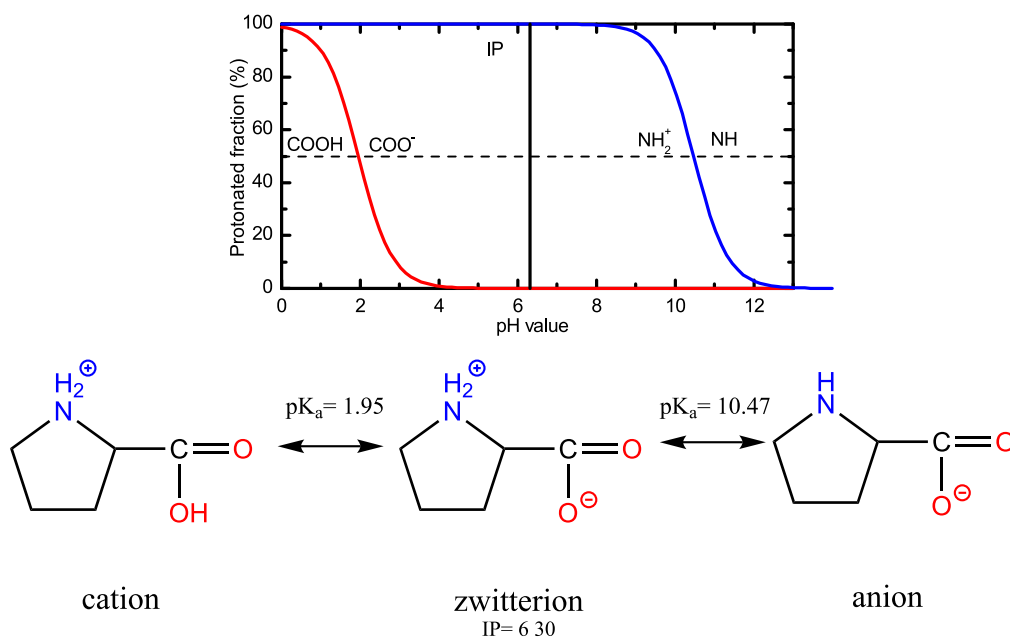


FIGURE 3.26. Top: Fraction of deprotonated to neutral species of the carboxylic group (red) and fraction of protonated to neutral species of the amino group (blue) as a function of pH. Bottom: All possible charge states of proline with pK_a-values and isoelectric point (IP) according to [88].

value of a certain functional group is known, equation 3.3 can be used to calculate the fraction of neutral (or protonated) functional groups:

$$(3.4) \quad \frac{c(HA)}{c(HA) + c(A^-)} = \frac{1}{1 + 10^{(pH - pK_a)}}$$

Fig. 3.26 a illustrates the ratio between the protonated and deprotonated configuration of the two functional groups of proline. The red graph indicates the fraction between COOH and COO⁻ and the blue graph indicates the fraction between NH₂⁺ and NH. The dotted line indicates the equilibrium concentrations at the two pK_a-values (1.95 and 10.47 [88]). The exponential behavior of the proton-transfer-reaction prevents the system to become fully anionic or cationic. A tiny fraction of molecules will always have the opposite configuration. In Fig. 3.26b the three pH-dependent Lewis structures of proline are depicted.

The following measurements on proline were done on three different sample solutions, each with a different pH and thus a different configuration of proline. For the sample solutions 3.4539 g of proline was solved in 20 ml of ultra pure water. This complies to a concentration of 3 mol/l and a pH of 6.8. To achieve the high and low pH solutions, NaOH and HCl were added, respectively. To set the pH-value to 13, 3.0 ml of NaOH (50 %) was added, resulting in a proline concentration of 2.6 mol/l. Since the

amino acid works as a buffer within the solution, for the low pH sample the initial concentration of proline was reduced to about 1 mol/l (2.3 g in 20 ml). The pH-value was then adjusted to pH 1 by adding 3.85 ml of HCl (50 %), resulting in a final proline concentration of about 0.8 mol/l.

At pH 6.8 99.98 % of the amino groups are protonated (NH_2^+) and 99.99 % of the carboxylic groups are deprotonated (COO^-). In other words, about 99.97 % of the proline molecules are in a *zwitterionic* state with no net charge. At pH 13.0 the carboxylic group is again deprotonated, while 99.99 % of the amino groups are neutral (NH) and the proline molecule is in an *anionic* configuration with net charge of -1. At pH 1 the situation is reversed. All amino groups are protonated and about 89.9 % of the carboxylic groups are neutral. At this pH proline is predominantly (89.9 %) in a *cationic* configuration with a net charge of +1.

The Carboxylic Group: OK-edge

For the carboxylic group of proline, the pK_a -value of 1.97 is below the average pK_a -value found for other amino acids. The pK_a -value of the carboxylic group is influenced by the neighboring amino group and thus varies within the group of amino acids. A smaller pK_a -value can be interpreted as a larger influence of the amino group on the carboxylic group [85].

Fig. 3.27 shows the OK RIXS maps of proline in aqueous solution at three different pH-values. The absorption edge of water starts at about 534 eV (excitation energy) and then dominates the map. For energies below the absorption onset, water is transparent and the emission can solely be related to the carboxylic group of proline. This is consistent with the observations in the OK RIXS map of solid proline (see Fig. 3.23c). As expected and calculated by Eqn. 3.4, the pre-edges of Fig. 3.27b (zwitterion) and Fig. 3.27c (anion) are identical, while Fig. 3.27a (cation) shows a different pre-edge pattern. The three emission features in Fig. 3.27b and Fig. 3.27c are typical of the deprotonated carboxylic group and are in accordance to the solid state measurement (see Fig. 3.23c), to previous OK RIXS experiments on glycine and cysteine [73, 86], and to RIXS experiments on acetic acid [114, 118, 119].

The maximum of the amino acid resonance of the zwitter ion (pH 6.8) is centered at $E_{\text{exc}} = 532.25$ eV. For the anion (pH 13) the maximum shifts to higher excitation energies and is centered at $E_{\text{exc}} = 532.5$ eV. This shift is most likely caused by an OH^- contribution which is centered at approx. $E_{\text{exc}} = 532.5$ eV. The emission fingerprint of both RIXS spectra (pH 6.8 and 13) consists of three features with descending intensity located at $E_{\text{em}} = 526.5$ eV, $E_{\text{em}} = 525.5$ eV, and $E_{\text{em}} = 522.3$ eV. The similarities in the two maps and the two pre-edge features are not surprising, since for both cases the carboxylic group is deprotonated (COO^-) and hence the local electronic structure

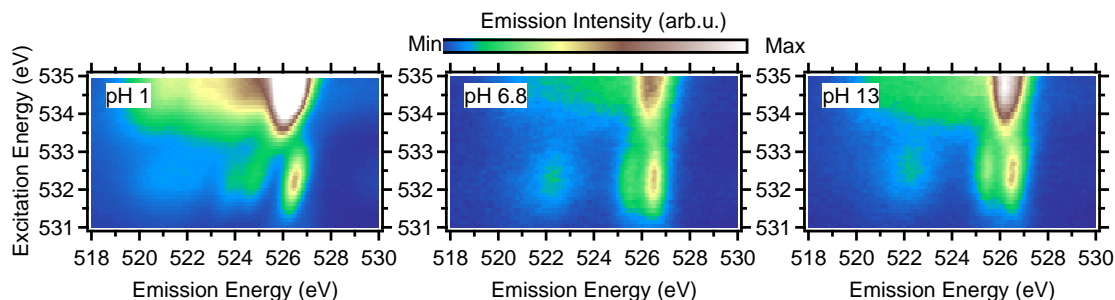


FIGURE 3.27. OK RIXS maps of proline in aqueous solution at three different pH-values (1, 6.8, 13.0) representing the cationic, zwitterionic, and anionic configuration. The absorption onset of water is visible at the top of the map.

surrounding the carboxylic group is expected to be similar.

As shown in the bottom of Fig. 3.26, the cation consists of a neutral carboxylic group and a protonated amino group. Consequently, the RIXS spectrum in Fig. 3.27a is different. The pre-edge resonance has its excitation maximum at $E_{\text{exc}} = 532.3$ eV. The emission fingerprint of this resonance is dominated by a strong peak at $E_{\text{em}} = 526.5$ eV and accompanied by three rather weak peaks centered at $E_{\text{em}} = 524.8$ eV, $E_{\text{em}} = 524.0$ eV, and approx. $E_{\text{em}} = 521.4$ eV, respectively (due to the low intensity, a center of the low energy feature is very hard to determine). The observed spectrum of a neutral carboxylic group is again in a very good agreement with previous measurements of cysteine [86] and also with measurements of acetic acid with a corresponding configuration of the carboxylic group [114, 118, 119].

For a closer inspection of the RIXS fingerprint of the different proline configurations, Fig. 3.28 illustrates the isolated OK RIXS spectra extracted from the maps in Fig. 3.27. To improve the signal to noise ratio, each spectrum was generated by averaging over three spectra in a 0.3 eV window centered at the respective absorption maximum ($E_{\text{exc}}^{\text{pH1}} = 532.3$ eV, $E_{\text{exc}}^{\text{pH6.8}} = 532.25$ eV, and $E_{\text{exc}}^{\text{pH13}} = 532.5$ eV). The generated spectra are compared to RIXS spectra of acetic acid (red). For better comparison the spectra of acetic acid were aligned with the proline spectra (shifted by +0.3 eV).

The RIXS spectra confirm the energy positions of all emission features as they were assigned above. Furthermore, two more details become visible. Firstly, the low-energy feature ($E_{\text{em}} = 520$ eV–523 eV) of the cationic proline (pH 1) shows a distinct asymmetry and fine structure, indicating that the observed intensity is the result of multiple transitions. Secondly, the OK RIXS spectra of zwitterionic (pH 6.8) and anionic (pH 13) proline are similar but not identical. The anionic configuration at pH 13 exhibits an increased intensity in feature (A), which was not visible in the RIXS maps. At this pH, the ratio of OH^- ions to proline molecules was estimated with Eqn. 3.2 and is

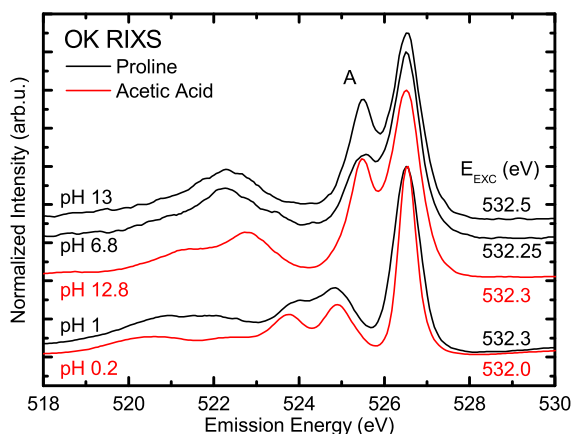


FIGURE 3.28. OK RIXS spectra of proline (black) in aqueous solution at various pH-values (1, 6.8, and 13) representing the cationic, zwitterionic, and anionic configurations compared to OK RIXS spectra of acetic acid (red) at pH 0.2 and pH 12.8. For better comparison the spectra of acetic acid were aligned with the proline spectra (shifted by +0.3 eV). The low pH-spectra represent a neutral carboxylic group, while the neutral and high pH-solutions represent a deprotonated carboxylic group.

about 1/40. Assuming that the RIXS cross section at this energy is similar for OH^- and the two oxygens of the carboxylic group, the spectral influence of OH^- on the RIXS spectrum of proline pH 13 should be about 1 to 2 % and hence negligible. Even by assuming a spectral contribution of 10 % and aligning the OH^- -RIXS spectrum with feature (A), the pH 13 spectrum could not be reconstructed satisfactorily from the pH 6.8 and the OH^- spectra (not shown).

The acetic acid spectrum (pH 12.8) shows a similar ratio of the two emission features as proline pH 13 spectrum. One can speculate that the increased intensity in feature (A) in Fig. 3.28 is the “natural” ratio between the two emission features and that for zwitterionic proline internal interactions between the protonated α -amino group and the carboxylic group broaden the emission of this transition.

Similar to the building block principle for non-resonantly excited NK XE spectra, the building block model can also be applied for the OK RIXS spectra of the three proline configurations (*cation*, *zwitterion*, *anion*). The OK RIXS spectra of acetic acid depicted in Fig. 3.28 show significant similarities. The usability of a building block model for RIXS was also shown in earlier studies on the example of cysteine [86], which was also compared to acetic acid as reference molecule (building block). In this context of the building block model the OK RIXS spectra of proline can also be compared to OK RIXS spectra of other amino acids. Previous studies on zwitterionic glycine [73, 120] and cysteine [86] show large similarities to zwitterionic proline.

The Amino Group: NK-edge

In this chapter the pH-dependence of the NK RIXS spectra of proline will be discussed. The solid state measurements already gave a hint about the spectral shape of the zwitterionic configuration. The result of the measurements in solution are depicted in Fig. 3.29. As expected, the spectra of the cation (c) and the zwitterion (d) are very similar. At both pH-values, the α -amino group is protonated. The pH 13 solution (e) shows the spectrum of the anionic proline, which hosts a neutral α -amino group. For comparison, NK XE spectra of cysteine at pH 5 (a) and pH 13 (b) are included in Fig. 3.29 [86].

The spectrum of zwitterionic cysteine Fig. 3.29 (a) shows the typical fingerprint of a protonated α -amino group (NH_3^+ see Fig. 3.9a). The NK XE spectrum of the anionic cysteine (pH 13) displayed in Fig. 3.29 (b) shows the fingerprint of a neutral α -amino group and is in very good agreement with glycine spectra recorded at similar charge states [65]. Furthermore, the spectrum shows large similarities to the deconvoluted NK XE spectrum of lysine (see Fig. 3.19f).

Even the library of the NK XE spectra of the 20 proteinogenic amino acids revealed the special character of the NK XE spectrum of zwitterionic proline (see Fig. 3.5). But in contrast to the solid phase which allows only the investigation of the zwitterionic configuration, pH dependent measurements additionally allow the measurement of the anionic configuration of proline which shows a neutral pyrrolidine ring.

The NK XE spectra of cationic and zwitterionic proline are, except for a small energy shift of about +0.3 eV, identical. Both spectra consist of three emission features centered at $E_{\text{Em}}^{\text{pH}0.8} = 388.8 \text{ eV}$, 393.0 eV , and 394.7 eV . No intensity changes between these two spectra are detectable. The energetic shift might be an indicator for the changes at the carboxylic group.

As expected, the NK XE spectrum of anionic proline (pH 13) has a completely different signature than the NK XE spectra of zwitterionic and cationic proline (pH 3.8 and pH 0.8). The neutral pyrrolidine ring structure shows a strong and sharp emission at 395.7 eV and two weaker and broader emission features at 391.8 eV and 387.5 eV , respectively. The latter feature is very broad and has a low energy tail which extends to 383.9 eV . In contrast to the NK XE spectra of zwitterionic proline and cysteine, the two NK spectra of anionic proline and cysteine show an almost identically high energy feature. Peak shape, relative intensity, and energy position of the dominating feature are almost identical for both spectra (3.29 (b), (e)). Only a small shift in the peak position of about $\Delta E = 0.3 \text{ eV}$ is present. Except from the similarities of the dominating feature, the spectra have no further similarities.

The fact that the NK XE spectra of proline have such a unique spectral shape is not surprising. The ring structure of the pyrrolidine ring alters the electronic

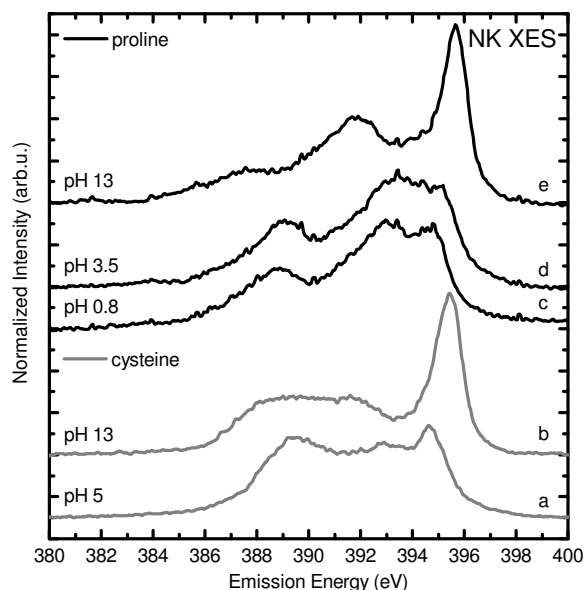


FIGURE 3.29. NK XE spectra ($E_{\text{exc}} = 419 \text{ eV}$) of proline in aqueous solution at various pH-values (0.8, 3.5, and 13) representing the cationic (c), zwitterionic (d), and anionic (e) configurations. As comparison the NK XE spectra ($E_{\text{exc}} = 420 \text{ eV}$) of cysteine in zwitterionic (a) and anionic (b) configuration is shown.

structure surrounding the nitrogen atom. It looks like as if the electronic structure of the nitrogen atom is altered to match the electronic configuration of the neighboring carbon atoms. In work about glycine, the dominating peak at about 395 eV is associated with the lone pair orbital of the nitrogen atom [120]. Which means by applying the building block model, in the cysteine spectrum (Fig. 3.29b) this feature can also be attributed to the lone pair orbital. Furthermore, also the dominating peak in the proline spectrum (Fig. 3.29e) can be assigned to the lone pair orbital which apparently has a larger influence on the local electronic structure surrounding the nitrogen atom than the delocalized ring structure.

As mentioned in the experimental chapter 2.3, the liquid flow through cell has many advantages compared to the liquid jet method, but the presence of a “hot” membrane, heated by the intense X-ray beam, can cause the adsorption of solved molecules onto the membrane.

Concentration Dependent Adsorption of Proline on SiC and Si₃N₄

Fig. 3.30 shows the measured NK RIXS maps for proline at three different pH-values representing the cationic, zwitterionic, an anionic configuration. It occurs that the NK RIXS map of the cationic proline at pH 0.8 (3.30a) meets the expectations and fits to the non-resonantly excited XE spectrum in Fig. 3.29c and the RIXS map of solid

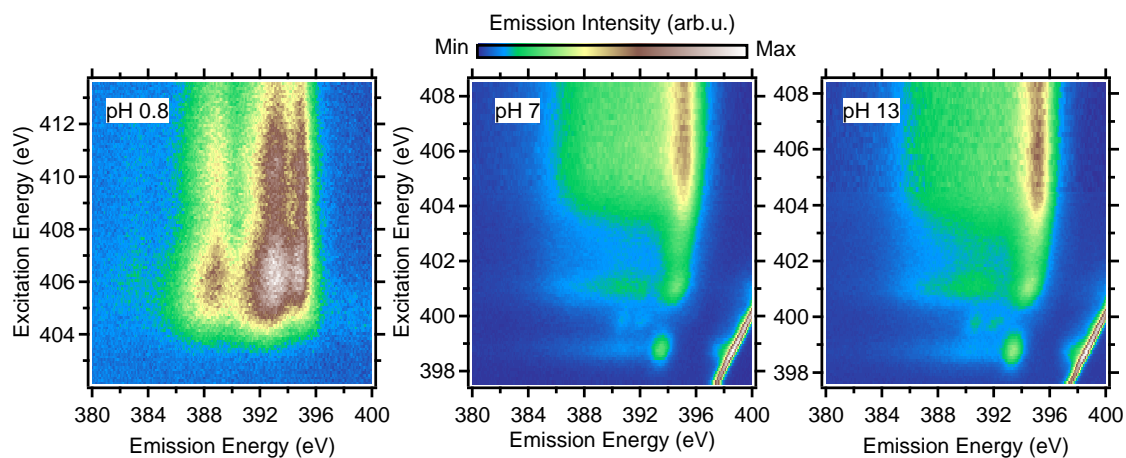


FIGURE 3.30. NK RIXS maps of proline in aqueous solution at various pH-values (0.8, 7, and 13) representing the cationic, zwitterionic, and anionic configurations.

proline. The other two NK RIXS maps of proline at pH 7 and pH 13 are identical, which is surprising. The pH 7 and pH 13 RIXS maps of proline also show a very rich pre-edge structure starting at $E_{\text{exc}} = 393.5 \text{ eV}$. By comparing the X-ray absorption pattern of the pH 13 RIXS map to an XA spectrum of gaseous proline measured by Plekan *et al.* [121], it becomes obvious that gaseous proline does not show this first absorption resonance at $E_{\text{exc}} = 393.5 \text{ eV}$. It is possible that the differences between the RIXS map and the literature could occur because of the different environment (liquid to gas phase) and the different configurations (anionic to neutral proline), but previous measurements have shown that XES and RIXS spectra are very local probing techniques and thus are mainly influenced by the electronic structure of the functional group itself (in this case the amino group). So far only minor changes in the XE and RIXS spectra have been found which could be related to the environment (hydrogen bonds). In both cases, anionic configuration in aqueous solution and neutral configuration in gas-phase, the charge state of the amino group is identical (NH).

In summary, the fact that the pH 7 and pH 13 RIXS maps are identical which should not be the case due to the different electronic configuration of the nitrogen atom, lead to the conclusion that the NK RIXS maps of proline at pH 7 and pH 13 in Fig. 3.30 do not show the molecule in the expected condition (zwitterionic, anionic configuration in aqueous environment, respectively). This assumption is supported by the fact that the X-ray emission pattern of the pH 13 and pH 7 spectra neither fit the non-resonantly excited XE spectrum of zwitterionic nor the spectrum of anionic proline (Fig. 3.29), as well as the fact that the absorption pattern of the pH 13 RIXS map does not fit to XAS measurements of gaseous proline [121].

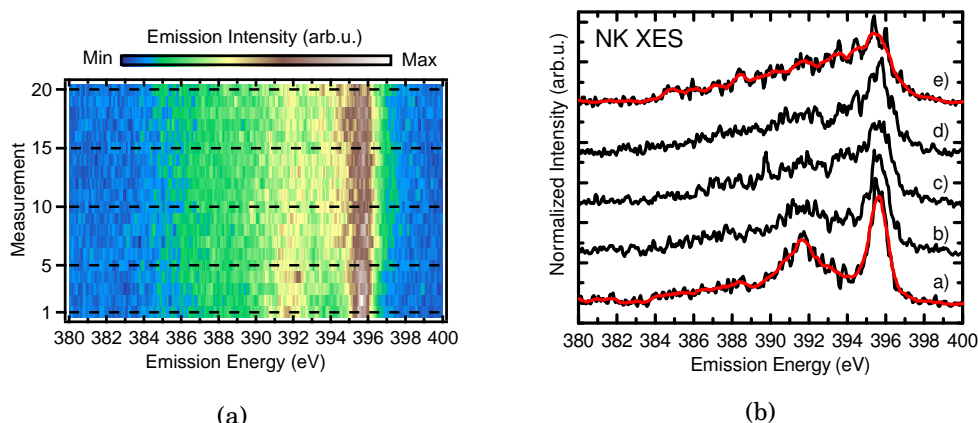


FIGURE 3.31. a) 20 10s NK XE spectra of anionic proline (pH 13) recorded successively ($E_{\text{exc}} = 419 \text{ eV}$). b) 1st, 5th, 10th, 15th, 20th spectrum of the measurement series in a) (black), smoothed spectrum depicted in red.

A possible reason for this might be that fragments of proline molecules, which are created by dissociation processes during the measurement adsorb on the membrane. The fragments might either be created by the heat of the intense synchrotron radiation and/or by auto-ionization due to the subsequent Auger decay, which leads to a highly charged and possibly highly unstable molecules. To rule out that damaged proline molecules within the solution and accumulate over time, the solution was pumped in an open cycle. This precaution did not change the outcome of the measurement.

The possible deposition of molecular fragments onto the membrane was investigated by a time-dependent measurement. The result is pictured in Fig. 3.31. Fig. 3.31a shows 20 NK XE spectra of anionic proline (pH 13). The spectra were recorded with an exposure time of 10 s. Including the readout and saving time, the second spectrum was started after approx. 13 seconds. To increase the signal to noise ratio, the measurement series was performed twice and the resulting spectra were summed. The result is shown in Fig. 3.31. Fig. 3.31b shows the 1st, 5th, 10th, 15th, 20th measurement of the series. To emphasize the changes in the spectra, the first and last spectra were smoothed (red).

Spectrum a) in Fig. 3.31b represents the first measurement with a pristine SiC membrane. Already after the third measurement, the spectrum changes (see spectrum b in Fig. 3.31b). The dominating feature at $E_{\text{em}} = 395.7 \text{ eV}$ loses in intensity as well as the intensity at $E_{\text{em}} = 391.8 \text{ eV}$. After 10 measurements (see spectrum c in Fig. 3.31b) both features are vanished completely and the spectrum has a triangular shape with its maximum at $E_{\text{em}} = 395.7 \text{ eV}$. The spectral shape stays constant for each subsequent measurement (spectrum d, e). The final triangular shape matches the emission of the pH 7 and pH 13 maps in 3.30 for excitation energies higher than $E_{\text{exc}} = 406.0 \text{ eV}$.

In summary, it can be stated that the NK RIXS spectrum of cationic proline (pH 0.8,

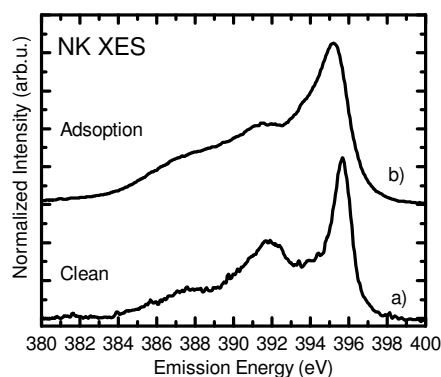


FIGURE 3.32. NK XE spectra of proline at pH 13 (anionic configuration) with a clean membrane and with Adsorbates ($E_{\text{exc}} = 419 \text{ eV}$).

see Fig. 3.29a) shows the amino group in the expected configuration, while the spectra of zwitterionic and anionic proline (pH 7, pH 13) observed in Fig. 3.30b and Fig. 3.30c show nitrogen containing fragments of proline on the SiC membrane. Since the area of “contamination” is limited to the spot size illuminated during the measurement series, the adsorption process is triggered by the X-ray beam.

Furthermore, it was found that extensive rinsing of the liquid cell with de-ionized water cleans the membrane. Nevertheless, in order to return back to the original clean SiC membrane, the exposure time of the membrane to the synchrotron radiation and the proline has to be rather short. To obtain the spectra plotted in Fig. 3.29, several measurement series like the one shown in Fig. 3.31 were performed. Of all series the first three to four spectra were added to increase the signal to noise ratio.

The RIXS maps displayed in Fig. 3.30 do not only show that an adsorption of proline fragments on the membrane occurs, but that the contamination does not occur at very low pH-values. Two possible explanations can be given. Firstly, the cationic configuration of proline is more stable than the zwitterionic and anionic configurations and thus less molecular fragments are created, which hinders an adsorption. Secondly, the low pH solution might clean the membrane by “etching” the molecular layer off the membrane. A third but rather unlikely explanation might be that the adsorption process is concentration dependent. By adding HCl to the neutral solution, the concentration of the proline is smaller than for the neutral pH solution. At high pH, however, NaOH was added to the base solution and so it reduces the concentration but has no effect on the adsorption behavior of proline.

3.2.4 The RIXS Spectra of Pyrrolidine

As it was introduced in chapter 3.1 and confirmed on solid state measurements in chapter 3.2.3, XES and RIXS spectra can be interpreted qualitatively by analyzing

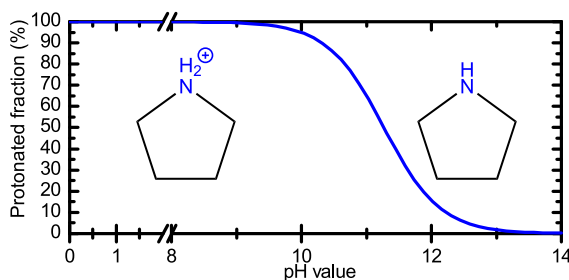


FIGURE 3.33. Protonated fraction of pyrrolidine as a function of pH-value. pK_a -value is 10.47 and identical to proline see Fig. 3.26.

XES and RIXS spectra of suitable reference molecules. The OK emission of proline is very similar to all of the other amino acids containing only the two oxygen atoms of the carboxylic group. In previous experiments it could already be shown that the OK RIXS spectra of the first absorption resonance of the amino acid cysteine could be very well approximated by using the OK RIXS spectrum of the first absorption resonance of acetic acid [86].

Fig. 3.29 in the previous section shows nicely that the NK XE spectrum of proline differs from the NK XE spectra of other amino acids. The comparison with cysteine shows this exemplarily. This implies that the reference molecule methylamine also fails in the description of the proline spectrum. A new reference molecule has to be investigated. The reference molecule of choice is pyrrolidine, which describes the entire ring structure of the proline molecule. Therefore, it is expected that the NK XES and RIXS spectra are in a very good agreement with the spectra of proline. Furthermore, due to the reduced size of the molecule, it was assumed that the dissociation discussed in the previous section might be different or even not existing which would give the possibility to record spectra of the medium and high pH conformations which are free of contributions of molecular fragments adsorbed on the membrane.

Fig. 3.34 shows the XA and XE spectra of pyrrolidine in aqueous solution at two different pH-values. As it can be seen from Fig. 3.33, the high pH solution (black) contains pyrrolidine in its neutral configuration, while in the low pH solution (red) the nitrogen atom of the pyrrolidine is protonated. The NK XE and XA spectra indicate the strong impact of the protonation on the electronic structure of the proline molecule. On a first glance, the spectra are also in a good agreement with the proline spectra.

The XE spectrum of the neutral pyrrolidine (Fig. 3.34, black) consists of four emission features centered at $E_{em} = 395.5$ eV, 391.8 eV, 397.8 eV, and 385.1 eV. The intensity of the features is decreasing with decreasing emission energy, while the width of the features increases with decreasing emission energy. The absorption spectrum of pyrrolidine (pH 13.6) shows an isolated absorption resonance at $E_{exc} = 398.9$ eV and a prominent pre-edge resonance at $E_{exc} = 401.9$ eV. The main-edge resonance is located

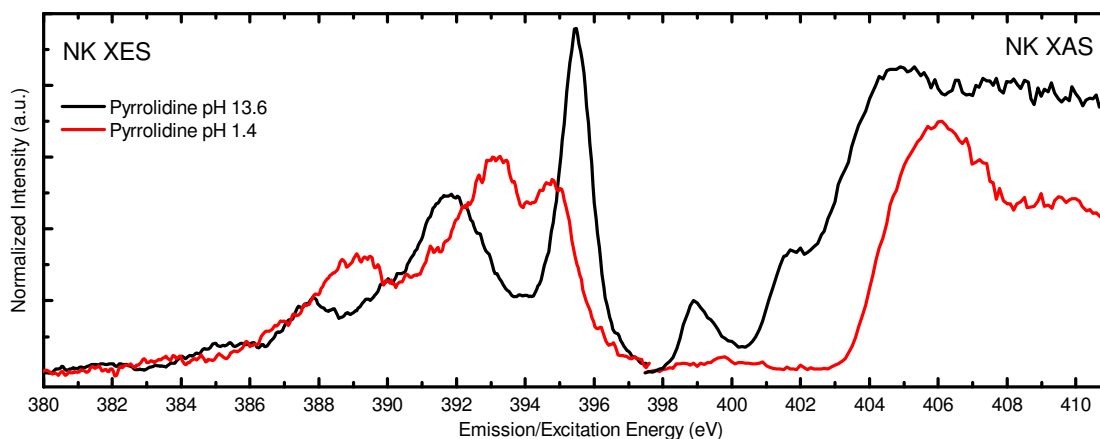


FIGURE 3.34. NK XES ($E_{\text{Exc}} = 424 \text{ eV}$) and XAS measurements of pyrrolidine in aqueous solution at pH 1.4 and pH 13.6 representing the cationic and neutral configuration, respectively.

at $E_{\text{exc}}=404.8 \text{ eV}$.

The spectrum of protonated pyrrolidine (pH 1.4, Fig. 3.34, red) is completely changed. Three overlapping peaks can be identified in the emission spectrum. The highest emission feature is located at $E_{\text{em}}=394.8 \text{ eV}$, followed by two emission features at $E_{\text{em}}=393.2 \text{ eV}$, and $E_{\text{em}}=389.1 \text{ eV}$. Compared to the XE spectrum of neutral pyrrolidine (pH 13.6), the features are broader and closer together. Upon protonation the changes in the electronic structure are even larger for the unoccupied states. Both, the isolated resonance structure and the pre-edge resonance, are vanished. The main edge is blue shifted to $E_{\text{exc}}=406 \text{ eV}$ and a post-edge at around $E_{\text{exc}}=409.8 \text{ eV}$ appears.

Fig. 3.35 shows the NK RIXS maps of protonated (pH 1.4) and neutral (pH 13.6) pyrrolidine in aqueous solution. The RIXS maps again demonstrate the large similarities between the electronic structure of proline and pyrrolidine in the direct vicinity of the nitrogen atom. The similarities become even clearer in Fig. 3.36a, which shows the non-resonantly excited NK XE spectra of proline (black) and pyrrolidine (red) at various pH-values. The spectra a), b) and a') show both molecules—proline in black and pyrrolidine in red—with a protonated nitrogen atom. The similarities between the spectra are remarkable. Spectrum c) and c') illustrate both molecules with a neutral nitrogen atom. The similarities are again strong but also small differences become visible, e.g., the spectrum of pyrrolidine c') shows a bit more fine structure. This might indicate that the proline spectrum c) is not completely free from beamdamage effects.

Fig. 3.36b shows the NK absorption spectra of proline (black) and pyrrolidine (red) at the different charge states of the nitrogen atom, generated from the RIXS maps depicted in Fig. 3.30 and Fig. 3.35. The spectra of the protonated nitrogen

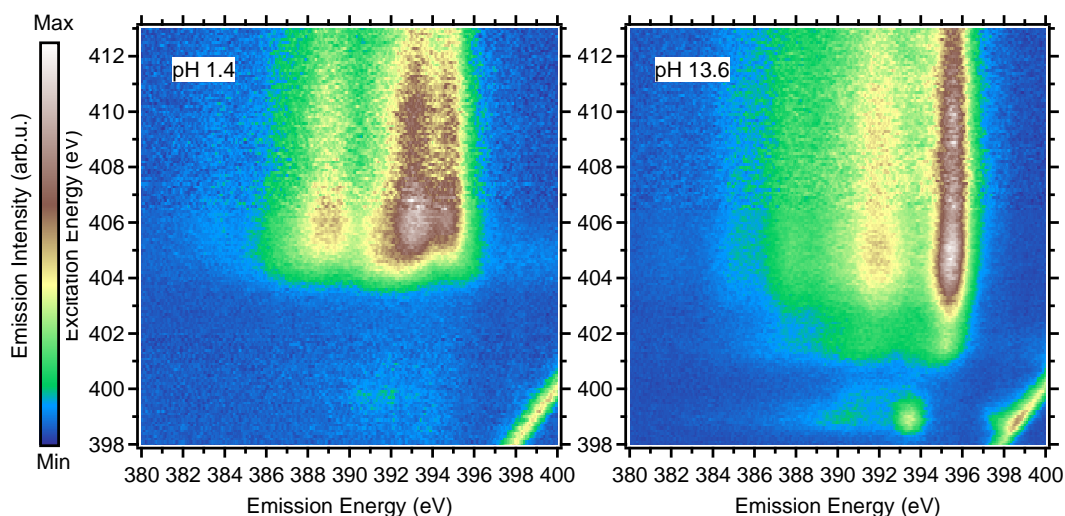


FIGURE 3.35. NK RIXS maps of pyrrolidine in aqueous solution at pH 1.4 and pH 13.6 representing the cationic and neutral configuration. The X-ray emission intensity is color coded.

atoms of proline and pyrrolidine a), and a') are again in remarkably good agreement. The XA spectrum of the neutral proline solution b) is expected to show the same behavior as the XA spectrum of the low pH solutions a), a'). However, spectrum b) in Fig. 3.36b shows a different result. The comparison of spectra a), a'), and b) implies that the two pre-edge resonances have their origin in the adsorption of molecular fragments onto the window. The spectra c) and c') of the high pH solutions reveal small differences. Although both molecules show an almost identical pre-pre-edge resonance at about $E_{\text{exc}}=398.9$ eV, the pre-edge resonance has slightly different energy positions. For proline the resonance is slightly red-shifted compared to the pre-edge resonance of pyrrolidine and matches with the pre-edge of Fig. 3.36b. The main-edges again have matching energy positions, but the pyrrolidine main-edge is more pronounced than the proline main-edge. It can be concluded that the first absorption resonance ($E_{\text{exc}}=398.9$ eV) originates from the molecular fragments adsorbed to the membrane. Furthermore, the second absorption resonance has a different origin for the different molecules. For proline the resonance is also caused by the adsorption of molecular fragments, while for pyrrolidine, since its energetic position is different, the resonance seems to be real.

The assignments are supported by electron energy loss experiments on gaseous pyrrolidine done by D.C. Newbury *et al.* [122] and by X-ray absorption measurement of gaseous proline performed by Plekan *et al.* [121]. In the high pH solutions the nitrogen atom is in neutral configuration and can be compared to the NK measurements of the

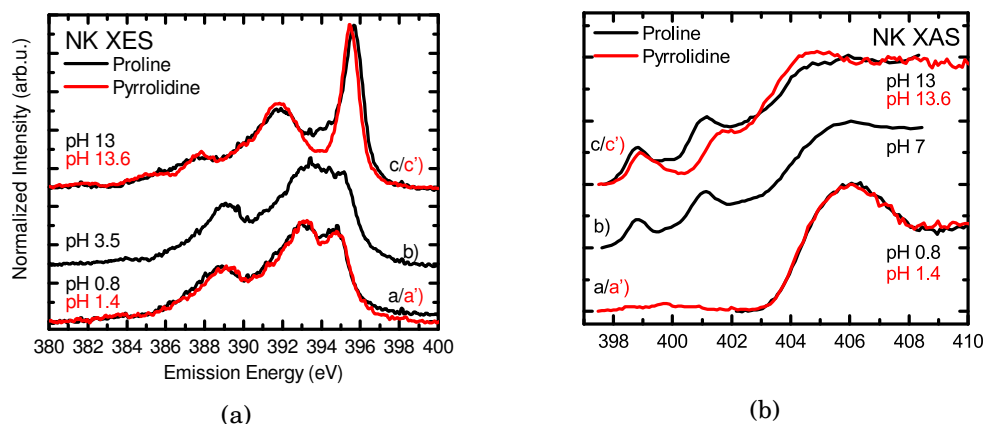


FIGURE 3.36. a) NK XE spectra of proline (black) excited at $E_{\text{exc}} = 419 \text{ eV}$ and pyrrolidine (red) excited at $E_{\text{exc}} = 424 \text{ eV}$ in aqueous solution at various pH-values. b) NK XA spectra of the same aqueous solutions.

gaseous molecules for which the nitrogen atom is also neutral. In both manuscripts the pre-pre-edge features at $E_{\text{exc}}=398.9 \text{ eV}$ were not observed. Newbury *et al.* observes the first absorption resonance at $E_{\text{exc}}=401.0 \text{ eV}$, a second resonance at $E_{\text{exc}}=402.5 \text{ eV}$ (not visible in this experiment), and the main-edge feature at $E_{\text{exc}}=404.5 \text{ eV}$. Although the absolute energy scale is different, the relative energies are close to the values found in this experiment. This is also in agreement with the NK XA spectrum of proline of Plekan *et al.*, which shows a first resonance at $E_{\text{exc}}=401.1 \text{ eV}$, a second at $E_{\text{exc}}=402.5 \text{ eV}$ (not observed in this study), and a third resonance at $E_{\text{exc}}=404.4 \text{ eV}$.

Although the measured X-ray absorption spectra illustrated in Fig. 3.36b are superimposed by the spectral contribution of an adsorbed layer of molecular fragments, the manuscripts mentioned above ([121, 122]) can be used as a reference. To gain additional information about the spectra and the orbital structure of proline and pyrrolidine, XES and XAS calculations of isolated proline and pyrrolidine were performed using the StoBe-deMon code.

3.2.5 Comparison Between Theory and Experiment

As it was shown at the beginning of this chapter, the comparison between experimental and theoretical spectra can provide additional information, which is not accessible by the experiment alone. It was shown that the approximated description of the XE and XA spectra of molecules in crystalline structure with calculations of isolated molecules works quite well and allows to estimate the influence of the environment on the measured spectrum. The same approach now will be used for the aqueous solution. The calculations presented in this chapter were calculated using the StoBe-deMon package. The details of the calculation are can be found in section 2.2.2.

In the following, calculated emission and absorption transition energies and oscillator strength of isolated pyrrolidine are depicted in Fig. 3.37 and Fig. 3.38. Hereby Fig. 3.37a illustrates the protonated pyrrolidine molecule and Fig. 3.37b the neutral pyrrolidine molecule. Even on this rather simple level of theory, the agreement between theory and experiment is very good for both configurations. The calculated transition energies and intensities were broadened by Gaussians to simulate vibrational, life time, and experimental broadening effects. The width of the Gaussians were chosen to achieve the highest possible agreement with the experiment. The FWHM increases with decreasing emission energy (for a justification of this see below). The area of the Gaussian is determined by the oscillator strength.

The width of spectral features is mainly determined by two parameters. Firstly, the excitation of molecular vibrations during the transition. Secondly, the lifetime broadening of the single states. The first broadening “term” is expected to vary from transition to transition depending on the vibrational coupling strength of the orbitals

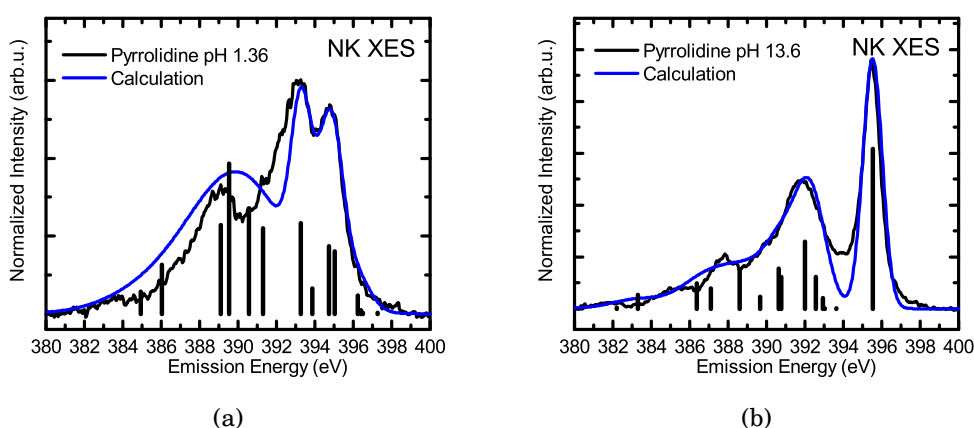


FIGURE 3.37. a) NK XE spectrum ($E_{\text{Exc}} = 424 \text{ eV}$) of pyrrolidine pH 1.4 (black). Calculated X-ray emission transitions of an isolated protonated pyrrolidine molecule (black bars). Gaussian broadened calculation (blue). b) NK XE spectrum ($E_{\text{Exc}} = 424 \text{ eV}$) of pyrrolidine pH 13.6 (black) and theoretical spectrum of isolated neutral pyrrolidine (blue).

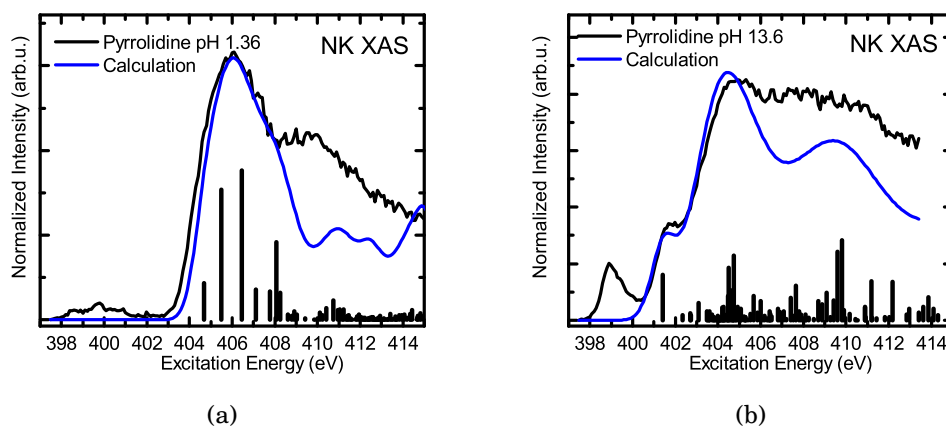


FIGURE 3.38. a) NK XA spectrum of pyrrolidine pH 1.4 (black). Calculated X-ray emission transitions of an isolated protonated pyrrolidine molecule (black bars). Gaussian broadened calculation (blue). b) NK XA spectrum of pyrrolidine pH 13.6 (black) and theoretical spectrum of isolated neutral pyrrolidine (blue).

involved. The lifetime is mainly influenced by the possibility of fast auger decay which is more likely to happen for deeper bound orbitals with a lower transition energy. This lifetime dependency increases the FWHM of transitions with a lower energy in respect to transitions with higher XE energy.

The calculated spectrum of protonated pyrrolidine (Fig. 3.37a) is in good agreement with the experiment. Both, the two high energy features and the broad low energy feature are visible. The intensity ratio between the two high energy features is in good agreement to experiment. However, to not overestimate the intensity of the low energy feature a very large width was chosen. These differences might be an indicator for the influence of the aqueous environment. Furthermore, the calculation shows that the highest occupied molecular orbitals (HOMOs) hardly have any transition probability due to the lack of spacial overlap with the N 1s core orbital.

The calculated spectrum in Fig. 3.37b is also not able to describe all details of the experimental spectrum. At about $E_{em}=394.0$ eV the calculation shows no intensity, while the experiment still exhibits intensity. The discrepancy might be caused by an underestimated transition probability of the HOMO-1 orbital, or can also be an indicator for possible hydrogen bonds being attached to the nitrogen atom. Besides the differences, due to the calculation the dominating feature can be assigned to the HOMO orbital, which is dominated by the atomic lone pair orbital of the nitrogen atom. The latter can be seen as a characteristic difference between the two configurations. In protonated pyrrolidine, the deeper bound orbitals have a larger overlap with the nitrogen atom while for the neutral pyrrolidine the overlap with the nitrogen atom decreases for increasing orbital binding energy.

Fig. 3.38a and Fig. 3.38b show the XA spectra of the two conformations. The protonated pyrrolidine is depicted in Fig. 3.38a and shows, apart from a small shift (≈ 0.35 eV) very good agreement with the experiment. The neutral pyrrolidine is illustrated in Fig. 3.38b. The calculation describes the pre-edge and the main-edge resonances nicely which is in accordance to the data of Newbury *et al.* [122]. This supports the conclusion that in case of pyrrolidine the pre-edge ($E_{\text{exc}}=401.0$ eV) is part of the intact molecule, while in case of proline this feature is also caused by the adsorption of molecular fragments. The pre-pre-edge resonance is not present in the calculation, which is another indication that this resonance results from molecular fragments adsorbed to the membrane.

3.2.6 Summary

In this chapter the building block approach was used to enable an in-depth analysis of the XA, XE, and RIXS spectra of solid and aqueous proline. Hereby pyrrolidine was used as a reference molecule to proline. The CK RIXS map of solid proline is very sensitive to the excitation energy showing numerous resonances, which reveal a localization of the molecular orbitals to different functional groups of the molecule. Since in solid state, only the zwitterionic configuration of proline is accessible, aqueous solutions of proline at various pH-values were investigated in the second part of the chapter. Both functional groups are strongly influenced by the protonation and deprotonation occurring upon variation of the pH-value. At neutral pH, a strong contamination of the membrane by molecular fragments could be observed which caused a strong signal in the X-ray spectra overlaying the proline signal.

Pyrrolidine was used as reference molecule to describe the NK emission and RIXS spectra of proline. The contamination was not as present in the pyrrolidine solutions as it was the case for proline. Due to the pyrrolidine spectra, the intact spectrum of proline could be identified and described. It could be shown that the origin of the unique NK emission spectrum of proline is mainly caused by the influence of the ring structure, which makes it impossible to compare it to the NK XE spectra of other amino acids hosting an α -amino group. The description of the NK XE spectrum of proline using the smaller reference molecule pyrrolidine, which can be easily calculated using the StoBe-deMon DFT code, allowed the assignment of single emission features within the spectrum to isolated molecular orbitals.

3.3 RIXS Study of Histidine and Imidazole

In the previous chapter the electronic structure of proline was discussed. Apart from proline, which is special due to its pyrrolidine ring, histidine is the next more complicated amino acid featuring a heterocyclic ring structure, called imidazole.

3.3.1 The Influence of pH on the Electronic Structure of Histidine

The biological relevance of histidine is significant. Although histidine is not found very often in regular proteins, it plays a crucial part in metalloproteins. The most famous enzyme among this class might be hemoglobin, in which histidine is found directly at the active center linking the protein to the iron ion [123]. Hemoglobin is an oxygen-transporter in red blood cells. The oxygen molecule is incorporated in the active center of the protein between the iron core and a histidine ligand. The bonding affinity is mediated by its ionic side-chain (the imidazole ring). The imidazole molecule itself is an essential component of the upcoming material class of ionic liquids. Since 1984, when imidazole was incorporated in an ionic liquid for the first time, it has become a fundamental component in this field [124].

Ionic liquids themselves were firstly reported by Paul Walden in 1914 [125]. Since the first discovery, a large variety of ionic liquids have been reported. Over 1 million different solvents based on ionic liquids were tailored and the community is convinced that ionic liquids will be used in all industrial fields [126]. One example of an (probably the most famous) industrial application for an ionic liquid is the BASIL™ process invented by BASF [127].

Fig. 3.39 shows the non-resonantly excited CK, NK, and OK X-ray emission spectra of solid histidine. As for all the other amino acids in the solid phase, the amino acid is present in only one configuration. Although the zwitterionic configuration in solid state is similar to the zwitterionic configuration in liquid phase, the solid phase does not represent the natural environment of the amino acid. While in solid phase the zwitterionic configuration is stabilized by a rigid crystalline structure, the aqueous zwitterionic configuration is stabilized by a flexible and supposedly constantly changing hydration shell. Fig. 3.40 shows the concentration of the protonated functional groups as a function of pH-value. Since the side-chain of histidine can be protonated as well, the diagram shows three functions and in total four different configurations are possible. For the calculation of the protonated fraction the Henderson-Hasselbach equation 3.3 was used. The pK_a -values were taken from [88]. The blue curve indicates the protonation of the α -amino group which has its equilibrium point at a pH 9. For pH-

values higher than pH 9, the majority of the molecules are in an anionic configuration. At a pH-value of pH 8, almost all α -amino groups are protonated and the histidine is in the zwitterionic configuration. The green curve with its equilibrium point at pH 6 displays the protonation behavior of the imidazole side-chain. The protonated fraction of the carboxylic group is indicated by the red curve which is centered at pH 1.7. At pH 4, both amino groups (α , and imidazole) are protonated while the carboxylic group is still deprotonated resulting in a single charged cationic configuration. For pH-values lower than 1.7 the majority of the molecules is present in a dicationic configuration for which the carboxylic group is neutral and the amino groups are protonated.

In order to record XE spectra of histidine without a spectral signature of molecular fragments adsorbed at the membrane, the membrane was continuously scanned during the measurement. To increase the signal to noise ratio, several spectra were recorded and summed up.

In Fig. 3.41a the OK RIXS spectra of histidine at four different pH-values are displayed. The spectra were recorded at the absorption resonance of the carboxylic group. This leads to an excitation energy of $E_{\text{exc}} = 532.2\text{eV}$ for the pH 0.1 solution and $E_{\text{exc}} = 532.5\text{eV}$ for the pH 2.8, 7.9, and 13 solutions. The pH-values were chosen to probe the four different conformations of the histidine molecule. The largest changes in the OK RIXS spectra are expected to occur between pH 0.1 and pH 2.8. At pH 0.1, the carboxylic group is in neutral configuration and at pH 2.8, 93 % of the carboxylic groups are deprotonated: the carboxylic group does not change for higher pH-values.

The results are two groups of emission spectra, one spectral fingerprint at pH 0.1, which represents a neutral carboxylic group and one at high pH (2.8, 7.9, 13), which represents a deprotonated carboxylic group. Fig. 3.41b illustrates the non-resonantly excited NK XE spectra of the same pH solutions. Here the largest changes are expected

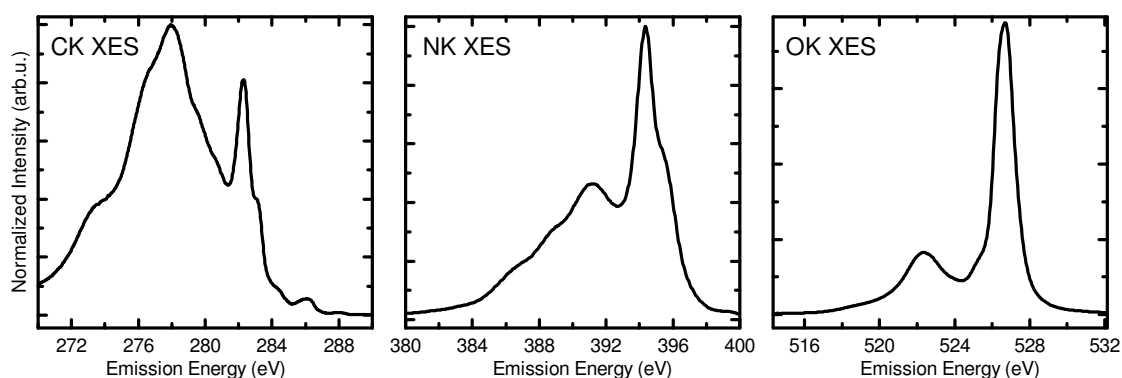


FIGURE 3.39. XE spectra of histidine powder measured at the carbon ($E_{\text{exc}} = 322\text{eV}$), nitrogen ($E_{\text{exc}} = 424\text{eV}$) and oxygen ($E_{\text{exc}} = 557\text{eV}$) K-edge.

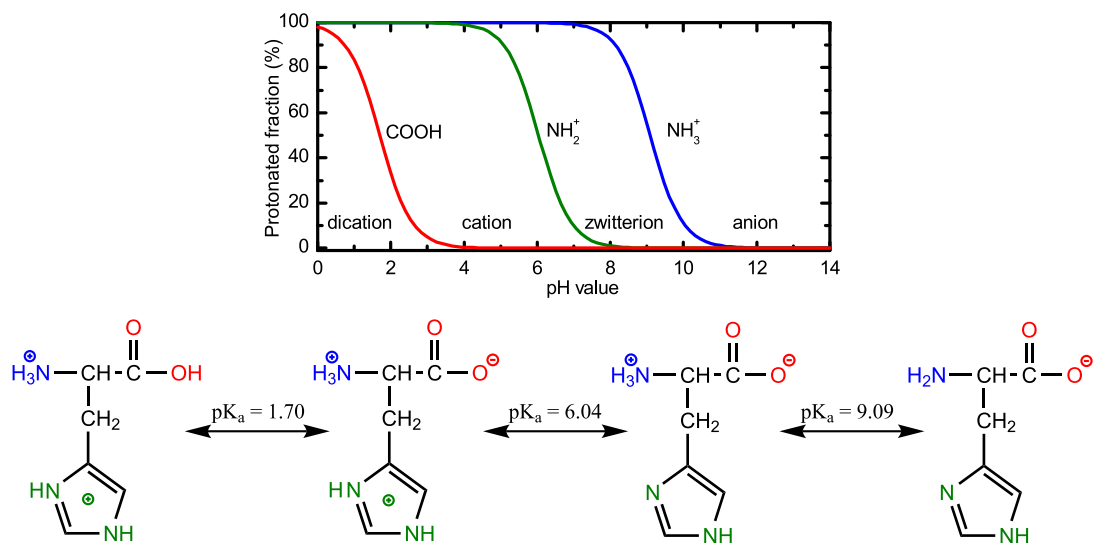


FIGURE 3.40. Fraction of the protonated functional group as a function of pH-value. The carboxylic group is shown in red, the imidazole ring in green, and the α -amino group in blue.

to occur between pH 13 and pH 2.8, while the spectra of pH 2.8 and pH 0.1 are expected to be very similar.

As a comparison, Fig. 3.41a shows the OK RIXS spectra of acetic acid (red). The spectra were also recorded at an excitation energy corresponding to the first absorption resonance. The acetic acid was measured at two pH-values representing the neutral (pH 0.2) and the deprotonated (pH 12.8) configuration. The similarities to the corresponding OK spectra of histidine are present but not as large as for other amino acids like proline (see Fig. 3.28) or cysteine [86]. Both solutions at low pH (pH 0.1 histidine, pH 0.2 acetic acid) show the same sharp and dominant high energy peak at about $E_{em}=526.3$ eV which can, in case of acetic acid, be attributed to the HOMO orbital that has a strong p-type character dominated by the two oxygen atoms [86, 118, 119]. The remaining parts of the spectra show a qualitative agreement but the spectrum of histidine exhibits additional intensity around $E_{em}=522.0$ eV, which covers the fine structure visible in the acetic acid spectrum. As the investigation of methanol has demonstrated, this energy region is usually attributed to molecular orbitals which are largely influenced by the carbon atoms [73, 90]. This is in agreement with the higher number of carbon atoms in the histidine molecule and the resulting increased number of orbitals in this energy regime.

The same effect can be found for the deprotonated spectra. The high energy features centered at $E_{em}=526.5$ eV and $E_{em}=525.5$ eV are represented in all four spectra (pH 2.8, 7.9, 12.8, and 13.0). Nevertheless, small differences in the intensity ratio between the two peaks are visible. With increasing pH-value, the feature at $E_{em}=525.5$ eV

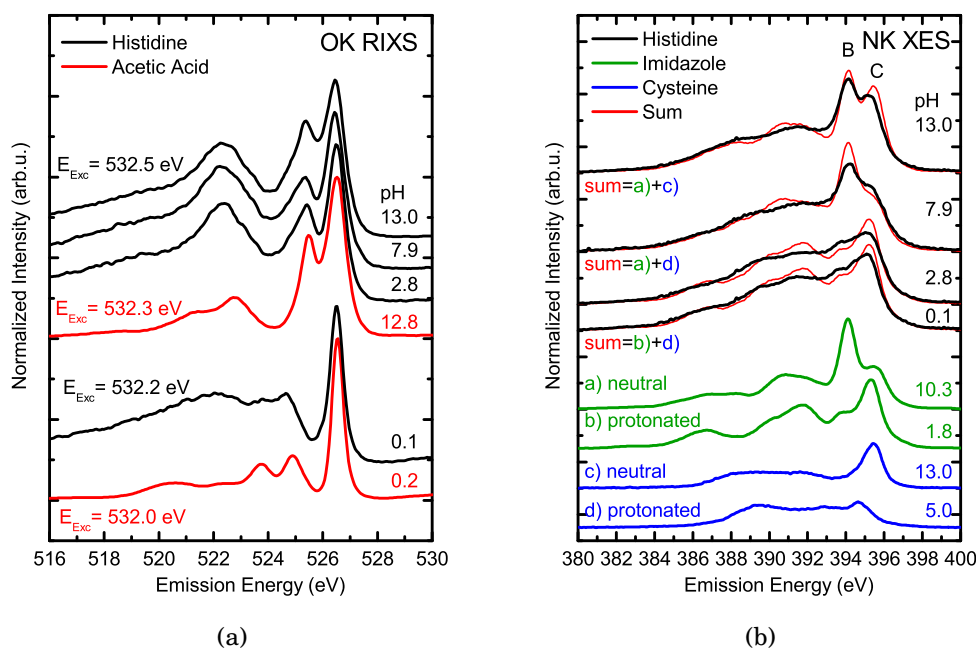


FIGURE 3.41. a) OK RIXS spectra of histidine (black) in aqueous solution at various pH-values (0.1, 2.8, 7.9, and 13.0) are compared to OK RIXS spectra of acetic acid (red) in aqueous solution at various pH-values (0.2 and 12.8). For better comparison the spectra of acetic acid were aligned with the histidine spectra (shifted by +0.3 eV). b) NK XE spectra of different histidine (black) configurations reproduced by a sum (red) of spectra of imidazole (green) and cysteine (blue) at various pH-values. $E_{exc}^{His} = 424\text{ eV}$, $E_{exc}^{Im} = 424\text{ eV}$, and $E_{exc}^{Cys} = 420\text{ eV}$

increases in intensity relative to the one at $E_{em}=526.5\text{ eV}$. This was also observed in the spectra of proline (see Fig. 3.28) and cysteine [86]. As for proline, about the origin of this feature one can only speculate. One possibility might be that this feature indicates the influence of the protonated α -amino group present in the zwitterionic form which changes if the α -amino group gets deprotonated. Changes in the hydrogen bonding network caused by the deprotonation might also create this signal. The low energy part of the spectra is significantly different for histidine and for acetic acid. While for acetic acid the low energy part consists of two intensity maxima centered at $E_{em}=522.8\text{ eV}$ and $E_{em}=521.4\text{ eV}$, the histidine spectra have a peak at $E_{em}=522.3\text{ eV}$ located on top of a broad feature similarly shaped as in the pH 0.1 spectrum.

Again the increased intensity in this regime can be explained by a higher number of carbon atoms and the resulting increased number of orbitals in this energy region. As mentioned above, in order to achieve spectra which are free or nearly free from spectral signatures of molecular fragments adsorbed to the membrane, the spectra were recorded while the membrane was scanned in the beam. With this procedure the

histidine was always measured with a clean membrane and it can be assumed that the shown spectra are free from the mentioned contamination effects.

Fig. 3.41b illustrates the NK emission spectra of histidine (black). The spectra were modeled by the summation of NK XE spectra of suitable reference molecules (red). The histidine molecule consists of three nitrogen atoms, two are located in the heterocyclic side-chains, plus the regular α -amino nitrogen. For each species, a reference spectrum was chosen. The side-chain is modeled by an imidazole molecule (green). The two imidazole spectra were recorded at two different pH-values to account for the two configurations (pH 1.8 protonated, pH 10.3 neutral). To model the α -amino group, the NK XE spectra of aqueous cysteine at two different pH-values were used [86] (pH 5.0 protonated, pH 13.0 neutral).

As a first approximation, the two reference spectra were area normalized and weighted with respect to the number of nitrogen atoms. This approximation of the ratio implies that the X-ray emission crosssection is equal for all chemically in-equivalent nitrogen atoms, which is a good assumption in a first approximation. The red spectrum is the resulting sum of the two reference spectra, imidazole (green) and cysteine (blue). The two spectra were summed up depending on the configuration of the histidine at the specific pH-value. For example for the pH 13.0 spectrum of histidine (top, black), for which histidine is in an anionic configuration with a neutral side-chain and a neutral α -amino group, the spectrum of neutral imidazole a) and the spectrum of neutral cysteine c) were summed up (red). The zwitterionic configuration of histidine is modeled by the spectrum of neutral imidazole a) and the spectrum of protonated cysteine d). For the cationic and dicationic spectra both protonated spectra were summed up.

The comparison of the experimental histidine spectra and the constructed spectra shows a reasonable agreement and gives an insight into the character and the origin of the high energy emission features of histidine without using any theoretical calculations. For example in the pH 13 spectrum peak B is dominated by the imidazole ring, while the peak C is dominated by the α -amino group. At pH 7.9, the spectrum of the α -amino group changes from neutral to protonated and hence peak C shrinks to a shoulder and is entirely dominated by the imidazole spectrum. A second transformation occurs from pH 7.9 to pH 2.8. Peak B vanishes completely while peak C remains. By going from pH 7.9 to pH 2.8, the cysteine spectrum does not change further since the α -amino group stays unchanged. In contrast, the imidazole spectrum is modified. The ratio between peak B and C in spectrum a) and b) changes upon protonation. At even lower pH-values (pH 0.1) the charge state of the nitrogen atoms stays constant and hence the spectrum of histidine exhibits the same signature as at a pH-value of pH 2.8.

3.3.2 The RIXS Spectra of Imidazole

As it was shown above, histidine is a complex molecule and the contamination of the membrane shows an influence on the spectra after exposure times longer than approx. 20 seconds even with scanning the membrane. This issue prevents the measurement of RIXS maps of histidine which would require measurement times of approx. 30 minutes or more. By using the building block approach introduced in the previous chapter, imidazole can be used to investigate the hetero-cyclic molecule side-chain of histidine. As shown above, the NK XE spectra of histidine can indeed be approximated by the summation of a NK XE spectrum of cysteine and of NK XE spectra of imidazole.

In the following the electronic structure of the hetero-cyclic molecule will be investigated in more detail. The chemical reactivity of free imidazole is similar to its reactivity as a part of histidine. This is also reflected in the pK_a -value of the molecule which is very close to the pK_a -value of the side-chain in histidine. Investigating imidazole instead of histidine has a pronounced advantage. Imidazole is highly soluble in water and due to the reduced size more stable to intense X-ray radiation. The spectra of imidazole could be recorded without observing any adsorption of molecular fragments onto the window membrane.

Fig. 3.42 illustrates the fraction between protonated and neutral imidazole as a function of the pH-value. The pK_a -value of the imidazole molecule is at pH 7.0 [88]. For pH-values lower than pH 7.0, the protonated conformation is dominating. This conformation is also known as imidazolium (ImH^+). For pH-values higher than pH 7.0, the neutral conformation is dominating (imidazole, Im). Within the graph the two conformations are displayed and the non-equivalent carbon and nitrogen atoms are labeled.

To investigate the two conformations in aqueous solution, 8.51 g of imidazole (98% purity Alfa Aesar) was solved in 25 ml of ultra pure water (Alfa Aesar). This results in a concentration of about 5 M and a pH-value of 10.3. To lower the pH-value below pH 7, 20 ml of HCl was added to the 5 M solution. This reduces the concentration to 2.78 M and the pH-value to 1.8.

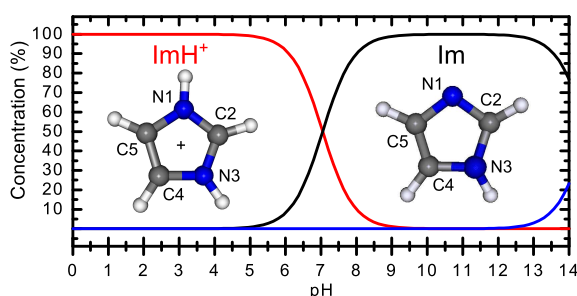


FIGURE 3.42. Imidazolium/imidazole ratio as a function of pH.

Imidazole	N1	C2	N3	C4	C5
XES	0	+0.75	+0.45	+0.55	+0.57
XAS	+0.75	+0.74	+0.75	+0.64	+0.64
Imidazolium					
XES	-0.7	-0.3	-0.7	-0.3	-0.3
XAS	-0.4	-0.2	-0.4	-0.6	-0.6

TABLE 3.2. Energetic shifts necessary to align the calculated XE and XAS spectra with the experiment.

Fig. 3.43 shows the XAS and XES spectra of imidazole (pH 10.3) at the carbon and the nitrogen K-edge. The nitrogen spectra are displayed in the top two graphs, while the bottom two graphs show the carbon spectra. In addition to the experimental spectra (black line), red, black, and green bars indicate the calculated transition probabilities for an *isolated* imidazole molecule. The different colors indicate at which atom the core level is located (see Fig. 3.42). The calculation was done with the StoBe-deMon DFT package. A detailed description of the calculation can be found in chapter 2.2.2. To account for vibrational, life-time, and experimental broadening, the calculated transition oscillator strength (bars) were broadened by Gaussian functions, which results in the blue spectrum. To achieve the illustrated agreement between calculation and experiment, the energy position of the theoretical spectra were aligned with the experiment hereby an independent shift of each core level binding energies was allowed and they are listed in table 3.2.

Starting with Fig. 3.43a, the NK emission of imidazole shows seven emission features between $E_{em}=398.0$ eV and $E_{em}=380.0$ eV. The feature with the highest emission energy is located at about $E_{em}=397.0$ eV and has a rather weak intensity. The dominating peaks are two narrow emission lines centered at $E_{em}=394.1$ eV and $E_{em}=395.5$ eV. On the low energy side, three broad and thus overlapping emission features, with decreasing intensity are visible. To model the spectrum, the transition oscillator strength of the occupied molecular orbitals with both nitrogen 1s core levels (N1, N3) were calculated. The similarities between the experimental NK XES spectrum (Fig. 3.43a), which shows an imidazole molecule in aqueous solution, and the calculated spectrum which represents an isolated imidazole molecule, indicate that the emission spectrum and thus the electronic structure of the occupied molecular orbitals surrounding the N1 and N3 nitrogen atoms might not or only little influenced by the aqueous environment. However, the necessary shift of the N3 component might be a hint of an underestimation of a possible interaction between the N3 atom and the surrounding water molecules. This is also supported by the obtained energy difference between the two nitrogen 1s core levels (N1, N3) of 2.5 eV. This value is larger than the value obtained by core level photoelectron spectroscopy measurements of Nolting

et al. [128] (1.7 eV), but is very close to calculations done by Thomason *et al.* [129] for free imidazole.

Fig. 3.43b shows the NK XA spectrum of imidazole (black). The NK absorption is dominated by two well separated absorption resonances located at $E_{\text{exc}}=400.0$ eV and $E_{\text{exc}}=401.7$ eV. A third resonance is visible at $E_{\text{exc}}=403.5$ eV. Again the experimental spectrum is compared to the theoretical calculation. Although the calculation does not produce a satisfactory XA spectrum, it proves that the two main absorption resonances are the result of a N 1s $\rightarrow \pi^*$ LUMO transition from the N1 nitrogen ($E_{\text{exc}}=400.0$ eV) and from the N3 nitrogen ($E_{\text{exc}}=401.7$ eV). The energy difference of 1.7 eV is in accordance to binding energy difference of the N 1s core levels measured by Nolting *et al.* [128] but does not fit to the calculations of Thomason *et al.* The absorption resonance at $E_{\text{exc}}=401.0$ eV is not observed in the experiment. This difference between the experimental and the calculated spectrum was already reported by Thomason *et al.* [129]. Thomason *et al.* stated that intermolecular hydrogen bonds affect the electron density around the N1 nitrogen, which causes a shift in the core level binding energy and suppresses the additional intensity between the absorption resonances. They also emphasize that direct imidazole to imidazole interactions have to be taken into account to describe the experimental XA spectrum correctly. In literature, the possibility of self-association, the spontaneous ordering of imidazole molecules in chains is assumed [130, 131]. The presented XE spectra, however, are rather uninfluenced by intermolecular hydrogen bonds which does not allow to draw any conclusion in regards of this hypothesis.

Fig. 3.43c illustrates the CK emission of imidazole (black) which consists of five emission features with three pronounced emission lines located at $E_{\text{em}}=283.2$ eV, $E_{\text{em}}=282.1$ eV, and $E_{\text{em}}=280.5$ eV. The calculation consists of three parts representing transitions into the three chemically non-equivalent carbon atoms (C2, C4, and C5) as red, green, and black bars. The calculation indicates that the three HOMO \rightarrow C 1s transition lines create the double peak structure: The emission feature with the highest emission energy can be attributed to the C2 1s atom while the C4 and C5 atoms are combined in the second emission feature. Besides the sharp HOMO features, the spectrum shows a rather strong intensity around $E_{\text{em}}=277.0$ eV, again implying that the molecular orbitals associated with this emission energy are localized at the carbon atoms.

Similar to the CK XE spectrum, the CK XA spectrum of imidazole illustrated in Fig. 3.43d, consists of three non-equivalent carbon atoms (red, green, and black bars). However, the individual resonances are very close together and thus overlapping. This creates a several eV broad absorption resonance which is followed by broad σ^* -like absorption features at higher excitation energies. The calculations of C2 and C4 (red and green) contribute only with one 1s \rightarrow LUMO transition, while the C5 calculation

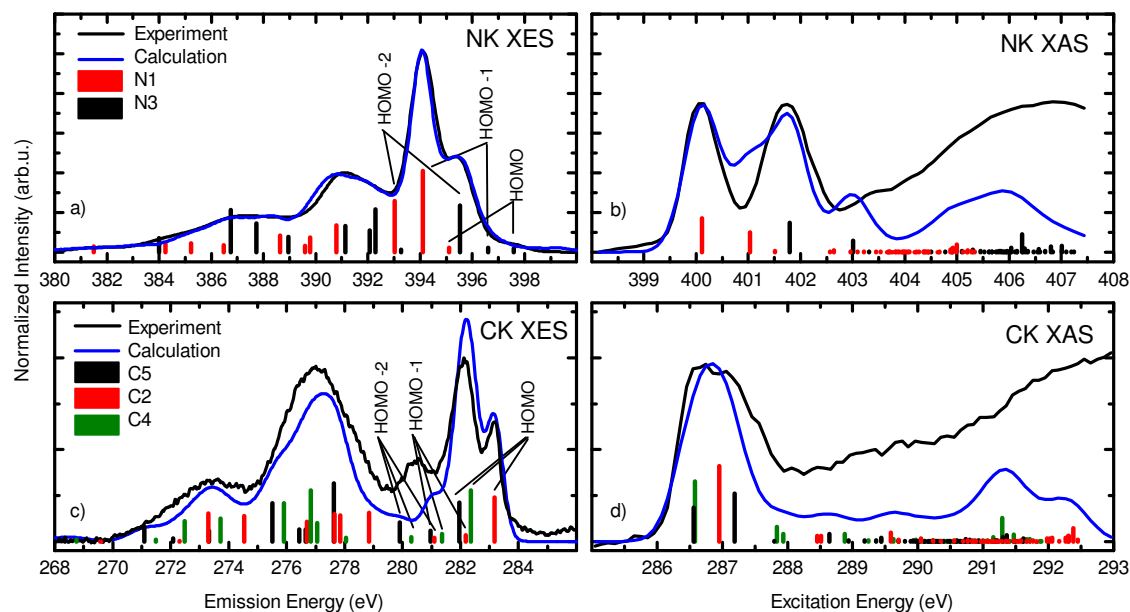


FIGURE 3.43. Experimental X-ray spectra of aqueous imidazole at pH 10.3 (black) compared with broadened DFT spectra of an isolated imidazole molecule (blue). Dipole oscillator strengths are shown as colored bars. a) NK XES excited at $E_{\text{Exc}} = 424\text{eV}$. b) NK XAS. c) CK XES excited at $E_{\text{Exc}} = 322\text{eV}$. d) CK XAS.

(black) shows two transitions: a $1s \rightarrow \text{LUMO}$ and $1s \rightarrow \text{LUMO}+1$ transition in this energy range.

The calculation illustrates that in case of the NK spectra the two non-equivalent nitrogen atoms are responsible for different emission features within the spectrum. In the non-resonant measurement (3.43a), both N1s core levels can be ionized and each occupied orbital decays into one of the two core levels resulting in two emission lines for each orbital. For the CK spectra, contributions from the three non-equivalent carbon atoms have to be taken into account. Since the symmetries of the five core levels are identical (s-symmetry), the probability of a single transition mainly depends on the spatial overlap between the valence orbital and the core orbitals. Hence the intensity of the transition can be seen as an indicator for the localization and the symmetry of the valence orbital. To illustrate this relationship, the isodensity surfaces of the three HOMO and two LUMO orbitals of imidazole are depicted in Fig. 3.44.

The orbitals displayed in Fig. 3.44 are extracted from the ground state frozen orbital calculation [64] and are all well distributed over the entire molecule. Although the molecule has only one high symmetry plane, the HOMO and HOMO-2 orbitals

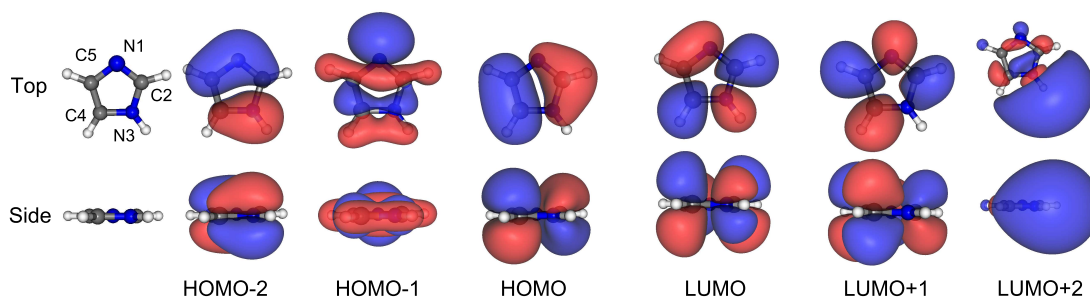


FIGURE 3.44. Isodensity surfaces of the highest occupied and first unoccupied molecular orbitals of imidazole calculated with the StoBe-deMon [58] package in the ground state frozen orbital approximation [64].

exhibit a nodal plane perpendicular to the molecular plane. The LUMO and LUMO+1 orbitals show even two. In case of the HOMO orbital, the nodal plane of the orbital at which the density of the orbital goes to zero (see Fig. 3.44) is located very close to the two nitrogen atoms (N1, N3), which is reflected in Fig. 3.43a where the HOMO emission shows a very small transition oscillator strength. The carbon atoms are further away from the nodal plane (see Fig. 3.44) and therefore a stronger transition oscillator is observed for the carbon atoms (see Fig. 3.43c).

In case of the HOMO-2 orbital the nodal plane is rotated by 90° , which results in a suppression of the dipole transition moments for the C2 and C4 carbons. Consequently, the transition dipole moments into the N1 1s and N3 1s core levels are very strong (see Fig. 3.43a and Fig. 3.43a).

In contrast to the HOMO and the HOMO-2 orbital, the HOMO-1 orbital is symmetric with respect to the molecular plain with a large electron density at the N1 nitrogen. The comparison between theory and experiment shows a large transition oscillator for the N1 nitrogen, while the oscillator strength for the N3 nitrogen almost vanishes (see Fig. 3.43a). Due to the large transition oscillator strength of the HOMO-1 with the N1 nitrogen, and the resulting strong signal in the NK XE spectrum, it can be speculated that this orbital is highly localized at the N1 nitrogen. The isodensity surface of this orbital depicted in Fig. 3.44 supports this hypothesis, although a significant electron density can be found spread over the entire molecule.

The nodal planes of the LUMO orbitals do not have such a strong effect on the spectrum as they have for the HOMO orbitals. Hence the origins of the differences in the oscillator strength of the LUMO transitions are more complicated and cannot simply be related to the localization of molecular orbitals. However, the calculation of the unoccupied orbitals is more complicated compared to a ground state frozen orbital (FO) approximation. XA signatures are highly influenced by relaxation effects

which are modeled in the calculation using the transition state (TS) calculation which includes a half filled core level [62]. Furthermore, the calculation can rearrange the order of the higher unoccupied molecular orbitals, which creates an uncertainty that makes a detailed interpretation of the calculation using the ground state frozen orbital calculations difficult. However, the isodensity surfaces of the transition state calculation (not shown) also show equally distributed LUMO and LUMO+1 orbitals, which again indicates that the origin of the transition oscillator strength cannot be seen in the mere localization of the LUMO orbitals.

Fig. 3.45 now shows the combined XE and XA spectra of the protonated imidazolium ion (ImH^+) at the CK and NK edge, respectively. The NK XE and XA spectra are displayed in Fig. 3.45a and 3.45b. The CK XE and XA spectra are illustrated in Fig. 3.45c and 3.45d. The transformation from imidazole to imidazolium ion changes not just the local electronic structure of the associated nitrogen atom, moreover, it changes the entire symmetry of the molecule which introduces a second mirror plane perpendicular to the molecular plane. Hence, the two nitrogen atoms N1 and N3, as well as the two carbon atoms C4 and C5 become identical. In all four spectra the experimental spectrum is displayed in black. Red and black colored bars indicate the calculated transition dipole moments using DFT frozen orbitals approximation for the XE and the transition state approximation for the XA spectra (for details see chapter 2.2.2). As in Fig. 3.43, the calculated transitions are convoluted with Gaussians to account for vibrational, life-time, and experimental broadening. The result is shown as a solid blue line.

Fig. 3.45a shows the experimental NK emission spectrum of imidazolium (imidazole pH 1.8) in black and two calculated spectra below. The regular frozen orbital XE spectrum is represented by the black bars and as orange line. It occurs that the calculated spectrum fits quite well to the experimental data except at $E_{\text{em}}=394.0$ eV. At this emission energy, the measurement features a small but distinct peak which is totally ignored by the calculation. From the NK XE spectra of a protonated α -amino group it was shown that the dissociation of a proton can influence the emission spectrum and thus creates large deviations from a regular frozen orbital calculation (e.g. see Fig. 3.19). The regular StoBe-deMon package does not allow time dependent DFT calculations as they were presented for the description of the NK XE spectrum of zwitterionic glycine (see Fig. 3.10). However, the fully dissociated case can be approximated by the N1 calculation of imidazole (shown in Fig. 3.43a) which is depicted by the red bars (N1*). To fit the experiment, the N1* calculation was shifted by -0.2 eV in respect to the N1 calculation in 3.43a. The sum of both species (dissociated, non-dissociated) is shown in blue. The spectral contribution of the dissociation (red) to the total spectrum (blue) amounts to 17%, which was chosen to give a best fit with the experimental

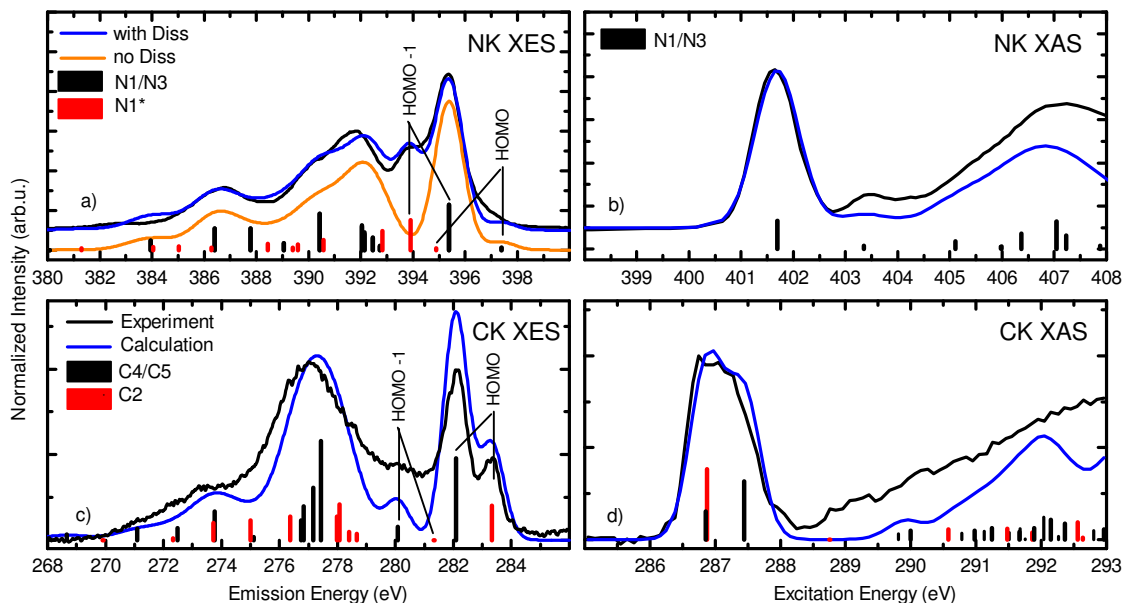


FIGURE 3.45. Experimental X-ray spectra of aqueous imidazolium—imidazole at pH 1.8—(black) compared with broadened DFT spectra of an isolated imidazole molecule (blue). Dipole oscillator strengths are shown as colored bars. a) NK XES excited at $E_{\text{exc}} = 424\text{ eV}$. b) NK XAS. c) CK XES excited at $E_{\text{exc}} = 322\text{ eV}$. d) CK XAS. The orange spectrum represents the calculated spectrum without dissociation effects.

spectrum.

The NK XA spectrum is displayed in Fig. 3.45b. A strong π^* absorption resonance is located at $E_{\text{exc}} = 401.6\text{ eV}$ and a second much weaker π^* absorption is visible at $E_{\text{exc}} = 403.4\text{ eV}$. Only one σ^* resonance is observed at $E_{\text{exc}} = 407.1\text{ eV}$. The reduced number of absorption resonances (compared to imidazole 3.43) is the result of the protonation induced symmetrization of the molecule which created two indistinguishable nitrogen 1s core levels. This is also reflected in the calculation which shows all three absorption resonances. The energetic position of the features is hereby in very good agreement to experiment and deviates only slightly for the σ^* resonance.

Fig. 3.45c displays the CK XE spectrum of the imidazolium ion. The protonation has a much smaller impact on the CK spectrum compared to the NK spectrum. The only visible difference between Fig. 3.45c and Fig. 3.43c is that for imidazolium (Fig. 3.45c) the feature at $E_{\text{em}} = 280.5\text{ eV}$ is much broader and hence much less pronounced than for imidazole (Fig. 3.43c). Besides the two nitrogen atoms, the protonation also equalizes two carbon atoms (C4 and C5) and only the C2 carbon is still chemically different. Hence the calculation consists of only two individual “spectra”. One for the

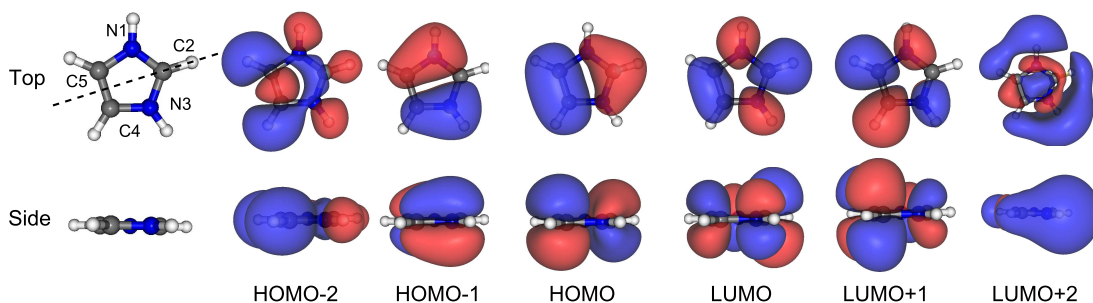


FIGURE 3.46. Isodensity surfaces of the highest occupied and first unoccupied molecular orbitals of imidazolium calculated with the StoBe-deMon [58] package in the ground state frozen orbital approximation [64].

transition into the C2 core hole and one for the transitions into the C4 and C5 core holes. The broadened calculation is again in a qualitatively good agreement with the experiment.

The CK XA spectrum of imidazolium is displayed in Fig. 3.45d. The spectrum shows a similarly broad π^* absorption resonance like imidazole (see Fig. 3.43d) with small but distinct differences. Compared to imidazole (see Fig. 3.43d), the absorption onset of imidazole is blue shifted by about +0.2 eV and shows a slightly smaller full width at half maximum (-0.4 eV). Furthermore, instead of the two σ^* absorption resonances (Fig. 3.43d), a steadily rising absorption edge is observed. The experimental spectrum is again well described by the calculation. The number of π^* transitions within the first absorption resonance is reduced to 3. The calculation indicates that the C2 carbon contributes with a single $1s \rightarrow$ LUMO transition, while the C4 and C5 carbons contribute with two transitions: a $1s \rightarrow$ LUMO and a $1s \rightarrow$ LUMO+1 transition. For the C2 carbon the LUMO+1 transition is shifted to higher excitation energies and is strongly suppressed.

As for the imidazole, the calculated intensities of the dipole transitions are an indication for the symmetries and the localization of the molecular orbitals. Fig. 3.46 illustrates isodensity surfaces of the three highest occupied molecular orbitals (HOMOs) and the three lowest unoccupied orbitals (LUMOs) as they were obtained by the ground state frozen orbital (FO) calculation done with the StoBe-deMon package. As for the imidazole orbitals depicted in Fig. 3.44, the FO approach is just an approximation for the LUMO orbitals.

The orbitals depicted in Fig. 3.46 nicely show the additional symmetry plane which is indicated by the dashed line. The C2 carbon atom is located directly on the new

symmetry plane. For the HOMO-1 and the LUMO +1 orbitals the symmetry plane simultaneously is also a nodal plane of the orbital. Hence transitions of these orbitals with the C2 core level are very weak (see Fig. 3.45c and 3.45d) whereas the transitions to the off plane nitrogen (N1 and N3) and carbon (C4 and C5) core levels are much larger.

In contrast to the HOMO-1 and LUMO+1 orbitals, the nodal plane of the HOMO orbital is very close to the two nitrogen atoms. Hence the transition from this orbital into the N1 and N3 core levels is suppressed, while the transition into the carbon core levels is allowed (see Fig. 3.45a, and 3.45c).

The imidazole and imidazolium molecules proved to be very stable under the intense X-ray radiation beam. Apart from the dissociation of a hydrogen proton observed in the NK XE spectrum of imidazolium, no beam damage could be detected. Furthermore, in contrast to pyrrolidine, no contamination of the membrane by the adsorption of molecular fragments was observed. This allows to record resonant inelastic X-ray scattering (RIXS) maps of both absorption edges of imidazole at two pH-values. The result is shown in Fig. 3.47 and Fig. 3.50.

The NK RIXS maps of imidazole (Im) and imidazolium (ImH) are displayed in Fig. 3.47a and Fig. 3.47b. Within the RIXS maps the X-ray emission intensity is color coded and plotted as a function of excitation and emission energy. The 2-dimensional RIXS map allows to extract XE and XA spectra at each excitation and emission energy, resulting in either a resonantly excited XE spectrum, or a decay channel specific partial fluorescence yield XA spectrum, respectively. The XA spectra of imidazole and imidazolium shown in Fig. 3.43 and Fig. 3.45 are also created using the RIXS maps. For the NK XA spectra the emission intensity between $E_{em}=380.0$ eV and $E_{em}=398.0$ eV was integrated and displayed as a function of excitation energy.

The RIXS maps show the combined XES and XAS information and hence provide comprehensive information about the electronic structure of the investigated molecule. Besides the electronic transitions between orbitals, the RIXS map also contains transitions, which are caused by the excitation of higher vibrational modes of the electronic ground state.

Fig. 3.47a shows the NK RIXS map of imidazole. In addition to the Rayleigh line (elastically scattered light) at equal excitation and emission energy, as well as vibrational “losses” close to the Rayleigh line, the RIXS map exhibits a spectator emission pattern rich on spectral features. With increasing excitation energy, the map can be read like an absorption spectrum. Two well separated resonances are visible (A and B). These resonances correspond to the XAS resonances shown in Fig. 3.43b. Each of these resonances consists of three emission features of different intensity. Fig. 3.48a shows the 1-dimensional RIXS spectra obtained at these two excitation energies. At higher excitation energies, the emission signature of both resonances (A and B)

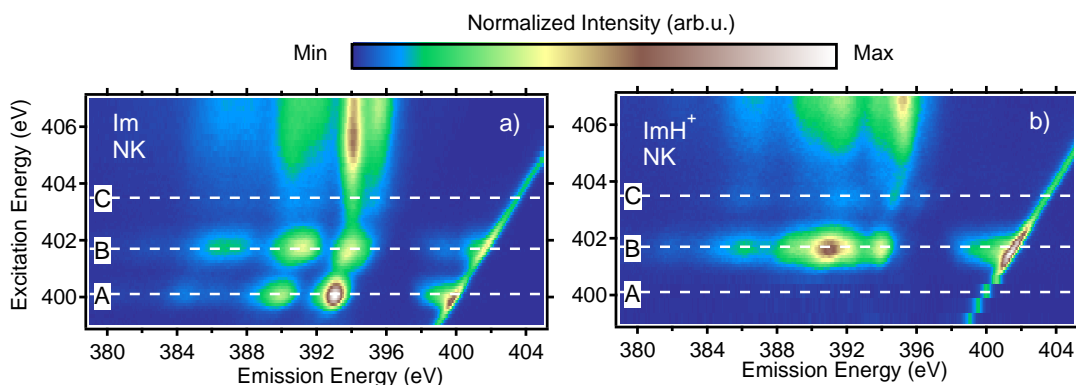


FIGURE 3.47. RIXS maps of imidazole (Im) (a) and imidazolium (ImH⁺) (b) at the nitrogen K-edge. The X-ray emission intensity is color coded and displayed as a function of excitation and emission energy.

becomes visible simultaneously. .

The NK RIXS maps of imidazolium is displayed in Fig. 3.47b. At $E_{\text{exc}}=401.7$ eV a strong absorption resonance is observed, which comes along with enhanced vibrational “losses”. The resonance itself shows a broad emission spectrum (B). At higher excitation energies a second much weaker resonance can be observed $E_{\text{exc}}=403.4$ eV (C). The 1-dimensional RIXS spectra obtained at these excitation energies are depicted in Fig. 3.48b. For a better comparison between imidazole and imidazolium, the RIXS spectra obtained at $E_{\text{exc}}=400.1$ eV and $E_{\text{exc}}=403.4$ eV were added to Fig. 3.48b and 3.48a, respectively. The non-resonantly excited XE spectra are plotted as reference in the top of the graphs (D). In the following the RIXS spectra will be discussed on the basis of Fig. 3.48.

As it became obvious from the calculated XAS spectrum depicted in Fig. 3.43b, at the first absorption resonance ($E_{\text{exc}} = 400.1$ eV) only the N1 nitrogen atom of imidazole is excited, which means that for the emission, only transitions into the N1 core level are possible. Hence, the RIXS spectrum (A) observed in Fig. 3.48a *solely* reflects the local transition dipole moment of the occupied molecular orbitals at the site of the N1 nitrogen. For imidazolium (Fig. 3.48b), the N1 nitrogen is protonated which results in a blue shift of its binding energy. Therefore, the excitation energy of $E_{\text{exc}} = 400.1$ eV cannot excite the core levels and consequently, no emission spectrum is observed at this excitation energy.

Spectrum (B), illustrated in Fig. 3.48a and Fig. 3.48b, was extracted at an excitation energy of $E_{\text{exc}} = 401.7$ eV. For imidazole as well as imidazolium, this excitation energy corresponds to the resonance energy for the N3 1s core level. In case of imidazole, also the N1 core level can be excited at this energy. Hence one has to assume that spectrum (B) does not solely consist of emission into the N3 core level. In case of

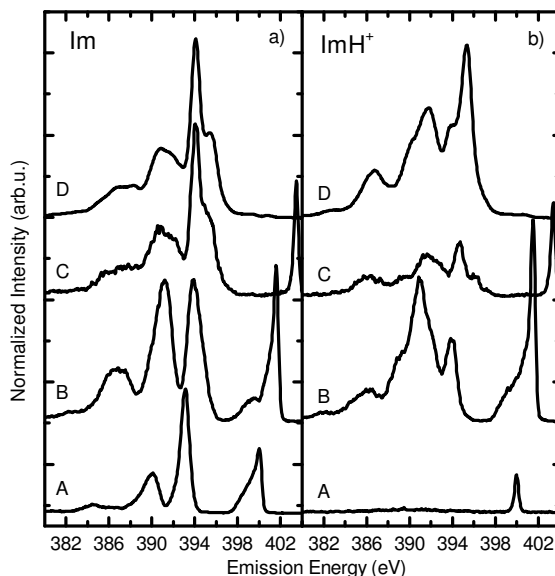


FIGURE 3.48. NK RIXS spectra of Imidazole (Im) (a) and Imidazolium (ImH⁺) (b) extracted from the RIXS maps displayed in Fig. 3.47. The spectra D are both non-resonantly excited XE spectra measures separately from the RIXS map ($E_{\text{Exc}} = 424 \text{ eV}$).

imidazolium, both nitrogen atoms are equal (due to the protonation) and the RIXS spectrum (B) shows emission into both core levels. The differences between the two RIXS spectra (B) of imidazole and imidazolium are prominent and are the result of the different symmetries of the molecules and the resulting different dipole matrix elements. Besides the different symmetries resonant effects have to be taken into account which again are different for the two symmetries which make a comparison of the resonant spectra of the two molecules very complicated.

Spectrum C was recorded at $E_{\text{exc}} = 403.4 \text{ eV}$. In case of imidazole (Fig. 3.48a), the spectrum is almost identical to the non-resonantly excited spectrum (D) and shows already large similarities to a summation of the two RIXS spectra (A and B). In case of imidazolium (Fig. 3.48b), this excitation energy corresponds to the excitation into the LUMO+1 orbital (see Fig.3.45b). The comparison of spectrum (B) and spectrum (C) shows that the RIXS spectrum strongly changes with respect to the orbital excited in the intermediate state.

Although the calculations displayed in Fig. 3.43 and Fig. 3.45 are only valid for the non-resonantly excited XE spectra and although the RIXS process introduces a second set of dipole selection rules [29, 132] as well as screening effects [133], these calculations can be used as a first approximation to interpret RIXS spectra. Furthermore, differences between the experiment and the calculation are an indication for resonant effects. The result is displayed in Fig. 3.49 which illustrates the NK RIXS

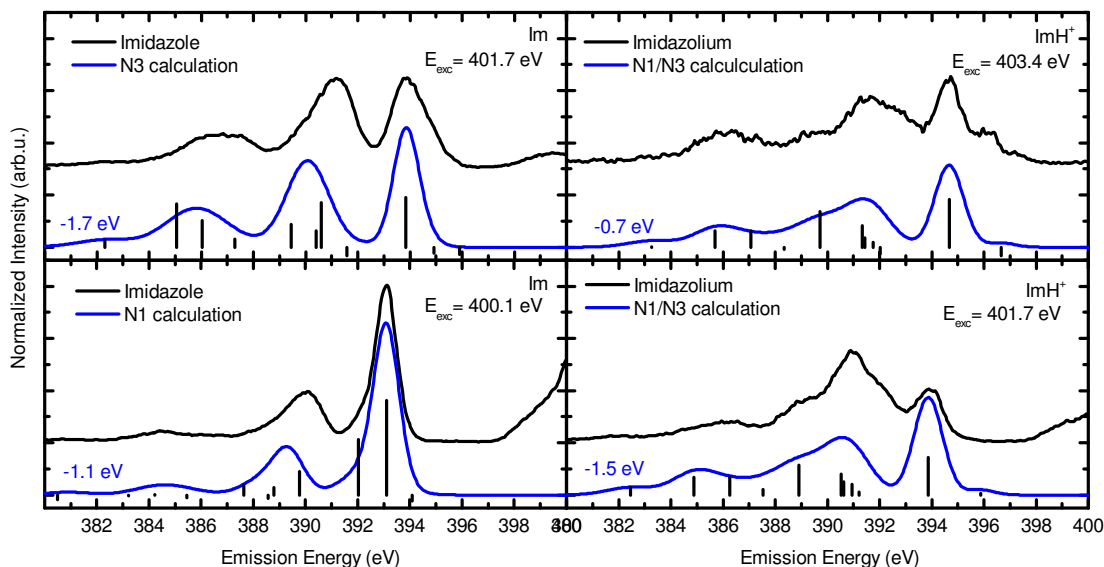


FIGURE 3.49. NK RIXS spectra of Imidazole and Imidazolium extracted from the RIXS maps displayed in Fig. 3.47 (black). Compared to the N1 and N3 components of the calculated non-resonantly excited XE spectra of imidazole and imidazolium.

spectra of imidazole and imidazolium (black). The calculated non-resonantly XE spectra are depicted in blue. The calculations are aligned to the highest emission feature accounting for the spectator shift which occurs due to screening of the core level upon resonant excitation [133]. Fig. 3.49a and Fig. 3.49c show the N3 and N1 RIXS spectra of imidazole (A and B), respectively. The figures 3.49b and 3.49d show again the two absorption resonances of imidazolium (B and C).

In case of imidazole, both RIXS spectra are nicely reproduced by the calculation. By aligning the calculation to the RIXS spectra, only the screening effect of the electron on the core level is included and the screening effect on the valence levels is neglected. This is a rough approximation. In both RIXS spectra (a) and (c), spectral lines attributed to the lower lying orbitals exhibit a much weaker screening induced shift. Ågren *et al.* [133] have shown that the magnitude of the screening strongly depends on the valence character of the LUMO orbital and the localization of the participating molecular orbitals. For rather small molecules (carbon monoxide, CO), the comparison to sophisticated theoretical calculations can shed light on the exact origin of the screening. For CO Ågren *et al.* found indications that the screening is mainly caused by the relaxation of the spectator electron in the LUMO level [133, 134]

For imidazolium the agreement between the two RIXS spectra and the XES calculations is not as good as for the imidazole molecule. Besides energetic shifts

caused by the spectator electron, also the intensities of the RIXS transitions are quite different from the non-resonant calculation. In the first absorption resonance (see Fig. 3.49d) ($E_{\text{exc}} = 401.7 \text{ eV}$), the HOMO-1 transition is significantly suppressed compared to the calculation, while the HOMO-2 to HOMO-5 transitions are enhanced. In the second resonance (see Fig. 3.49b) ($E_{\text{exc}} = 403.4 \text{ eV}$), the RIXS spectrum shows an enhanced HOMO transition, while the HOMO-6 transition is suppressed. The differences between experimental spectra and calculation, as well as between first and second resonance are the result of a superposition of effects.

Firstly, the symmetry of the intermediate state, which is defined as the direct product of the irreducible representations of the ground state, the dipole moment operator, and the the core-excited state ($\Gamma^0 \times \Gamma^d \times \Gamma^i$) [29], is unique for the two absorption resonances.

Secondly, due to different screening induced energetic shifts, transitions might overlap or separate. It is also reported that the screening effect has an effect on the intensity of a transition. However, in general, it is assumed that the latter effect is rather weak [133–136].

Thirdly: at resonant excitation, the spectrum is also influenced by polarization characteristics, which creates “a specific angular distribution pattern (specific polarization anisotropy, specific parity selection) and which has no counterpart in non-resonant emission spectra” [134]. The anisotropy of the RIXS emission is caused by the symmetry of the core excited state. Combined with the assumption that the molecule is immobile during the entire RIXS process the linear polarized light will selectively excite mainly molecules, which are oriented in a way that the dipole moment of the unoccupied molecular orbital is parallel to the polarization vector of the incoming light. Since the emission takes place before the molecule rotates, the angular distribution of the emission depends on the symmetry (dipole moment) of the decaying occupied molecular orbital. Hence at resonant excitation, the intensity of a single transition depends on the geometry of the experimental setup. In contrast to resonant excitation, in “the non-resonant case, the core electron is excited into the continuum, which is infinitely degenerate, representing all symmetries” [134], which makes the non-resonant emission much less sensitive to any symmetry related selection rules imposed by the molecule or the experimental setup. However, by accounting for the polarization anisotropy during the RIXS process, one has to differentiate between the two-step model and the one-step scattering model, because the polarization anisotropy can be different for different intermediate state constellations [132].

Luo *et al.* investigated the influence of the model used (one-step, two-step) onto the different polarization features on four different example molecules [132] and observed quite large differences depending on the model, the number of intermediate states, and the number of interfering core-excited states that were used. For a single

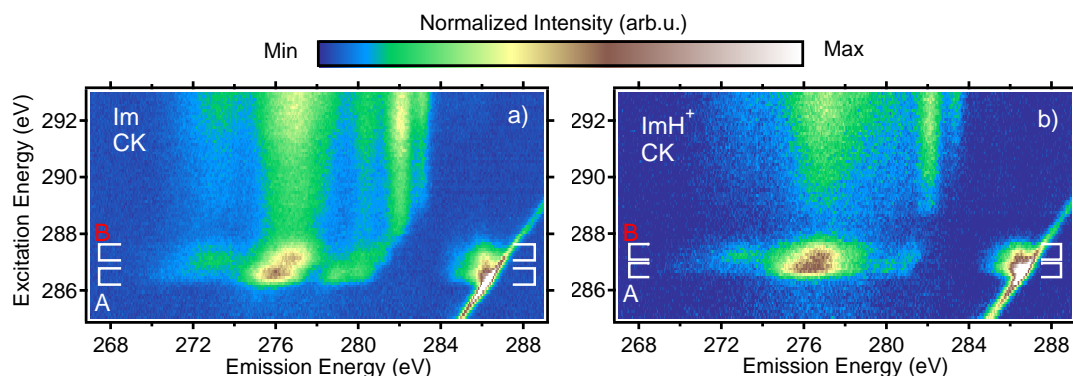


FIGURE 3.50. RIXS maps of imidazole (Im) (a) and imidazolium (ImH⁺) (b) at the carbon K edge. The X-ray emission intensity is color coded and displayed as a function of excitation and emission energy.

core level decay channel, interference can be neglected and the two-step model can be simplified to a classical relation between XE intensities of non-resonantly and resonantly excited randomly ordered samples (which is the case for the two NK RIXS spectra of imidazole). In case of imidazolium, the two core levels are identical which results in two close-lying core-excited intermediate states. In this case, no simple classical relation can be obtained for the polarization anisotropy.

In conclusion, in case of imidazolium polarization anisotropy, screening effects, and symmetry of the intermediate states have a large impact on the NK RIXS spectra, which is the reason why the approximation of the NK RIXS spectra with non-resonant calculations fails.

Fig. 3.50a illustrates the CK RIXS map of imidazole and the CK RIXS map of imidazolium (Fig. 3.50b). As for the NK RIXS maps, the Rayleigh line is visible at equal excitation and emission energy. For both molecules, close to the Rayleigh line a distinctive vibrational “loss” tail can be observed. For the CK XA spectra in Fig. 3.43d and Fig. 3.45d, the emission intensity between $E_{em}=268.0$ eV and $E_{em}=284.0$ eV was integrated and displayed as a function of excitation energy.

The CK RIXS map of imidazole (Fig. 3.50a) reveals that the first absorption resonance can be divided into two spectral components which are shifted in emission energy with respect to each other. The two components are extracted from the map and displayed in Fig. 3.51d. To improve the signal to noise ratio of the RIXS spectra, parts of the absorption resonance were integrated. The area of integration is indicated by the open rectangles marked with A and B. The shift in emission energy is again the result of screening effects. The emission pattern of the resonances consists of four spectral features with the highest intensity at about $E_{em}=276.0$ eV. At higher

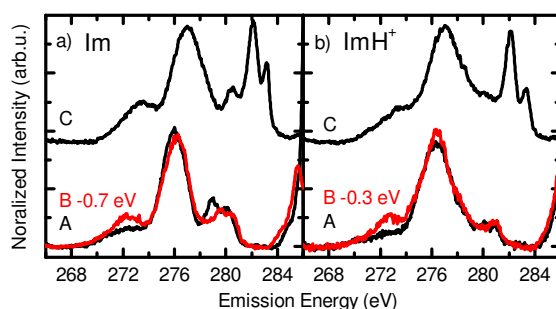


FIGURE 3.51. CK RIXS spectra of Imidazole (Im) (a) and Imidazolium (ImH⁺) (b) extracted from the RIXS maps displayed in Fig. 3.50. Spectrum C shows a non-resonantly XE spectra recorded separately from the RIXS map.

excitation energies, new emission features appear at $E_{em}=282.1$ eV and $E_{em}=283.0$ eV. The intensity of all emission features increases with increasing excitation energy.

The CK RIXS map of imidazolium (Fig. 3.50b) shows also a double peak structure in the first absorption resonance. Similar to imidazole, the RIXS spectra of the first absorption resonance of imidazolium were extracted by the integration of a 0.5 eV excitation energy range marked with an open rectangle (A, B). The resulting spectra are displayed in Fig. 3.51c.

Similar to imidazole, the emission pattern of both resonances show three features with the highest intensity at about $E_{em}=276.1$ eV. Again, at higher excitation energies two comparable emission features appear at $E_{em}=282.0$ eV and $E_{em}=283.2$ eV.

Fig. 3.51a and 3.51b illustrate the two RIXS spectra of the two components of the first absorption resonance (A and B) and the non-resonantly excited XE spectrum (C) for imidazole (a) and imidazolium (b), respectively. In both graphs, spectrum B was shifted to account for the spectator shift and to allow a better comparison with spectrum A. The shift amounts for imidazole to -0.7 eV and for imidazolium to -0.3 eV.

After this shift of the CK RIXS spectrum, strong similarities between spectrum A and B as well as between imidazole and imidazolium, for which also the non-resonantly excited spectra (C) show several common features are observed. The three emission features are visible in all four CK RIXS spectra. In addition, the high energy feature of imidazole exhibits a double peak. Comparing the RIXS spectrum of the first resonance (A) with the RIXS spectrum of the second resonance (B), it appears that for imidazole the emission at about $E_{em}=272$ eV increases while the emission at about $E_{em}=279$ eV decreases. For imidazolium, only the low energy part of the spectrum is changing (increase at $E_{em}=272$ eV).

The difference between the RIXS spectra and the non-resonantly excited XE spectra is more dramatic. Upon resonant excitation the two emission intensities,

which could be related to the HOMO \rightarrow C1s transitions (imidazole: $E_{em}=282.1$ eV and $E_{em}=283.0$ eV, imidazolium: $E_{em}=282.0$ eV and $E_{em}=283.2$ eV), are completely quenched for both molecules. The fact that it occurs for both molecules is puzzling. Both molecules have different symmetries and neither of them has an inversion symmetry, which could explain the quenching of resonant transitions [29, 137, 138]. In case of imidazole, three close lying core excited states exist, which make a simple calculation for the polarization anisotropy not possible. The same is the case for imidazolium, where two of the three states are even degenerated. The interference of these close-lying intermediate states can cause such a quenching [139], but this hypothesis can only be validated by detailed theoretical calculations of the RIXS process in a one-step scattering model. Similar to the intensity differences in the NK RIXS spectra of imidazolium, so far the quenching of the HOMO emission at resonant excitation could not be attributed to a single effect.

3.3.3 Summary

In this chapter the electronic structure of histidine and imidazole was investigated in detail. Upon protonation and deprotonation of the functional groups, large changes in the XE and RIXS spectra of the functional groups were observed. Furthermore, apart from some fine structures, the OK RIXS spectra of aqueous histidine at different pH-values could be approximated by OK RIXS spectra of aqueous acetic acid at suitable pH-values. This is consistent with the building block approach introduced in chapter 3.1.1. The NK XE spectra of histidine could also be modeled using suitable reference molecules. Since histidine has a polar side-chain which can also be protonated and deprotonated, two reference molecules were chosen to model its NK XE spectrum. The spectral fingerprint of the α -amino group was approximated by the NK XE spectrum of cysteine, while the NK fingerprint of the side-chain was approximated by the NK XE spectrum of imidazole. For each reference molecule a spectrum of the protonated and the deprotonated configuration was used. By the summation of different combinations of the four reference spectra, the spectra of histidine at the different charge states could be modeled successfully.

As the amino acid proline, histidine was decomposed within the intense X-ray beam and molecular fragments adsorbed to the membrane. Due to this contamination of the membrane, no RIXS maps of histidine could be measured. To investigate the unique electronic structure of the side-chain of histidine, the reference molecule imidazole was investigated in aqueous solution.

The imidazole solutions did not show any sign of adsorbed molecular fragments which made it possible to record RIXS spectra at the NK and CK absorption edge at different pH-values. Similar to histidine, upon protonation of the nitrogen atom,

strong changes in the NK XE and XA spectra could be observed. For the CK XE and XA spectra the changes are not as pronounced as for the NK XE and XA spectra. Calculated XE and XA spectra of an isolated imidazole and imidazolium molecule, which were generated with the StoBe-deMon DFT package, were in a good agreement with the experimental spectra. Based on the calculations, emission and absorption features in the XE and XA spectra could be assigned to single molecular orbitals. Moreover, based on the local structure of the molecular orbitals, changes in the XE and XA intensities could be understood.

The recorded NK and CK RIXS spectra of imidazole and imidazolium show strong resonant effects which manifest in a superposition of screening, polarization anisotropy, and channel interference. In case of the NK RIXS spectra of imidazole, the two non-equivalent nitrogen atoms could be separated experimentally and be validated by the comparison to non-resonant calculations. In case of the NK RIXS spectrum of imidazolium and the CK RIXS spectra of both molecules, the origin or the absence of certain features are not yet fully understood and are a potential starting point of further investigations.

ION-SOLVATION-INDUCED MOLECULAR REORGANIZATION IN LIQUID WATER

The focus of the previous chapter was set on the electronic structure of amino acids and the development of a building block model for the interpretation of XE and RIXS spectra using suitable reference molecules. In this chapter the focus will be set on the electronic structure of the solvent: the water molecules. Water is a seemingly simple molecule, consisting of an oxygen atom and two hydrogen atoms. Because of the lone pair electrons of the oxygen, the molecule is not linear. Due to its size, it should be easy to describe it with theoretical calculations. However, in the liquid state the dynamic character of the water network makes a precise description very complicated.

In the solid phase, the water molecules are arranged in a crystalline structure in which the water is coordinated preferably in a tetrahedral configuration. Hereby, the single water molecules are connected through hydrogen bonds (HB). In the liquid phase, the order gets distorted. This most likely results in a reduced number of hydrogen bonds per water molecule [108, 140]. Due to dynamic changes within the water network, the determination of the number of hydrogen bonds becomes very complicated. By the addition of salt to water, the network will undergo further changes induced by the ionic solvation [141, 142].

The molecular structure of liquid water has been investigated using various experimental and theoretical approaches [113, 143–148]. Hereby, different approaches and methods were used, e.g., the local coordination of the atoms with electron diffraction and X-ray or neutron scattering [149–151]. Other experiments targeted the vibrational characteristics or the local electronic structure using infrared, Raman, photoelectron,

and resonant Auger electron spectroscopy [108, 149, 152, 153]. In recent years, also synchrotron-based soft X-ray spectroscopic techniques like X-ray photoelectron spectroscopy (XPS), X-ray absorption spectroscopy (XAS), X-ray emission spectroscopy (XES), and resonant inelastic X-ray scattering (RIXS) spectroscopy were applied [13, 79, 106–111, 140, 153–157].

As it was demonstrated in the previous chapter, XE spectroscopy and in particular RIXS contain comprehensive information about the electronic structure of a system and thus can give insight into the local structure of the water network and the character of the hydrogen bonds. Furthermore, the element selectivity of X-ray experiments allows the investigation of specific atomic species and thus for example separate the solute from the solvent.

The electronic structure of the pure water network was already investigated with XES and RIXS by several groups [79, 155, 158]. The observed results, however, created an intensive debate [106–108, 156, 157] which has not been fully agreed on yet. As a next step towards a deeper understanding of the liquid water network and the solvation of molecules in water, work has been published about the influence of ions onto the water [159–161] using mainly X-ray absorption spectroscopy as a tool for investigation. Ions in water are hereby good model systems since in a simple picture, they can be treated as a single electrostatic charge that perturbs the water network, while the amino acids, discussed above, also exhibit a 3-dimensional structure.

By understanding the solvation behavior of ions in water and the impact the ions have on the water, the foundation for further research is set. Combining the knowledge about salt solutions with the knowledge about amino acids and extending this to peptides and proteins, the fundamental forces behind the Hofmeister effect might be revealed.

In the following chapter the influence of potassium chloride (KCl) on the electronic structure of aqueous water will be investigated. The data presented in this chapter is the output of a cooperation with the university of Heidelberg and was published in “The Journal of Physical Chemistry Letters” [76] the displayed graphs are inspired by the graphs of the publication.

4.1 The X-ray Spectra of Liquid Water

To be able to investigate the influence of potassium chloride (KCl) on the water network with X-ray spectroscopy the spectrum of pure water has to be discussed briefly.

Fig. 4.1a illustrates the non-resonantly excited X-ray emission spectrum of liquid water at the OK-edge, while in Fig. 4.1b the X-ray absorption edge is displayed. Fig. 4.1c shows the isodensity surfaces of the four occupied and two unoccupied molecular orbitals in ground state configuration for an isolated water molecule.

The XE spectrum of liquid water consists of three emission features which are associated to three final state configurations ($1b_2^{-1}, 3a_1^{-1}, 1b_1^{-1}$) which can be related to the three highest occupied molecular orbitals ($1b_2, 3a_1, 1b_1$) of water (see Fig. 4.1c). The emission from the $2a_1$ orbital is not shown in this energy window. Since the $1b_2$ orbital consists of O 2p and H 1s orbital components in literature, it is attributed to the internal O-H bonds [162]. The $3a_1$ orbital consists of the O 2s and the O2p_z orbitals and is therefore attributed as hydrogen bond (HB) acceptor [155, 162]. The $1b_1$ orbital is associated with the O2p_x lone pair orbital. This orbital is fully occupied and does not participate in any molecular bonds. Because of this, the orbital is rather insensitive to molecular vibrations which together with the strong p-character, results in a strong single emission line [155, 162]. This is true for XPS measurements as well as for XES measurements on gas-phase water [143, 154]. However, XES experiments of liquid water seemingly show a splitting of this emission feature (see Fig. 4.1a). A low energy component ($1b_1^{LE}$) is located at $E_{em}=526.0$ eV and a high energy component ($1b_1^{HE}$) is centered at $E_{em}=526.8$ eV. The double peak structure shows a pronounced isotope effect, but is only little influenced by temperature changes [106, 107, 163].

The origin of the splitting in the $1b_1^{-1}$ emission has been under debate within the soft X-ray emission community. Consequently, two different interpretations about the presence of this double peak structure can be found in literature [106, 107].

On the one hand, the double peak structure is assumed to be caused by the presence of two water “species“, both being in a different geometric configuration. In this interpretation, the HE peak is assigned to water molecules showing an intact ice-like hydrogen bond (HB) network, while the LE component is assigned to a strongly distorted water molecule which has significantly less HBs [107]. Accordingly, both water species create an independent XE spectrum that is described by the two different initial states.

On the other hand, the HE emission is assigned to the $1b_1$ orbital of intact water molecules, while the LE emission is caused by ultra fast molecular dissociation. In this interpretation the spectrum consist of two independent contributions for which the HE feature represents the initial state configuration, while the LE feature is a final state effect which is mediated by the presence of intact hydrogen bonds [79, 106].

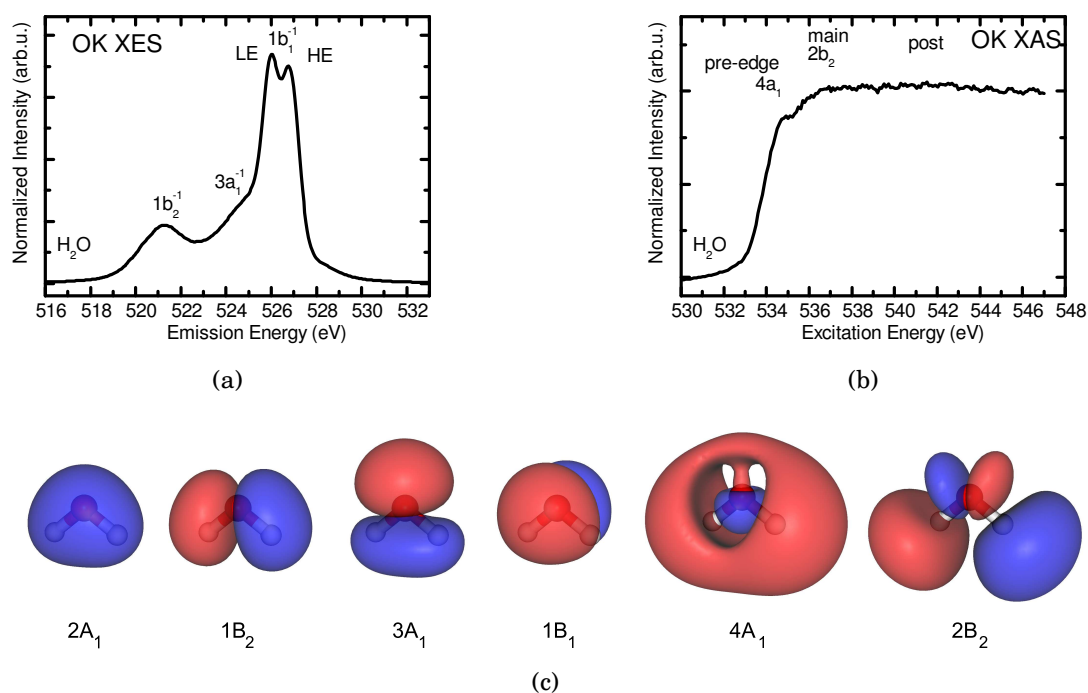


FIGURE 4.1. (a) X-ray emission spectrum of liquid water ($E_{\text{Exc}} = 550 \text{ eV}$). (b) X-ray absorption spectrum of liquid water. (c) Isodensity surfaces of the four occupied and two unoccupied valence orbitals of H_2O

In numerous publications the interpretations were analyzed [79, 110–113]. The interpretation based on ultra-fast dissociation is strongly supported by the strong isotope effect and the excitation dependent behavior of the features. A recent study also points out that the ultra-fast dissociation of the water molecule during the core hole lifetime of the X-ray emission process is promoted by the presence of intact hydrogen bonds [164]. This supports the model of a superposition of the spectral components of intact and dissociated H_2O [106].

Note that in this interpretation the presence of hydrogen bonds is necessary because they promote the dissociation process. The number of HBs of a particular molecule is then only indirectly responsible for the ratio between HE and LE peak, which is in accordance with the observed weak temperature effect.

The XA spectrum of H_2O displayed in Fig. 4.1b shows two absorption resonances labeled as pre- and main-edge which can be attributed to the unoccupied $4a_1$ and $2b_2$ orbitals, respectively. The presented XA spectrum was recorded using the fluorescence yield. This results in the strong suppression of the post-edge feature which is much more pronounced in electron yield and transmission experiments. In literature, the pre-edge ($E_{\text{exc}} \sim 534 \text{ eV}$) and main-edge ($E_{\text{exc}} \sim 536 \text{ eV}$) are associated with distorted hydrogen bonds, while the post-edge ($E_{\text{exc}} \sim 540 \text{ eV}$) is associated with a fully intact (tetrahedral) hydrogen bonding network [108, 109]. These interpretation points into

the same direction as the interpretation of the XE spectrum with two structural motifs.

The strong self-absorption effect present in FY-XAS measurements does not allow a quantitative analysis of the spectrum. Hence from the data evaluated in this thesis this interpretation cannot be validated or disproved.

By the addition of salt ions to liquid water, the hydrogen bonding network is expected to react and to undergo distinctive changes due to the reorganization of the water molecules around the salt ions forming a hydration shell [142, 159]. The influence of salt on the water network was investigated on a molecular level using a wide range of methods [141, 165]. Most of the previous soft X-ray studies were based on X-ray absorption measurements [159–161, 166, 167].

In general, changes in the three absorption features of the water spectrum (the pre-, main-, and post-edge) were associated with a change in the number of distorted (pre-, main-edge) or intact (post-edge) hydrogen bonds. The observed changes are an indication for the large influence of the salt ions and the extended rearrangement of hydrogen bonds. It also shows that XA spectroscopy is a suitable method to tackle this research question.

However, XAS measurements alone can only provide information about the unoccupied molecular orbitals ($4a_1$ and $2b_2$). The post-edge is related to Rydberg like states. With XE spectroscopy this picture can be completed and comprehensive information about the electronic structure and thus the structural influence of the salt ions onto the hydrogen bonding network can be recorded. Yet also far only very limited work has been performed [168, 169].

4.2 Aqueous KCl Solutions

In this chapter the influence of potassium chloride (KCl) on the water network is investigated by recording RIXS maps as well as non-resonantly excited OK XE spectra of aqueous salt solutions with different concentrations.

Pure liquid water, which was bought from Sigma Aldrich (ultra pure), as well as five salt solutions of different concentrations were investigated. The KCl was also bought from Sigma Aldrich (99% purity) and used without further purification. For the solutions, 1.864 g, 3.727 g, 5.591 g, 7.455 g, and 11.183 g KCl were solved in 25 ml H₂O. This results in salt concentrations of roughly 1 M, 2 M, 3 M, 4 M and 6 M, respectively. The 6 M solution represents already a supersaturated solution. In the following the different samples will always be labeled by means of their approximate concentration.

Fig. 4.2 shows the OK RIXS maps of pure liquid water and a 3M KCl solution. In the RIXS maps the X-ray emission intensity is plotted as a function of emission energy and excitation energy. The emission can be divided into two classes of emission features: the spectator emission (the emission intensity below 529 eV) and the participant emission visible around the Rayleigh line (elastic scattered light, visible at equal excitation and emission energy) which is magnified. The term “participant” emission is related to the radiative decay of the core excited electron, namely the electron participating in the excitation (X-ray absorption) process. The participant decay is mainly attributed to excited vibrations. The decay of valence electrons into the core hole is then called “spectator” emission.

The RIXS maps displayed in Fig. 4.2a and 4.2b both show the expected absorption

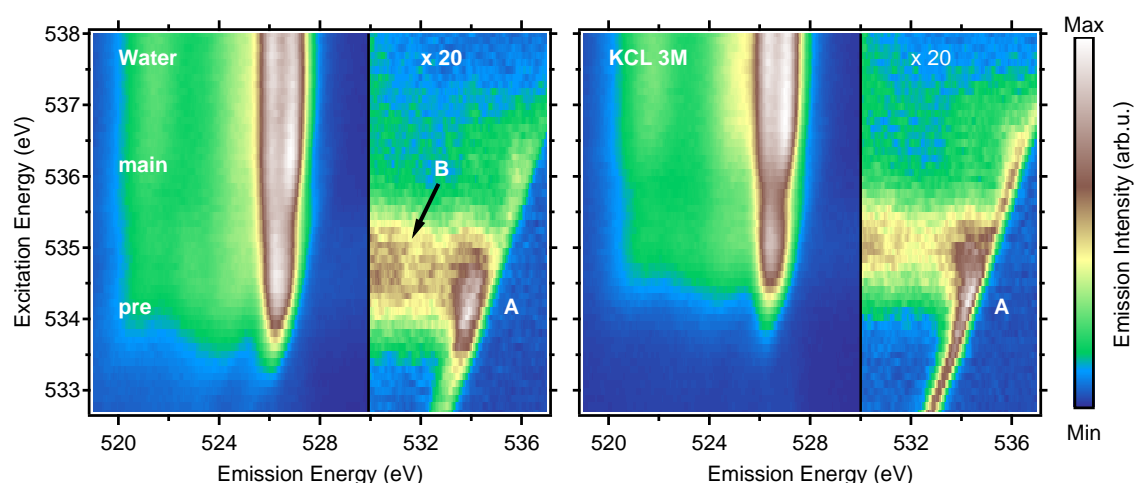


FIGURE 4.2. left: OK RIXS map of liquid water. right: OK RIXS map of aqueous KCl solution (3M).

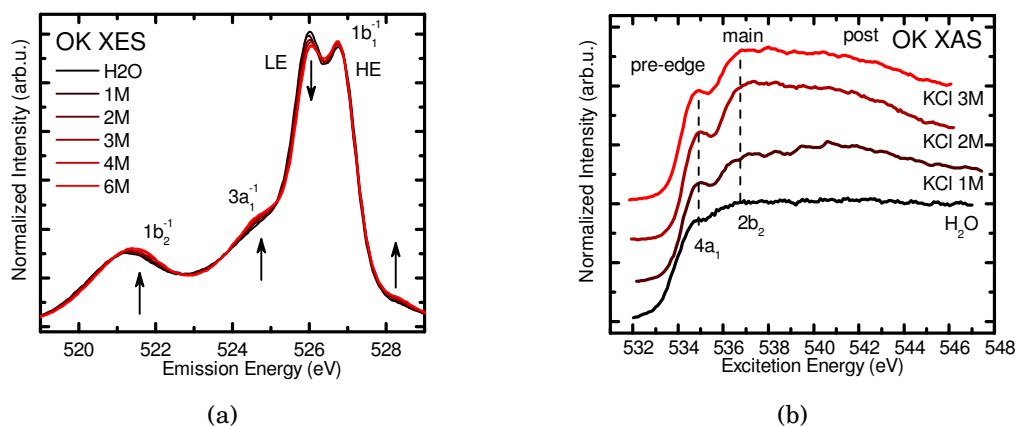


FIGURE 4.3. a) Non-resonantly excited OK-edge XE spectra of aqueous H_2O and aqueous KCl solutions of various concentrations ($E_{\text{exc}} = 550 \text{ eV}$). b) PFY-XA spectra of aqueous H_2O and 1M, 2M, and 3M KCl solutions.

characteristics. Two absorption resonances labeled with “pre” and “main”, which correspond to the $4a_1$ and the $2b_2$ orbitals are visible. The emission spectrum shows the expected characteristic split $1b_1^{-1}$ emission present for excitation above the main-edge. For resonant excitation at the pre-edge, the two lines merge and appear as a single $1b_1^{-1}$ line. The $3a_1^{-1}$ and the $1b_2^{-1}$ emissions are also present. The slightly blue-shifted absorption onset is the most pronounced difference between the OK RIXS map of pure water and the map of the 3M KCl solution. Apart from this, no strong changes in the spectator region of the RIXS maps are visible. In the participant decay region further differences become obvious. For pure water the intensity of the Rayleigh line is strongly enhanced upon resonant excitation (A). With the addition of 3M KCl, this phenomenon is reduced. Furthermore, the extended vibrational progression, also visible for resonant excitation, is stronger for pure water and extends to much lower emission energies than for the salt solution. The third difference within the participant decay region becomes visible in the extended vibrational and dissociation region (B) [79, 158, 168], which is much more pronounced for pure water than for 3M KCl. These three differences will be discussed below.

Further changes in the OK emission spectrum of water become visible in the spectrum excited at about $E_{\text{exc}} = 550 \text{ eV}$ which is displayed in Fig. 4.3a. The spectra illustrated here (H_2O , KCl 1M, 2M, 3M, 4M, 6M) reveal a change in the spectral weight between the LE and HE component with increasing salt concentration. Furthermore, a slight increase in the intensity of the $1b_2^{-1}$ and the $3a_1^{-1}$ emission lines is observable, as well as a small feature arising at about $E_{\text{em}} = 528.4 \text{ eV}$. All features increase according to the salt concentration. The shifted absorption onset already observed in the RIXS maps is visible in Fig. 4.3b. What looks like a shift of the absorption edge in the RIXS map, turns out to be a change of the slope of the absorption onset, whereas the actual

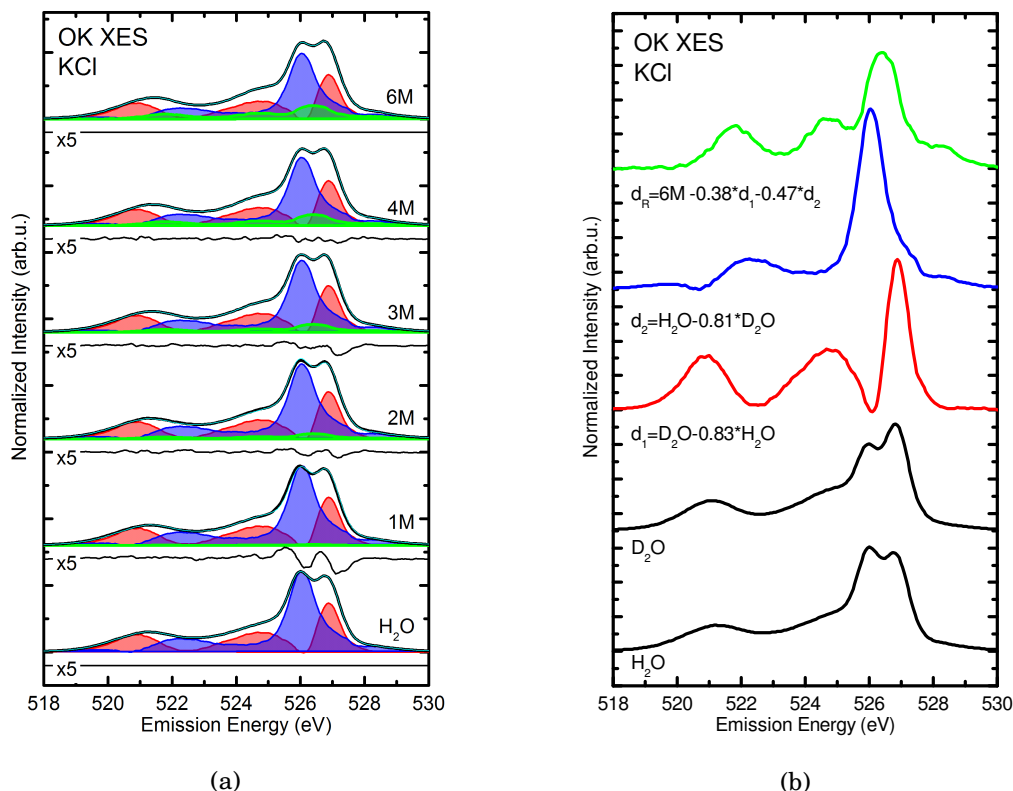


FIGURE 4.4. a) Fit of the non-resonantly excited OK-edge XE spectra ($E_{\text{exc}} = 550 \text{ eV}$) of H_2O and KCl solutions at various concentrations (black) with three spectral components (d_1 , d_2 , d_R) shown as red, blue, and green shaded areas. The resulting fit is shown in turquoise, the residual is shown below each set of spectra. b) OK-edge XE spectra ($E_{\text{exc}} = 550 \text{ eV}$) of H_2O and D_2O . d_1 and d_2 components derived from the differences of the H_2O and the D_2O spectra. The d_R component was derived from subtracting the two components (d_1 and d_2) from the KCl 6M spectrum.

energetic position of the $4a_1$ resonance stays constant.

Interestingly, by increasing the salt concentration, the XA spectra reveal more intensity in the main-, and post-edge which is in contrast to the published data [76]. This increase in intensity is an intrinsic effect of the fluorescence detection and is only indirectly related to the addition of KCl: Both, the potassium and the chlorine, are able to absorb photons with an energy of about 530 eV. Although the resonance energy of both absorption edges are much smaller (K $L_{2,3}$ -edge $\sim 300 \text{ eV}$, Cl $L_{2,3}$ -edge $\sim 270 \text{ eV}$) than the used photon energy a significant ratio of the photons gets absorbed by the salt. This decreases the attenuation length of the incident photons and reduces the self-absorption effect in the spectrum. Both effects, self absorption and molecular reorganization, are expected to show changes of similar amplitude which partly cancel each other out. Because of this, no further interpretation of the XA spectrum can be

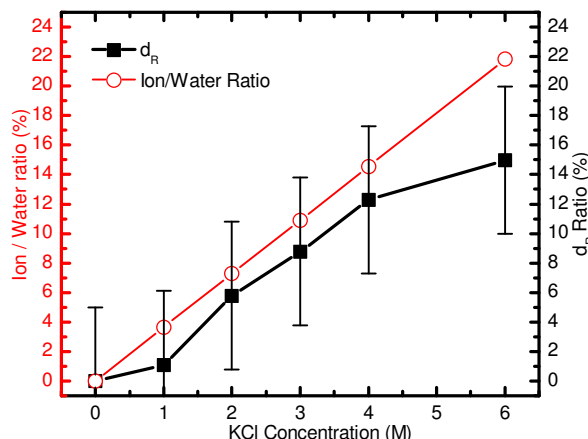


FIGURE 4.5. Ratio of the d_R component evaluated for the non-resonantly excited OK-edge XE spectra as a function of KCl concentration (black). Red circles indicate the ratio of salt ions to water molecules.

made.

Following the interpretation from Fuchs *et al.* [106], the splitting in the $1b_1^{-1}$ emission line is caused by the rapid dissociation of water molecules during the RIXS process. According to Fuchs *et al.*, the HE emission belongs to the emission of the $1b_1$ orbital of intact water molecules, while the LE emission belongs to the emission of the $1e_1$ orbital of OH^- which consists of the two degenerate π orbitals of OH^- .

In these studies it was shown that the two contributions (H_2O and OH^-) are two independent components which can be separated [106]. Since the two components show a strong isotope effect, the spectrum of D_2O and the spectrum of H_2O can be used to separate these two components [106] by creating weighted differences between the H_2O and the D_2O spectrum and vice versa, without creating negative intensity at all energies. The result are two spectral components, in the following named as $d_1 = \text{D}_2\text{O} - \text{H}_2\text{O}$ and $d_2 = \text{H}_2\text{O} - \text{D}_2\text{O}$.

However, a similar decomposition of the aqueous salt solutions into two components is not possible. For a sufficient description of the KCl spectra, a third component d_R has to be introduced. This third component is derived by subtracting the two components, d_1 and d_2 , from each salt spectrum. It is found that for each salt spectrum the additional component is very similar. To analyze this third component quantitatively, the d_R component is created from the 6M KCl spectrum and used together with the other two components d_1 and d_2 to fit the remaining spectra. The spectral weight of the three components is the only parameter.

The fit and the spectral components are displayed in Fig. 4.4a and Fig. 4.4b. Fig. 4.4b illustrates the non-resonantly excited XE spectrum of H_2O and D_2O . Above the spectra the three spectral components are displayed. $d_1 = \text{D}_2\text{O} - 0.83 \cdot \text{H}_2\text{O}$. $d_2 =$

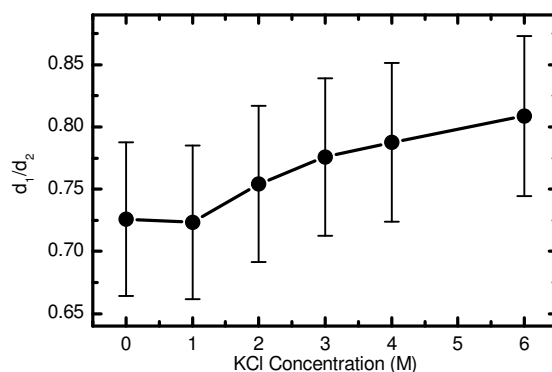


FIGURE 4.6. Fraction of the d_1 to d_2 component evaluated for the non-resonantly excited OK-edge XE spectra as a function of KCl concentration.

$\text{H}_2\text{O} - 0.81 \cdot \text{D}_2\text{O}$. $d_R = \text{KCl}_{6\text{M}} - 0.38 \cdot d_1 + 0.47 \cdot d_2$. For the definition of d_1 and d_2 , the spectra of H_2O and D_2O were area normalized. For the determination of d_R , d_1 and d_2 were also area normalized.

Fig. 4.4a illustrates the fits of the measurement series with the three components. The measurement is shown in black. Red, blue, and green areas indicate the three components d_1 , d_2 , and d_R . The sum of the components is illustrated in turquoise. Below each set of spectra, the residuum of the fit is displayed.

Even in Fig.4.4a a change in the relative weight of the three components can be observed. The quantitative changes are displayed in Fig. 4.5. By increasing the salt concentration, an increase in the d_R component of about 14% is visible. Fig. 4.5 also shows the ratio of salt ions to water molecules in percent. The d_R component is nicely following the ion to water ratio up to a concentration of 4M. For 6M the d_R component seems to saturate. This progression is not surprising. KCl has a solubility of 35.5 g in 100 g H_2O [88]. At a temperature of 20°C a maximal concentration of 4.6M can be reached. A concentration of 4.6M is comparable to an ion/water ratio of about 17%.

Based on the observed behavior, the d_R component can now be related to water molecules interacting with the salt ions. However, the extracted d_R ratio is notoriously smaller than the theoretically calculated ion/water ratio. This systematic underestimation of the d_R component indicates that the area of the d_R component still might be a bit too large. The error of this evaluation is mainly defined by the uncertainty in the subtraction of the d_1 and the d_2 components.

The d_R component shown in Fig. 4.4b shows four emission features. Besides the weak emission at about $E_{\text{em}}=528.4$ eV, the spectrum is very similar to the d_1 component, which is associated with intact molecules. These emission features can be assigned to the $3a_1$, $1b_2$, and $1b_1$ orbitals of intact water. By comparing the d_R component with the d_1 component, shifts in the energy position of the spectral features can be observed. The $1b_2^{-1}$ emission line is blue-shifted, while the $1b_1^{-1}$ line

is red-shifted. The position of the $3a_1^{-1}$ emission line is almost unchanged indicating that the molecular reorganization and the changes in the hydrogen bonding network mostly influence the $1b_2$ and the $1b_1$ orbitals, while the $3a_1$ orbital stays unaffected. Calculations from Gråsjö *et al.* [170] indicate a similar shift for the two orbitals and were related to the confinement of the water molecules by the ions. In accordance to photoemission experiments [171] and the calculation from Gråsjö *et al.* [170], the additional intensity observed at $E_{em}=528.4$ eV can be attributed to Cl 3p derived states created by the Cl^- ions.

In other words, the d_R component can be associated to intact water molecules interacting with the ions. Fig. 4.6 illustrates the d_1 to d_2 fraction as they were obtained by the fit. With increasing salt concentration, the d_1 to d_2 fraction increases slightly, which indicates that spectral weight is shifted from the dissociation related component (d_2) towards the d_1 component, which is related to intact water molecules.

In conclusion, KCl changes the electronic structure of the water molecules in the first hydration shell in a way that the core-excited state is less dissociative leading to a reduction of radiation induced dissociation. These findings are in good agreement with previously recorded XAS experiments of aqueous salt solutions [160, 161, 166].

This decomposition of the OK emission spectra is now repeated for RIXS spectra obtained at the main-edge and the pre-edge of water. Fig. 4.7 shows the OK RIXS spectra of the measurement series excited with $E_{exc}=536.0$ eV. Also at resonant excitation, the d_R^{main} component consists of three emission lines which have significant similarities to the emission features of the d_1^{main} component. The d_2^{main} component, similar to the non-resonantly excited d_2 component, consists of two components. However, the high emission line which can be associated with the $1e_1$ orbital of OH^- shows a high energy shoulder, which might be an artifact of the subtraction process neglecting the different vibrational envelopes in the spectra of H_2O and D_2O .

Similar to the non-resonantly excited spectra, the ratio of the d_R^{main} component increases with increasing salt concentration. The d_R^{main} ratio of the main-edge is depicted in Fig. 4.9. The shift in the spectral weight between d_1^{main} and d_2^{main} is also visible and is even more pronounced than the one in the non-resonant spectra.

Fig. 4.8 illustrates the OK RIXS spectra of the measurement series excited at $E_{exc}=534.2$ eV. Here the d_1^{pre} component still shows three emission lines but is largely suppressed. The d_2^{pre} component again consists of two components and is dominating the water spectrum. A ratio of d_1^{pre} to d_2^{pre} of about 1:2 is observed. The resulting d_R^{pre} component shows the three emission features. Although the OK RIXS spectrum of pure water recorded at the pre-edge is strongly dominated by the dissociation, with increasing salt concentration the d_R^{pre} component increases and the dissociation decreases.

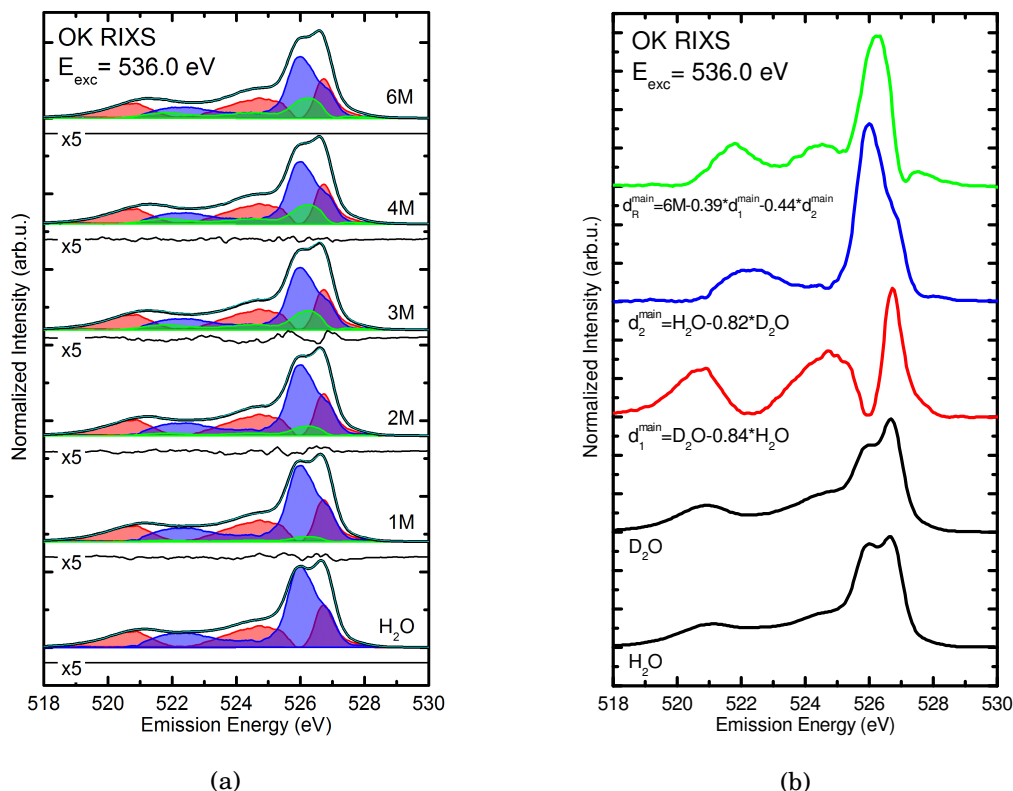


FIGURE 4.7. a) Fit of the OK RIXS spectra ($E_{\text{exc}} = 536.0 \text{ eV}$) of H₂O and KCl solutions at various concentrations (black) with three spectral components (d_1 , d_2 , d_R) shown as red, blue, and green shaded areas. The resulting fit is shown in turquoise, the residual is shown below each set of spectra. b) OK-edge XE spectra of H₂O and D₂O. d_1 and d_2 components derived from the differences of the H₂O and the D₂O spectra. The d_R component was derived from subtracting the two components (d_1 and d_2) from the KCl 6M spectrum.

Fig. 4.9 shows the ratio of the d_R components for all measurement series. The evaluated d_R components follow the same trend and fit very well to the ratio of ions to water molecules. All three components saturate for concentrations above 4M. The continuous development of the different d_R components indicates a consistent data evaluation.

However, the evaluation largely depends on the correct subtraction of the three spectral components d_1 , d_2 , and d_3 . For the experiment shown above, a component was labeled meaningful if the area was minimal without showing negative values. Although meaningful spectra, which have a larger area, could be created, they were ignored since it would influence the consistency within the data evaluation procedure. The shown errorbars were defined by estimating the error of the area of the three spectral components d_1 , d_2 , and d_R of $\pm 5\%$ of the total area.

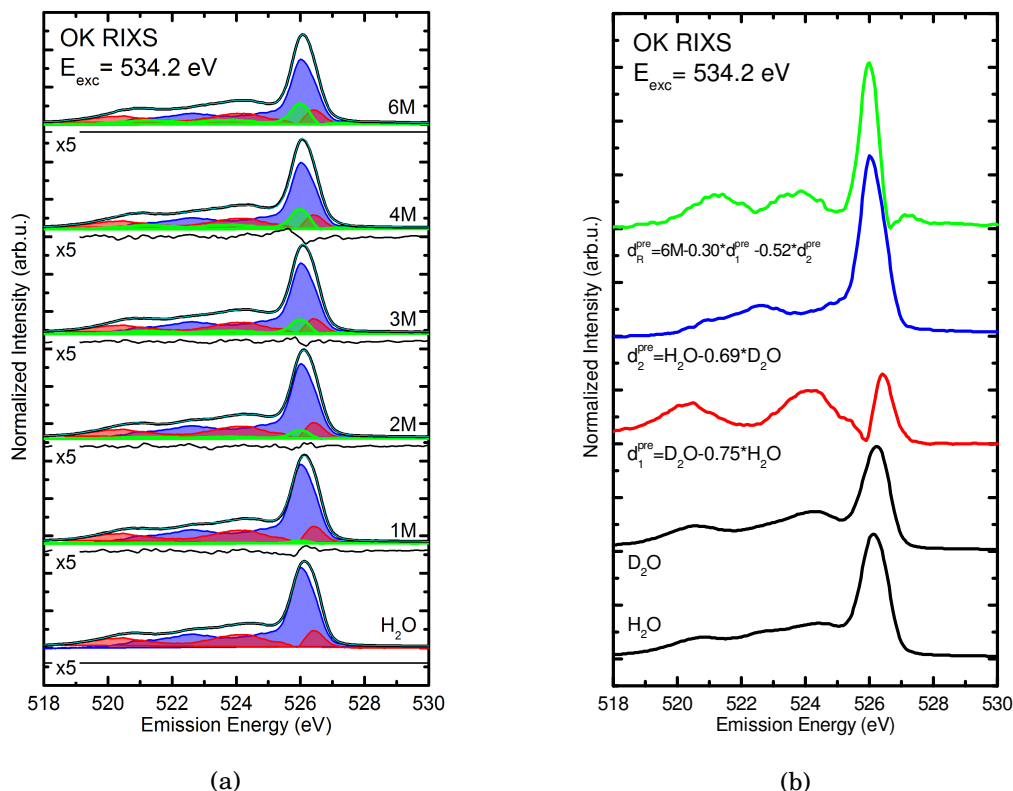


FIGURE 4.8. a) Fit of the OK RIXS spectra ($E_{\text{exc}} = 534.2 \text{ eV}$) of H_2O and KCl solutions at various concentrations (black) with three spectral components (d_1 , d_2 , d_R) shown as red, blue, and green shaded areas. The resulting fit is shown in turquoise, the residual is shown below each set of spectra. b) OK-edge XE spectra of H_2O and D_2O . d_1 and d_2 components derived from the differences of the H_2O and the D_2O spectra. The d_R component was derived from subtracting the two components (d_1 and d_2) from the KCl 6M spectrum.

As it can be observed in the OK RIXS maps displayed in Fig. 4.2, changes also occur in the participant decay region of the map. In the following, these changes are discussed in more detail. As already mentioned above, the participant decay region is associated with the radiative decay of the core excited electron. Fig. 4.10 displays the participant decay region of the spectra shown above in Fig. 4.7 and Fig. 4.8. All spectra were normalized to the measurement time and the photon flux of the beamline. No additional normalization was used to make changes in the absolute intensity visible.

The participant region of the pre-edge (Fig. 4.10a) exhibits two pronounced emission features marked with A and B. For emission energies lower than $E_{\text{em}}=532.0 \text{ eV}$, an increased background signal is visible. The participant region of the main-edge (Fig. 4.10b) shows a similar emission spectrum. Again two intense and narrow peaks are visible (A, B) and for emission energies below $E_{\text{em}}=532.0 \text{ eV}$ an increased back-

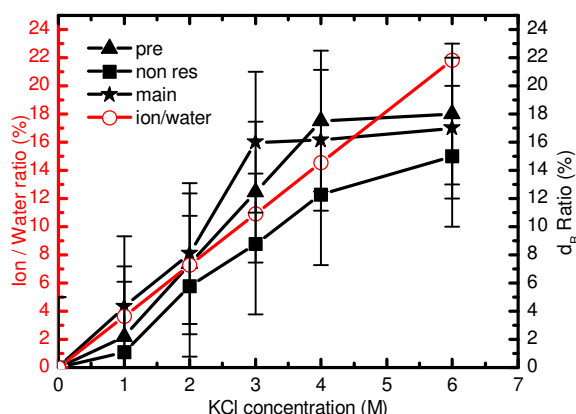


FIGURE 4.9. Ratio of the d_R component evaluated for the non-resonantly excited OK-edge XE spectra as a function of KCl concentration (square) as well as for the pre- (triangle) and main-edge (star). Red circles indicate the ratio of salt ions to water molecules.

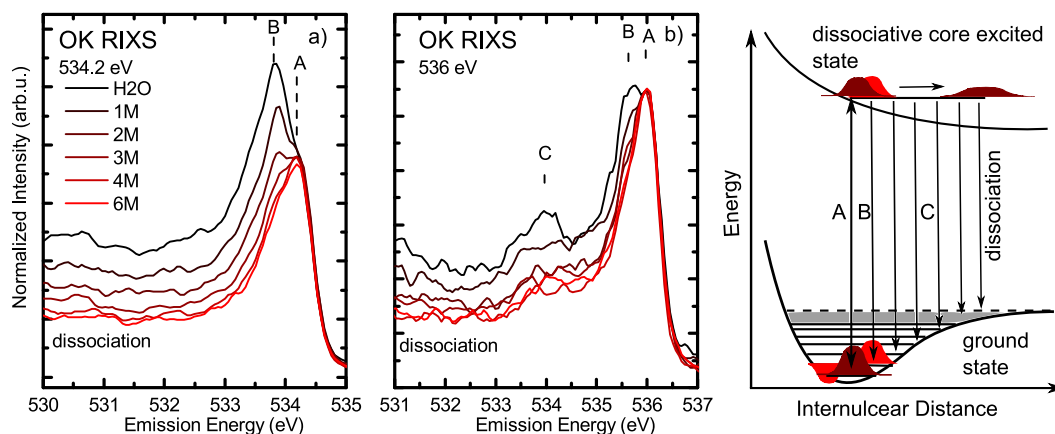


FIGURE 4.10. Participant decay spectra of pure liquid water and aqueous KCl solution (1-6M) resonantly excited at the pre- and main-edge. Schematic drawing of the nuclear dynamics occurring on the time scale of the RIXS process.

ground signal is observed. In contrast to the pre-edge, an additional emission feature can be found at about $E_{em}=534.0$ eV. The right panel in Fig. 4.10 shows a schematic illustration of the dynamics of a RIXS process with a dissociative core-excited state upon resonant excitation on the time scale of the X-ray emission process.

From literature it is known that the first core-excited state of liquid water has a strong dissociative character [99, 158]. This character could also be observed for the first core-excited state of gaseous water [154]. Subsequently, the schematic illustration models the reaction of the hydrogen proton which is illustrated as a wave package

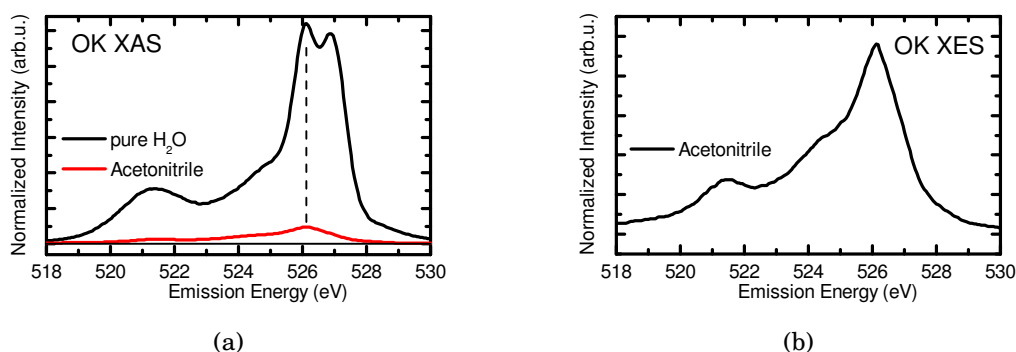


FIGURE 4.11. a) OK XE spectra of pure liquid water (black) behind a pristine window membrane and pure acetonitrile (red) measured after exposing the membrane to the X-ray radiation for approximately 3h, visualizing the oxidization of the window ($E_{\text{Exc}} = 550 \text{ eV}$). b) Enlarged OK XE spectrum of pure acetonitrile behind an oxidized window membrane shown in (a).

during the RIXS process.

For simplicity, the vibrational ground state is chosen as initial state ($1a_1 2a_1 1b_2 3a_1 1b_1$). Upon absorption of a photon, the H_2O molecule is excited into a core-excited state. In case of the pre-edge resonance, this state has the following configuration: $1a_1^{-1} 2a_1 1b_2 3a_1 1b_1 4a_1^1$. Note: the superscript indicates the occupation of an orbital deviating from the ground state. The core-excited state at the main-edge is given as: $1a_1^{-1} 2a_1 1b_2 3a_1 1b_1 2a_2^1$.

The subsequent emission process (decay) is now defined by the shape of the core-excited potential curve and the lifetime of this intermediate state ($\sim 3.6 \text{ fs}$ for O 1s) [172]. If the decay occurs before the wave package (hydrogen proton) has time to move, the system has the highest probability to decay back into the vibrational ground state (dark red), giving rise to feature A, which can be regarded as the elastic scattered peak. If the wave package has enough time to propagate, the probability of decaying into higher vibronic levels increases, giving rise to feature B. If the wave package moves far enough, the system dissociates before the emission takes place (indicated by the arrow ending in a continuum of levels above the dissociation level), giving rise to the increased background intensity observed for emission energies below 533 eV [79, 154].

In addition to the features explained above, the main-edge spectra show intensity at $E_{\text{em}}=534.0 \text{ eV}$ (C). This feature is also associated with the vibrational progression which is also true for feature B. But in contrast to feature B, the wave package has traveled quite far and thus the overlap with higher vibronic levels is larger creating this second emission feature. One also has to keep in mind that, although the energy difference between feature A and B fits very nicely to the energy of the OH stretch mode of liquid water ($\sim 0.4 \text{ eV}$) [173], feature B and C are most likely the result of

the envelope function of the Franck-Condon like vibrational progression, as it can be observed for O₂ [99] and for ethylene [174].

The spectral weight of the background and the intensity in the features B and C are thus an indicator for the speed of the wave package in the core-excited state.

In this context the changes observed in the intensity of feature B and C, as well as the background occurring with increasing salt concentration, have a physical meaning. It is suggested that the ions change the potential curve of the core-excited state of the water molecules in a way that the dissociation process is slowed down or even hindered. This interpretation is in accordance to the findings from the spectator emission data.

Since the changes evaluated in the X-ray spectra of pure liquid water and aqueous KCl solutions are very small, spectral changes occurring due to a degradation of the window membrane have to be ruled out. Fig. 4.11a shows the OK XE spectrum of pure liquid water with a pristine window and an “OK XE spectrum” of acetonitrile recorded after the entire measurement series including all RIXS maps (KCl 1M, 2M not shown). The spectra are normalized to the measurement time and the photon flux. Acetonitrile is an oxygen free liquid. Hence, the graph illustrates the accumulated “contamination” (oxidization) of the window membrane material. Fig. 4.11b shows a detailed view of the “oxidization” spectrum. The spectrum shows large similarities to the spectrum of Si₂O found in literature [11] (SI of [76]) and has obvious differences to the d_R extracted above, indicating that the observed effect is not the result of an oxidization of the window membrane.

4.3 Summary

In Summary, the OK RIXS data investigated above show a consistent picture. Through addition of KCl into aqueous water, the hydrogen bonding network of the water molecules gets perturbed. An extensive reorganization of the water molecules can be observed. This reorganization of the hydrogen bonding network visualizes in two different emission channels. The participant decay channel shows large changes in the vibrational progression of the water molecules as well as a pronounced suppression of the dissociation related intensity background. The phenomenon that the introduction of ions into the water network reduces the dissociative character of the water molecules was also observed in the spectator emission. Besides the reduction of the dissociation, also a direct influence of the ions on the electronic structure of the water molecules can be observed. The derived third spectral component (d_R) associated with the water molecules which are influenced by the KCl ions shows a spectral signature similar to the signature of intact water molecules. This again indicates that the salt ions cause a molecular reorganization of the water molecules around the ions. Moreover, the

energetic positions of the spectral features within the d_R component indicated that the influenced H₂O molecules have a significantly different electronic structure.

With the study presented above, a distinct signature associated with ion solvation was obtained. By investigating a larger variety of salt solutions, it might be possible to distinguish between effects caused by cations and anions on the hydrogen bonding network of liquid water. This study opens up opportunities to study the more complex solvation mechanisms of biomolecules in salt solutions, also known as Hofmeister effect, as well as solvation issues in electrochemical devices.

CONCLUDING DISCUSSION

The focus of this thesis is on the investigation of the electronic structure of biological molecules and salts in aqueous solution. Besides gaining fundamental knowledge about the characteristic features in the X-ray spectra of organic molecules in aqueous solutions, a building block approach was established which allows the qualitative investigation of the, often complex, X-ray emission spectra of these systems. Within the scope of this thesis, the applicability and the possibilities that come with this building block approach were demonstrated on several solid state molecular systems as well as aqueous solutions of biological molecules and salts.

A Building Block Principle for XES and RIXS

In the first part of this thesis the X-ray emission spectra of the 20 proteinogenic amino acids in solid phase at all emission edges are presented. This library of spectra was used to evaluate the spectral fingerprint of the functional groups, most prominently the protonated α -amino group (NH_3^+) and the deprotonated α -carboxylic group (COO^-). Both fingerprints were generated as an averaged spectrum of NK emission and OK emission spectra of amino acids containing only one nitrogen atom in the α -amino group and the two oxygen atoms in the α -carboxylic group, respectively.

According to the building block principle, the NK XE spectra of amino acids with additional nitrogen atoms containing functional groups within the side-chains consist of a superposition of an α -amino fingerprint, and a signature of the side-chain. To evaluate the fingerprints of the side-chain's functional groups, the NH_3^+ fingerprint was subtracted from the NK XE spectra, weighted according to the number of nitrogen atoms per functional group. This can be done under the assumption that the total cross

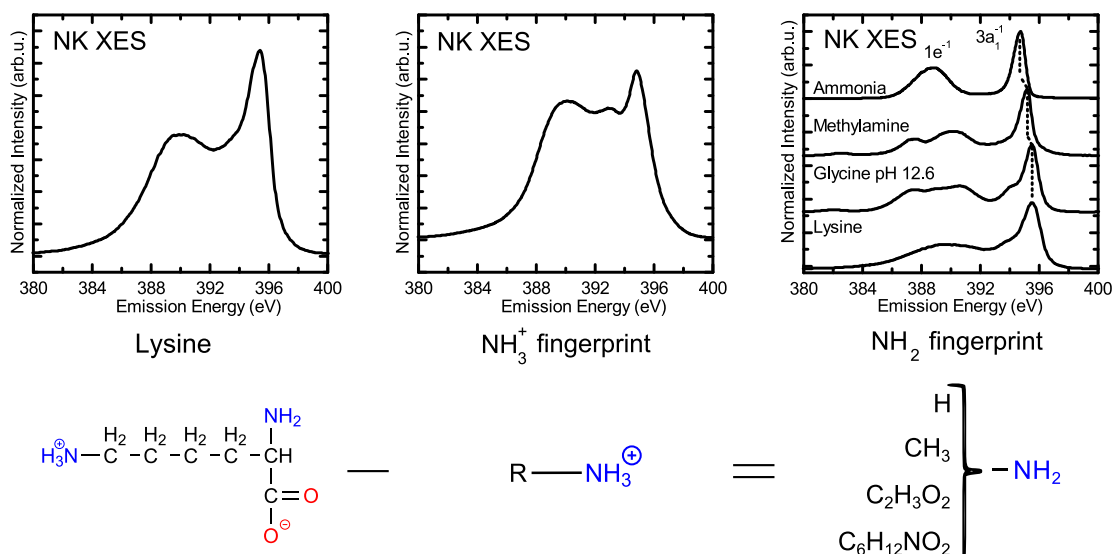


FIGURE 5.1. The building block approach applied to the NK XE spectrum of lysine. Subtracting the NH_3^+ fingerprint results in a NH_2 spectrum which is comparable to the NK XE spectra of smaller reference molecules. The ammonia spectrum was adopted from [77]. The glycine spectrum adopted from [65].

section is equal for all (chemically different) nitrogen atoms. This assumption is a first approximation and slight variations from this ratio might occur. This subtraction procedure was repeated for the OK XE spectra. By using the building block model, spectral fingerprints of all functional groups of the 20 proteinogenic amino acids in solid state could be proposed (see Table 3.1). The local character of XES and the applicability of the building block approach suggest that the XE spectrum of a functional group should show large similarities which are independent of the size of the molecule they are attached to.

Based on this, the NK XES spectral fingerprints of the side-chains of lysine and histidine were compared to the NK XE spectra of smaller molecules—so called reference molecules—hosting the same functional groups. In the case of lysine, the size of the reference molecule could be reduced dramatically. Comparing the NK XE spectra of the side-chain of lysine, aqueous glycine at pH 12, gaseous methionine, and aqueous ammonia, it was concluded that even the spectrum of ammonia shows a significant agreement with the lysine spectrum (see Fig. 5.1). For histidine, the size of the reference molecules could only be reduced to a certain amount. The ring structure is strongly influencing the electronic structure surrounding the nitrogen atoms. In this case, the entire ring structure had to be used as a suitable reference molecule.

The fact, that the spectral fingerprint of a functional group of a much larger molecule shows large similarities to the spectral fingerprint of a suitable reference molecule implies that the electronic structure of both have to be very similar too. However, due to the largely reduced size of the reference molecule, the electronic structures of both molecules cannot be very similar at all, in fact at some point the electronic structure has to be very different. Nevertheless, as demonstrated above, experimentally a building block model seems to be applicable. The key point why a spectral fingerprint of a functional group attached to a rather big molecule can be compared with the spectral fingerprint of a simple reference molecule, which represents the bare functional group lies in the local probing character of XES, XAS, and RIXS. The involvement of core electrons induces not only the element selectivity, but also the local probing character. Which means, that the spectral fingerprint obtained by XES and RIXS, is mainly determined by the electronic structure of the orbitals, which have a spacial overlap with the core level participating in the XES and RIXS process and therefore reflects only a very local part of the molecular orbitals.

Furthermore, over the past decades a number of models were developed to describe the wave function of a molecular orbital. Hereby the molecular orbital theory (MO) and the Hartree-Fock method are both wave function based methods, which approximate a molecular orbital by a *linear combination of atomic orbitals* (LCAO). By keeping in mind that the valence orbitals of a molecule can be described by a linear combination of atomic orbitals the applicability of the building block model becomes more obvious. The atomic orbitals of a single functional group are “mixed” into the valence orbital structure of a molecule and their influence are largest for valence orbitals which are mainly localized around the particular functional group. The XES and RIXS process are both, due to the local probing character, particularly sensitive to exactly these valence orbitals, which have a significant overlap with the core level of the excitation site (functional group). In other words, the local partial density of states, probed by XES and RIXS is highly influenced by the atomic orbitals of the excitation site and the neighboring atoms independently of the size of the molecule. Since, if all nearest neighbors of the excited atom are included, the functional group and the reference molecule consist of the same atomic orbitals, the building block model can be applied.

In case of imidazole the entire ring structure had to be used as a reference molecule. The reason why the building block had to be increased compared to a functional group like the amino group can also be ascribed to the localization of the molecular orbitals. In a ring structure, the molecular orbitals are, due to the high symmetry more delocalized over the entire molecule, therefore more atoms are contributing to these molecular orbitals and the fraction of a single atomic orbital is reduced, which is also reflected in the spectral fingerprint.

In conclusion, reference molecules can be named suitable, if the orbital structure

and thus the linear combination of atomic orbitals in the vicinity of the excitation site of functional group and building block are similar.

Building Block Principle Applied to Proline and Pyrrolidine

The amino acid proline has only one α -amino group, but its NK XE spectrum differs strongly from the regular α -amino spectrum (NH_3^+ fingerprint) observed for other amino acids. The side-chain of proline is back connected to the α -amino group, which creates a saturated heterocyclic ring structure. Inspired from the findings on the side-chain of histidine, the NK XE spectral fingerprint of proline should also be largely influenced by the ring structure, which means a suitable reference molecule has to describe the entire ring. Furthermore, compared to histidine, proline hosts only a single nitrogen atom which makes the NK XE spectrum much easier. These facts make proline an interesting candidate for further studies validating the building block approach on a more complex molecule showing a delocalized electronic structure. In this work proline was investigated in solid phase as well as in aqueous solutions of different pH-values.

To investigate the electronic structure of zwitterionic proline, RIXS maps of the OK-, CK- and NK-edge of solid proline were measured and evaluated in detail. Hereby, the OK RIXS map shows a strong resonance at $E_{\text{exc}}=532.6$ eV, which has a significantly different XE signature than the XE spectra at higher excitation energies. The NK-edge shows a weak resonance at $E_{\text{exc}}=398.8$ eV which is caused by small traces of nitrogen containing contamination. Apart from this, the NK RIXS map shows no significant resonant effects. On the contrast, the CK RIXS map shows many resonances. Following the investigation of the CK RIXS map of cysteine [83], single emission lines can be assigned to localized orbitals without the help of theoretical calculations.

Due to the high solubility of proline in water, solutions with a high concentration and therefore a high signal to noise ratio can be achieved. This makes proline a perfect candidate for investigations of amino acids in aqueous environment. At neutral pH-value, the chemical structure (bonding configuration) of the solid and liquid phase is identical. By changing the pH-value, the amino group and the carboxylic group can be protonated or deprotonated, respectively. These changes have a prominent effect on the XE spectra of the molecule's functional groups.

Although the sample volume within the liquid cell is replenished with a very high frequency, the decomposition of the proline molecule could not be prevented and an agglomeration of molecular fragments at the window membrane of the measurement setup was observed. Therefore, with increasing measurement time, the proline spectra became superimposed by the spectral signature of molecular fragments adsorbed at the membrane (see Fig. 3.31). This effect was stronger for the nitrogen K-edge than

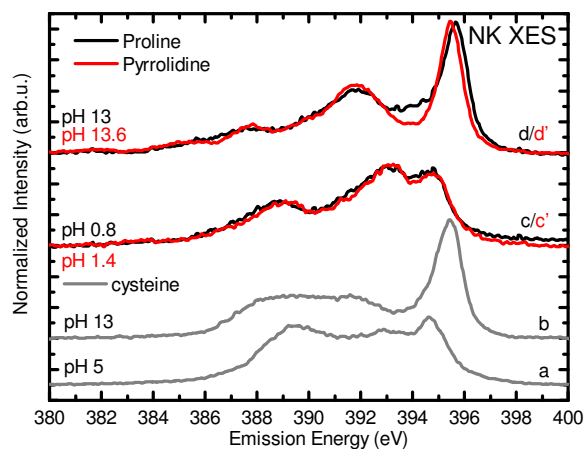


FIGURE 5.2. Illustrating the influence of the ring structure on the electronic structure of the α -amino group. NK XE spectra of proline (black) and pyrrolidine (red) with protonated (c) and deprotonated (d) amino group. NK XE spectra of cysteine are shown as comparison (a, b).

for the oxygen K-edge. As a consequence the OK RIXS maps could be recorded without any contamination signature, while the NK RIXS maps are highly influenced by the contamination. However, the contamination was limited to the neutral and high pH solutions. For low pH solutions ($\text{pH} < 3$), no contamination of the membrane was observed. The reason for this different behavior might be due to the high concentration of hydronium ions (H_3O^+) within the solution which possibly interact with the molecular fragments and prevent them from agglomerating at the window membrane. By slightly lowering the pH-value from neutral ($\text{pH} 7$) to $\text{pH} 3.5$, the agglomeration process could be slowed down and the exposure time per membrane spot could be increased. At low pH-values, the contamination reaction was again slower than for the neutral pH-value solution. Therefore, non-resonantly excited XE spectra of intact proline could be achieved, but for the NK RIXS maps an agglomeration of molecules on the membrane could not be fully prevented.

These studies demonstrate that for experimental setups which separate the liquid from the vacuum by a thin membrane, agglomeration of molecular fragments on the membrane can have a large effect on the spectra and have to be taken into account. By a suitable optimization of the experimental parameters, the influence of this effect can be minimized.

The non-resonantly excited NK XE spectra of proline at different pH-values are very different from the NK XE spectra of other amino acids and also from the NH_3^+ fingerprint. The comparison to pyrrolidine showed large similarities. Pyrrolidine has a heterocyclic ring structure and hence can be seen as a proline molecule without a carboxylic group. This comparison shows that the electronic structure of the nitrogen

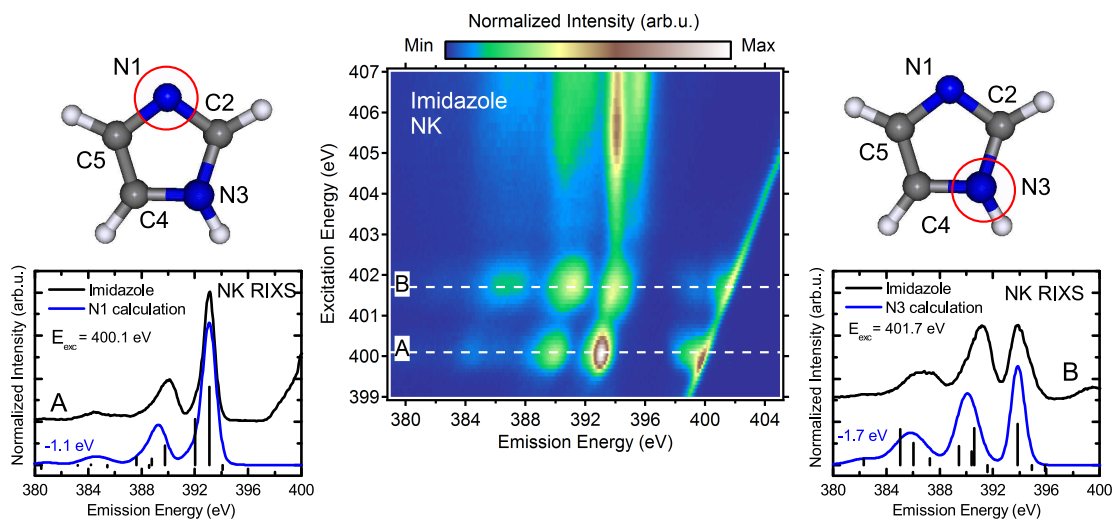


FIGURE 5.3. Upon resonant excitation, the X-ray emission of the two chemically non-equivalent nitrogen atoms can be separated. Left: emission of the N1 nitrogen. Right: emission of the N3 nitrogen.

atom is highly influenced by the ring structure (see Fig. 5.2). The NK RIXS maps of pyrrolidine show the same but weakened agglomeration signatures as for proline. The contamination was not prevented entirely but reduced such that both configurations could be measured. In addition to the described experiment, XE and XA spectra of pyrrolidine were calculated using the StoBe-deMon DFT package [58]. With the calculation it was possible to assign single orbitals to single emission and absorption lines, respectively.

Site selective Investigation of Histidine and Imidazole

Histidine was chosen because of its biological relevance, e.g. as oxygen binding partner in the protein hemoglobin [123]. Furthermore, the bare side-chain of histidine (imidazole) is of particular significance to the entire material class of ionic liquids [124].

In aqueous solution, four chemical configurations of histidine can be achieved by adjusting the pH-value. Using the building block approach, the NK XE spectra of all four chemical configurations can be modeled with the NK XE spectra of imidazole and cysteine at different pH-values. The excellent agreement between the measured spectra and the modeled spectra verifies the building block approach and shows that molecular structures with delocalized electronic states have to be treated as a unit.

This method was also extended to resonantly excited spectra at the OK-edge which were compared to OK RIXS spectra of acetic acid.

In the NK XE spectra of histidine also an agglomeration of molecular fragments at the membrane was observed, which did not allow to record NK RIXS maps of its four chemical configurations. However, the investigation of the much smaller molecule imidazole as a reference, made it possible to record NK RIXS spectra without contributions from agglomerated fragments. These NK RIXS maps of imidazole represent the functional group of histidine and with the help of the building block model conclusions about histidine can be drawn.

Besides strong changes in the NK XE spectra of imidazole due to protonation of the N1 nitrogen atom (see Fig. 5.3), a dynamical signature within the spectrum could be observed. The NK XE spectrum of the protonated imidazolium ion shows a strong signature, which can be explained by rapid proton movements on the timescale of the core hole lifetime. This dynamical component was identified by a comparison of the experimental with the theoretical spectra. Furthermore, the calculations allow the assignment of single emission and absorption features to single molecular orbitals. In the case of imidazole, resonant excitation allows an isolated excitation of the two chemically different nitrogen atoms and thus the separation of the two emission signatures (see Fig. 5.3). The spatial localization of the two nitrogen atoms and their emission characteristics give information about the spatial distribution (nodal planes and localization) of the electron density of selected orbitals.

Upon resonant excitation of both imidazole configurations, strong resonant effects in the spectra are observed. These effects manifest themselves as energetic shifts as well as changes in the intensity of the transitions, which are caused by the interaction of the core-excited electron with the occupied molecular orbitals during the intermediate state. Due to these resonant effects, the resonantly excited RIXS spectra and the non-resonantly excited XE spectra show significant differences in peak position and intensities.

By comparing the XE spectrum with the RIXS spectra, it is possible to quantify the energetic shifts of the single transmission lines. As it was observed for the NK RIXS spectrum of imidazolium and the CK RIXS spectra of imidazolium and imidazole, the intensity of the single transition within the RIXS spectrum can be very different from the non-resonantly excited XE spectrum. The observed differences can be very dramatic and an assignment to a single effect was in the presented case not possible. However, a combination of the following three effects might create the observed behavior. Firstly, in the two-step picture of the RIXS process also the excitation step depends on dipole selection rules [132]. Secondly, in randomly oriented samples (liquids), the intermediate state introduces an orientation-dependent selection of molecules, which results in a polarization anisotropy of the emitted photons. Hence, the

emission varies in dependence of the measurement geometry. Thirdly, since the RIXS process can also be described as a single step scattering process, the interference of different decay channels can also change the intensity of the transition. The described experiments demonstrate the applicability of the building block approach and the possibilities to quantitatively analyze molecular systems in aqueous solution.

Impact of KCl on the Hydrogen Bonding Network of liquid Water

To shed light on the secrets of the Hofmeister effect [175–182], the influence of salt ions on the hydrogen bonding network of liquid water was investigated in the third part of this thesis. Besides changes in the emission spectra of water (XES and RIXS), which were analyzed by decomposing the spectrum into the characteristic spectral signatures of intact water molecules, dissociated water molecules, and water molecules, which are in direct vicinity of the salt ion, also spectral signatures of dynamical processes were investigated.

The decomposition is schematically shown in Fig. 5.4. Upon the addition of potassium chloride a decrease in intensity of the vibronic loss structure at the Rayleigh line of the water spectra can be observed. This comes along with a decrease of spectral

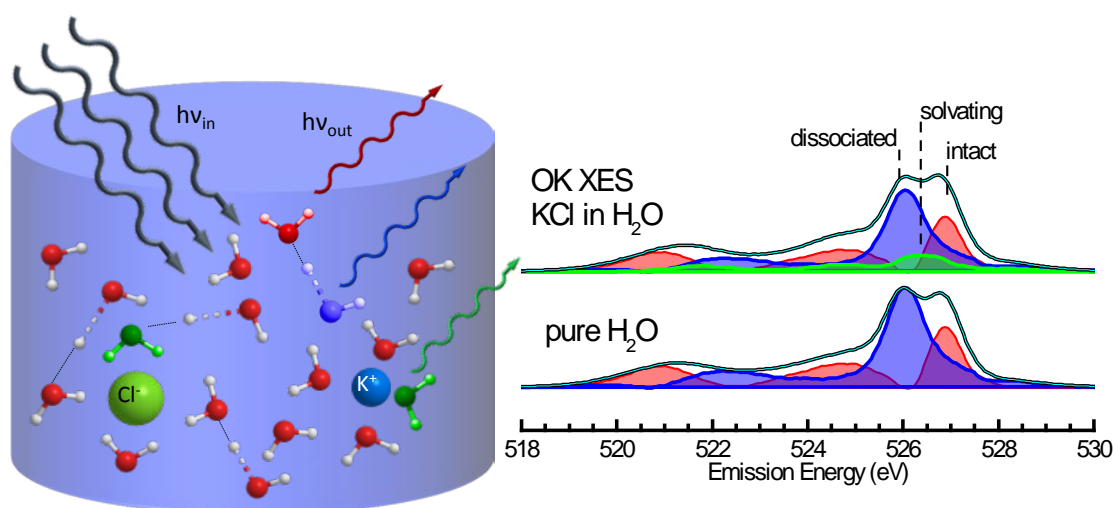


FIGURE 5.4. Illustration of the influence of the KCl ions on the hydrogen bonding network of liquid water and its impact on the OK XE spectrum. Spectral components of the different water “species” in the aqueous KCl solution are highlighted.

features which are assigned to the dissociation of a proton on the timescale of the core hole lifetime. Both, the changes in the vibronic progression and the reduced dissociation, are interpreted as the result of changes in the potential landscape of the water molecules. This might be due to the weakening or even breaking of hydrogen bonds caused by the reorganization of the water molecules around the salt ions.

Concluding Remarks

The analysis of resonantly and non-resonantly excited X-ray emission spectra allows the separation of spectral fingerprints of either complex molecules (e.g., histidine) or of complex mixtures (e.g., aqueous salt solutions) which then can be interpreted by comparing them to spectral fingerprints of suitable reference molecules or by using theoretical calculations. This work sets the foundation for the investigation of more complex molecules, e.g. dipeptides or proteins. Many questions about the Hofmeister series are still open and the number of potential sample systems is large.

XES, XAS, and RIXS have proven to be a powerful tool for the investigation of the electronic structure of liquid samples. Although this thesis was limited to the investigation of biological molecules and salt solutions a large number of systems can be studied by this approach. For example, by designing new experimental setups which are electrically isolated, this method can be used for the investigation of electrochemical reactions [183]. Other setups are able to extend this methods to catalytic reactions of gases at solid interfaces [9, 184].

BIBLIOGRAPHY

- [1] Zubavichus, Y., Fuchs, O., Weinhardt, L., Heske, C., Umbach, E., Jonathan D. Denlinger, and Grunze, M. “Soft X-Ray-Induced Decomposition of Amino Acids: An XPS, Mass Spectrometry, and NEXAFS Study”. *RADIATION RESEARCH* **161** (2004), pp. 346–358.
- [2] X. Liu, W. Yang, and Z. Liu. “Recent Progress on Synchrotron-Based In-Situ Soft X-ray Spectroscopy for Energy Materials”. en. *Advanced Materials* **26** (2014), pp. 7710–7729.
- [3] H. Siegbahn and K. Siegbahn. “ESCA applied to liquids”. *Journal of Electron Spectroscopy and Related Phenomena* **2** (1973), pp. 319–325.
- [4] H. Siegbahn. “Electron spectroscopy for chemical analysis of liquids and solutions”. *The Journal of Physical Chemistry* **89** (1985), pp. 897–909.
- [5] B. Winter. “Liquid microjet for photoelectron spectroscopy”. *Nuclear Instruments and Methods in Physics Research Section A: Accelerators, Spectrometers, Detectors and Associated Equipment* **601** (2009), pp. 139–150.
- [6] M. Faubel, S. Schlemmer, and J. P. Toennies. “A molecular beam study of the evaporation of water from a liquid jet”. *Zeitschrift für Physik D Atoms, Molecules and Clusters* **10** (1988), pp. 269–277.
- [7] D. E. Starr, E. K. Wong, D. R. Worsnop, K. R. Wilson, and H. Bluhm. “A combined droplet train and ambient pressure photoemission spectrometer for the investigation of liquid/vapor interfaces”. *Physical Chemistry Chemical Physics* **10** (2008), p. 3093.
- [8] K. R. Wilson, B. S. Rude, T. Catalano, R. D. Schaller, J. G. Tobin, D. T. Co, and R. J. Saykally. “X-ray Spectroscopy of Liquid Water Microjets”. *J. Phys. Chem. B* **105** (2001), pp. 3346–3349.
- [9] A. Benkert, M. Blum, F. Meyer, R. G. Wilks, W. Yang, M. Bär, F. Reinert, C. Heske, and L. Weinhardt. “Setup for in situ investigation of gases and gas/solid

- interfaces by soft x-ray emission and absorption spectroscopy”. *Review of Scientific Instruments* **85** (2014), p. 015119.
- [10] M. Blum, L. Weinhardt, O. Fuchs, M. Bär, Y. Zhang, M. Weigand, S. Krause, S. Pookpanratana, T. Hofmann, W. Yang, J. D. Denlinger, E. Umbach, and C. Heske. “Solid and liquid spectroscopic analysis (SALSA) a soft x-ray spectroscopy endstation with a novel flow-through liquid cell”. *Review of Scientific Instruments* **80** (2009), p. 123102.
- [11] O. Fuchs, F. Maier, L. Weinhardt, M. Weigand, M. Blum, M. Zharnikov, J. Denlinger, M. Grunze, C. Heske, and E. Umbach. “A liquid flow cell to study the electronic structure of liquids with soft X-rays”. *Nuclear Instruments and Methods in Physics Research Section A: Accelerators, Spectrometers, Detectors and Associated Equipment* **585** (2008), pp. 172–177.
- [12] A. J. Achkar, T. Z. Regier, H. Wadati, Y.-J. Kim, H. Zhang, and D. G. Hawthorn. “Bulk sensitive X-ray absorption spectroscopy free of self-absorption effects”. *Physical Review B* **83** (2011), p. 081106.
- [13] L. Weinhardt, M. Blum, O. Fuchs, A. Benkert, F. Meyer, M. Bär, J. Denlinger, W. Yang, F. Reinert, and C. Heske. “RIXS investigations of liquids, solutions, and liquid/solid interfaces”. *Journal of Electron Spectroscopy and Related Phenomena* **188** (2013), pp. 111–120.
- [14] J.-E. Rubensson, F. Hennies, and A. Pietzsch. “High-resolution resonant inelastic soft X-ray scattering applied to liquids”. *Journal of Electron Spectroscopy and Related Phenomena*. *Progress in Resonant Inelastic X-Ray Scattering* **188** (2013), pp. 79–83.
- [15] J. Bergengren. “Über die Röntgenabsorption des Phosphors”. *Zeitschrift für Physik* **3** (1920), pp. 247–249.
- [16] C. J. Sparks. “Inelastic Resonance Emission of X Rays: Anomalous Scattering Associated with Anomalous Dispersion”. *Physical Review Letters* **33** (1974), pp. 262–265.
- [17] P. Eisenberger, P. M. Platzman, and H. Winick. “Resonant X-ray Raman scattering studies using synchrotron radiation”. *Physical Review B* **13** (1976), pp. 2377–2380.

-
- [18] J. Nordgren and J.-E. Rubensson. “Resonant soft X-ray emission for studies of molecules and solids”. *Journal of Electron Spectroscopy and Related Phenomena* **188** (2013), pp. 3–9.
- [19] J. P. Rueff and A. Shukla. “A RIXS cookbook: Five recipes for successful RIXS applications”. *Journal of Electron Spectroscopy and Related Phenomena. Progress in Resonant Inelastic X-Ray Scattering* **188** (2013), pp. 10–16.
- [20] F. Gel’mukhanov and H. Ågren. “X-ray resonant scattering involving dissociative states”. *Physical Review A* **54** (1996), pp. 379–393.
- [21] P. A. M. Dirac. “The Quantum Theory of the Emission and Absorption of Radiation”. *Proceedings of the Royal Society of London. Series A* **114** (1927), pp. 243–265.
- [22] E. Fermi. *Nuclear Physics*. University of Chicago Press, 1950.
- [23] K. Siegbahn, L. Werme, B. Grennberg, J. Nordgren, and C. Nordling. “The carbon X-ray spectrum of gaseous CO”. *Physics Letters A* **41** (1972), pp. 111–112.
- [24] R. C. Ehlert and R. A. Mattson. “X-Ray Emission Spectra from Chlorinated Methanes and Fluorochloromethanes”. *The Journal of Chemical Physics* **48** (1968), pp. 5471–5475.
- [25] R. E. LaVilla. “ K_{α} Emission Spectrum of Gaseous N_2 ”. *The Journal of Chemical Physics* **56** (1972), pp. 2345–2349.
- [26] D. T. Attwood. *Soft x-rays and extreme ultraviolet radiation*. 1. ed. Cambridge Univ. Press, 2000.
- [27] M. O. Krause. “Atomic radiative and radiationless yields for K and L shells”. *Journal of Physical and Chemical Reference Data* **8** (1979), pp. 307–327.
- [28] J. Stöhr. *NEXAFS spectroscopy*. 1. ed., corr. 2. print. Springer series in surface sciences ; 25. Berlin [u.a.]: Springer, 2003. XV, 403 S.
- [29] F. Gel’mukhanov and H. Ågren. “Resonant X-ray Raman scattering”. *Physics Reports* **312** (1999), pp. 87–330.
- [30] J. J. Sakurai. *Advanced quantum mechanics*. 1. ed. Addison-Wesley series in advanced physics. Reading, Mass.: Addison-Wesley, 1967.

- [31] H. A. Kramers and W. Heisenberg. “Über die Streuung von Strahlung durch Atome”. *Zeitschrift für Physik* **31** (1925), pp. 681–708.
- [32] J.-E. Rubensson. “RIXS dynamics for beginners”. *Journal of Electron Spectroscopy and Related Phenomena* **110-111** (2000), pp. 135–151.
- [33] H. C. Haken H. und Wolf. *Molekülphysik und Quantenchemie*. 1. ed. Springer-Lehrbuch. Berlin [u.a.]: Springer, 1992.
- [34] P. Hohenberg and W. Kohn. “Inhomogeneous Electron Gas”. *Physical Review* **136** (1964), B864–B871.
- [35] W. Kohn. “Nobel Lecture: Electronic structure of matter-wave functions and density functionals”. *Reviews of Modern Physics* **71** (1999), pp. 1253–1266.
- [36] R. M. Dreizler. *Density functional theory*. 1. ed. Berlin [u.a.]: Springer, 1990.
- [37] R. G. Parr. *Density functional theory of atoms and molecules*. 1. iss. as paperback. The international series of monographs on chemistry ; 16. New York: Oxford Univ. Press, 1994.
- [38] T. Ziegler. “Approximate density functional theory as a practical tool in molecular energetics and dynamics”. *Chemical Reviews* **91** (1991), pp. 651–667.
- [39] R. G. Parr. “Density Functional Theory”. *Annual Review of Physical Chemistry* **34** (1983), pp. 631–656.
- [40] E. Fermi. “Un metodo statistico per la determinazione di alcune proprietà dell’atome”. *Atti Accad. Naz. Lincei, Cl. Sci. Fis. Mat. Nat. Rend.* **6** (1927), pp. 602–607.
- [41] Y. Wang and R. G. Parr. “Construction of exact Kohn-Sham orbitals from a given electron density”. *Physical Review A* **47** (1993), R1591–R1593.
- [42] C.-O. Almbladh and U. von Barth. “Exact results for the charge and spin densities, exchange-correlation potentials, and density-functional eigenvalues”. *Physical Review B* **31** (1985), pp. 3231–3244.
- [43] W. Kohn. “Density Functional and Density Matrix Method Scaling Linearly with the Number of Atoms”. *Physical Review Letters* **76** (1996), pp. 3168–3171.
- [44] W. Kohn and L. J. Sham. “Self-Consistent Equations Including Exchange and Correlation Effects”. *Physical Review* **140** (1965), A1133–A1138.

- [45] E. Wigner. “Effects of the electron interaction on the energy levels of electrons in metals”. *Transactions of the Faraday Society* **34** (1938), pp. 678–685.
- [46] D. Ceperley. “Ground state of the fermion one-component plasma: A Monte Carlo study in two and three dimensions”. *The Journal of Physical Review B* **18** (1978), p. 3126.
- [47] J. P. Perdew and A. Zunger. “Self-interaction correction to density-functional approximations for many-electron systems”. *Physical Review B* **23** (1981), pp. 5048–5079.
- [48] J. P. Perdew and Y. Wang. “Accurate and simple analytic representation of the electron-gas correlation energy”. *Physical Review B* **45** (1992), pp. 13244–13249.
- [49] S. H. Vosko, L. Wilk, and M. Nusair. “Accurate spin-dependent electron liquid correlation energies for local spin density calculations: a critical analysis”. *Canadian Journal of Physics* **58** (1980), pp. 1200–1211.
- [50] J. P. Perdew, K. Burke, and M. Ernzerhof. “Generalized Gradient Approximation Made Simple”. *Physical Review Letters* **77** (1996), pp. 3865–3868.
- [51] A. D. Becke. “Density-functional exchange-energy approximation with correct asymptotic behavior”. *Physical Review A* **38** (1988), pp. 3098–3100.
- [52] P. Ziesche, H. Eschrig, T. U. D. I. für Theoretische Physik, and E. P. Society. *Electronic structure of solids '91: proceedings of the 75. WE-Heraeus-Seminar and 21st Annual International Symposium on Electronic Structure of Solids held in Gaussig (Germany), March 11-15, 1991*. 1. ed. Physical research. Akademie Verlag Berlin, 1991, pp. 11–20.
- [53] C. Lee, W. Yang, and R. G. Parr. “Development of the Colle-Salvetti correlation-energy formula into a functional of the electron density”. *Physical Review B* **37** (1988), pp. 785–789.
- [54] J. P. Perdew. “Density-functional approximation for the correlation energy of the inhomogeneous electron gas”. *Physical Review B* **33** (1986), pp. 8822–8824.
- [55] P. J. Stephens, F. J. Devlin, C. F. Chabalowski, and M. J. Frisch. “Ab Initio Calculation of Vibrational Absorption and Circular Dichroism Spectra Using Density Functional Force Fields”. *The Journal of Physical Chemistry* **98** (1994), pp. 11623–11627.

- [56] A. D. Becke. “Density functional thermochemistry. IV. A new dynamical correlation functional and implications for exact, “exchange mixing”. *The Journal of Chemical Physics* **104** (1996), pp. 1040–1046.
- [57] A. D. Becke. “Density functional thermochemistry. III. The role of exact exchange”. *The Journal of Chemical Physics* **98** (1993), pp. 5648–5652.
- [58] K. Hermann, L.G.M. Pettersson, M. E. Casida, C. Daul, A. Goursot, A. Koester, E. Proynov, A. St-Amant, D.R. Salahub, Contributing authors: V. Carravetta, H. Duarte, C. Friedrich, N. Godbout, J. Guan, C. Jamorski, M. Leboeuf, M. Leetmaa, M. Nyberg, S. Patchkovskii, L. Pedocchi, F. Sim, L. Triguero, and A. Vela. *StoBe-deMon version 3.1 (2011)*.
- [59] J. T. Golab and H. L. Sellers. *Theoretical and Computational Approaches to Interface Phenomena: Proceedings of an International Conference Held in Brookings, South Dakota, August 2-4, 1993*. English. 1994th ed. New York: Springer, 1995.
- [60] G. Malli, ed. *Relativistic and Electron Correlation Effects in Molecules and Solids*. English. 1994th ed. New York: Springer, 1994.
- [61] I. Tanaka, H. Araki, M. Yoshiya, T. Mizoguchi, K. Ogasawara, and H. Adachi. “First-principles calculations of electron-energy-loss near-edge structure and near-edge x-ray-absorption fine structure of BN polytypes using model clusters”. *Physical Review B* **60** (1999), pp. 4944–4951.
- [62] L. Triguero, L. G. M. Pettersson, and H. Ågren. “Calculations of near-edge x-ray-absorption spectra of gas-phase and chemisorbed molecules by means of density-functional and transition-potential theory”. *Physical Review B* **58** (1998), pp. 8097–8110.
- [63] J. C. Slater and K. H. Johnson. “Self-Consistent-Field $X\alpha$ Cluster Method for Polyatomic Molecules and Solids”. *Physical Review B* **5** (1972), pp. 844–853.
- [64] L. Triguero, L. G. M. Pettersson, and H. Ågren. “Calculations of X-ray Emission Spectra of Molecules and Surface Adsorbates by Means of Density Functional Theory”. *J. Phys. Chem. A* **102** (1998), pp. 10599–10607.
- [65] M. Blum, M. Odellius, L. Weinhardt, S. Pookpanratana, M. Bär, Y. Zhang, O. Fuchs, W. Yang, E. Umbach, and C. Heske. “Ultrafast Proton Dynamics in Aqueous Amino Acid Solutions Studied by Resonant Inelastic Soft X-ray Scattering”. *The Journal of Physical Chemistry B* **116** (2012), pp. 13757–13764.

- [66] A. Föhlisch, J. Hasselström, P. Bennich, N. Wassdahl, O. Karis, A. Nilsson, L. Triguero, M. Nyberg, and L. G. M. Pettersson. “Ground-state interpretation of x-ray emission spectroscopy on adsorbates: CO adsorbed on Cu(100)”. *Physical Review B* **61** (2000), pp. 16229–16240.
- [67] H. Öström, L. Triguero, K. Weiss, H. Ogasawara, M. G. Garnier, D. Nordlund, M. Nyberg, L. G. M. Pettersson, and A. Nilsson. “Orbital rehybridization in n-octane adsorbed on Cu(110)”. *The Journal of Chemical Physics* **118** (2003), pp. 3782–3789.
- [68] L. Triguero and L. G. M. Pettersson. “MO and DFT approaches to the calculation of X-ray absorption/emission spectra of nitrogen atom adsorbed on Cu(100)”. *Surface Science* **398** (1998), pp. 70–83.
- [69] K. Eichkorn, O. Treutler, H. Öhm, M. Häser, and R. Ahlrichs. “Auxiliary basis sets to approximate Coulomb potentials”. *Chemical Physics Letters* **240** (1995), pp. 283–290.
- [70] W. Kutzelnigg, U. Fleischer, and M. Schindler. “The IGLO-Method: Ab-initio Calculation and Interpretation of NMR Chemical Shifts and Magnetic Susceptibilities”. en. *Deuterium and Shift Calculation*. NMR Basic Principles and Progress. Springer Berlin Heidelberg, 1990, pp. 165–262.
- [71] L. G. M. Pettersson, U. Wahlgren, and O. Gropen. “Effective core potential parameters for first and second row atoms”. *The Journal of Chemical Physics* **86** (1987), pp. 2176–2184.
- [72] C. Kolczewski, R. Püttner, O. Plashkevych, H. Ågren, V. Staemmler, M. Martins, G. Snell, A. S. Schlachter, M. Sant’Anna, G. Kaindl, and L. G. M. Pettersson. “Detailed study of pyridine at the C1s and N1s ionization thresholds: The influence of the vibrational fine structure”. *The Journal of Chemical Physics* **115** (2001), pp. 6426–6437.
- [73] M. Blum. “Electronic and Chemical Properties of Liquids and Solutions”. PhD thesis. Universität Würzburg, Fakultät für Physik und Astronomie, 2010.
- [74] O. Fuchs. “Soft x-ray spectroscopy of organic molecules and liquids”. PhD thesis. Universität Würzburg, Fakultät für Physik und Astronomie, 2009.
- [75] O. Fuchs, L. Weinhardt, M. Blum, M. Weigand, E. Umbach, M. Bär, C. Heske, J. Denlinger, Y.-D. Chuang, W. McKinney, Z. Hussain, E. Gullikson, M. Jones, P. Batson, B. Nelles, and R. Follath. “High-resolution, high-transmission soft

- x-ray spectrometer for the study of biological samples”. *Review of Scientific Instruments* **80** (2009), p. 063103.
- [76] Y. L. Jeyachandran, F. Meyer, S. Nagarajan, A. Benkert, M. Bär, M. Blum, W. Yang, F. Reinert, C. Heske, L. Weinhardt, and M. Zharnikov. “Ion-Solvation-Induced Molecular Reorganization in Liquid Water Probed by Resonant Inelastic Soft X-ray Scattering”. *The Journal of Physical Chemistry Letters* **5** (2014), pp. 4143–4148.
- [77] L. Weinhardt, M. Weigand, O. Fuchs, M. Bär, M. Blum, J. D. Denlinger, W. Yang, E. Umbach, and C. Heske. “Nuclear dynamics in the core-excited state of aqueous ammonia probed by resonant inelastic soft x-ray scattering”. *Physical Review B* **84** (2011), p. 104202.
- [78] R. R. T. Marinho, A. F. Lago, M. G. P. Homem, L. H. Coutinho, G. G. B. de Souza, and A. Naves de Brito. “Gas phase photoabsorption and mass spectra of l-alanine and l-proline in the soft X-ray region”. *Chemical Physics* **324** (2006), pp. 420–424.
- [79] L. Weinhardt, O. Fuchs, M. Blum, M. Bär, M. Weigand, J. Denlinger, Y. Zubavichus, M. Zharnikov, M. Grunze, C. Heske, and E. Umbach. “Resonant X-ray emission spectroscopy of liquid water: Novel instrumentation, high resolution, and the ”map“ approach”. *Journal of Electron Spectroscopy and Related Phenomena* **177** (2010), pp. 206–211.
- [80] V. S. Lusvardi, M. A. Barteau, J. G. Chen, J. Eng, B. Frühberger, and A. Teplyakov. “An NEXAFS investigation of the reduction and reoxidation of TiO₂(001)”. *Surface Science* **397** (1998), pp. 237–250.
- [81] B. Watts and H. Ade. “A simple method for determining linear polarization and energy calibration of focused soft X-ray beams”. *Journal of Electron Spectroscopy and Related Phenomena* **162** (2008), pp. 49–55.
- [82] C. T. Chen, Y. Ma, and F. Sette. “K-shell photoabsorption of the N₂ molecule”. *Physical Review A* **40** (1989), p. 6737.
- [83] F. Meyer, L. Weinhardt, M. Blum, M. Bär, R. G. Wilks, W. Yang, C. Heske, and F. Reinert. “Non-equivalent carbon atoms in the resonant inelastic soft X-ray scattering map of cysteine”. *The Journal of Chemical Physics* **138** (2013), p. 034306.

- [84] I. Wagner and H. Musso. “New Naturally Occurring Amino Acids”. *Angewandte Chemie International Edition in English* **22** (1983), pp. 816–828.
- [85] H. R. Horton, L. A. Moran, K. G. Scrimgeour, M. D. Perry, and J. D. Rawn. *Biochemie - Das Basislehrbuch - aktuell und anwendungsorientiert*. Deutsch. 4., aktualisierte Auflage. München u.a.: Addison-Wesley Verlag, 2008.
- [86] F. Meyer, M. Blum, A. Benkert, D. Hauschild, S. Nagarajan, R. G. Wilks, J. Andersson, W. Yang, M. Zharnikov, M. Bär, C. Heske, F. Reinert, and L. Weinhardt. “Building Block Picture“ of the Electronic Structure of Aqueous Cysteine Derived from Resonant Inelastic Soft X-ray Scattering”. *The Journal of Physical Chemistry B* **118** (2014), pp. 13142–13150.
- [87] M. Schreyer, L. Guo, S. Thirunahari, F. Gao, and M. Garland. “Simultaneous determination of several crystal structures from powder mixtures: the combination of powder X-ray diffraction, band-target entropy minimization and Rietveld methods”. en. *Journal of Applied Crystallography* **47** (2014), pp. 659–667.
- [88] D. R. Lide. *CRC Handbook of Chemistry and Physics, Internet Version 2005*. Ed. by D. R. Lide. Boca Raton, FL: CRC Press, 2005.
- [89] L. Åsbrink, A. Svensson, W. von Niessen, and G. Bieri. “30.4-nm He(II) photoelectron spectra of organic molecules: Part V. Hetero-compounds containing first-row elements (C, H, B, N, O, F)”. *Journal of Electron Spectroscopy and Related Phenomena* **24** (1981), pp. 293–314.
- [90] A. Benkert, F. Meyer, D. Hauschild, M. Blum, W. Yang, M. Bär, F. Reinert, C. Heske, and L. Weinhardt. “Isotope effects in the resonant inelastic soft x-ray scattering maps of gas-phase methanol”. *to be published* (2015).
- [91] J. Nordgren and N. Wassdahl. “Current Status and Future Prospects for Ultra-Soft X-ray Emission Spectroscopy”. *Physica Scripta* **1990** (1990), p. 103.
- [92] P. A. Williams, C. E. Hughes, and K. D. M. Harris. “L-Lysine: Exploiting Powder X-ray Diffraction to Complete the Set of Crystal Structures of the 20 Directly Encoded Proteinogenic Amino Acids”. en. *Angewandte Chemie International Edition* **54** (2015), pp. 3973–3977.
- [93] B. M. Messer, C. D. Cappa, J. D. Smith, W. S. Drisdell, C. P. Schwartz, R. C. Cohen, and R. J. Saykally. “Local Hydration Environments of Amino Acids and

- Dipeptides Studied by X-ray Spectroscopy of Liquid Microjets”. *The Journal of Physical Chemistry B* **109** (2005), pp. 21640–21646.
- [94] C. Pérez-Casas and A. K. Yatsimirsky. “Detailing Hydrogen Bonding and Deprotonation Equilibria between Anions and Urea/Thiourea Derivatives”. *The Journal of Organic Chemistry* **73** (2008), pp. 2275–2284.
- [95] H. Wincel. “Hydration Energies of Deprotonated Amino Acids from Gas Phase Equilibria Measurements”. *Journal of the American Society for Mass Spectrometry* **19** (2008), pp. 1091–1097.
- [96] O. Plekan, V. Feyer, R. Richter, M. Coreno, M. de Simone, K. C. Prince, and V. Carravetta. “Investigation of the Amino Acids Glycine, Proline, and Methionine by Photoemission Spectroscopy”. *The Journal of Physical Chemistry A* **111** (2007), pp. 10998–11005.
- [97] G. Wiech, N. Auer, A. Šimůnek, J. Vackář, A. Hammerschmidt, and G. Rittmayer. “Diamond-like hydrogenated amorphous carbon films studied by X-ray emission spectroscopy”. *Diamond and Related Materials* **6** (1997), pp. 944–951.
- [98] Y. Zubavichus, M. Zharnikov, A. Shaporenko, O. Fuchs, L. Weinhardt, C. Heske, E. Umbach, J. D. Denlinger, and M. Grunze. “Soft X-ray Induced Decomposition of Phenylalanine and Tyrosine: A Comparative Study”. *J. Phys. Chem. A* **108** (2004), pp. 4557–4565.
- [99] F. Hennies, A. Pietzsch, M. Berglund, A. Föhlisch, T. Schmitt, V. Strocov, H. O. Karlsson, J. Andersson, and J.-E. Rubensson. “Resonant Inelastic Scattering Spectra of Free Molecules with Vibrational Resolution”. *Physical Review Letters* **104** (2010), p. 193002.
- [100] Y. Zubavichus, A. Shaporenko, M. Grunze, and M. Zharnikov. “Innershell Absorption Spectroscopy of Amino Acids at All Relevant Absorption Edges”. *The Journal of Physical Chemistry A* **109** (2005), pp. 6998–7000.
- [101] K. Kaznacheyev, A. Osanna, C. Jacobsen, O. Plashkevych, O. Vahtras, Ågren, V. Carravetta, and A. P. Hitchcock. “Innershell Absorption Spectroscopy of Amino Acids”. *The Journal of Physical Chemistry A* **106** (2002), pp. 3153–3168.
- [102] M. Fleck and A. Petrosyan. *Salts of Amino Acids: Crystallization, Structure and Properties*. 2014th ed. Springer, 2014.
- [103] F. A. Momany, R. F. McGuire, A. W. Burgess, and H. A. Scheraga. “Energy parameters in polypeptides. VII. Geometric parameters, partial atomic charges,

- nonbonded interactions, hydrogen bond interactions, and intrinsic torsional potentials for the naturally occurring amino acids". *The Journal of Physical Chemistry* **79** (1975), pp. 2361–2381.
- [104] R. Linder, K. Seefeld, A. Vavra, and K. Kleinermanns. "Gas phase infrared spectra of nonaromatic amino acids". *Chemical Physics Letters* **453** (2008), pp. 1–6.
- [105] A. K. Covington, R. G. Bates, and R. A. Durst. "Definition of pH scales, standard reference values, measurement of pH and related terminology (Recommendations 1984)". *Pure and Applied Chemistry* **57** (1985).
- [106] O. Fuchs, M. Zharnikov, L. Weinhardt, M. Blum, M. Weigand, Y. Zubavichus, M. Bär, F. Maier, J. D. Denlinger, C. Heske, M. Grunze, and E. Umbach. "Isotope and Temperature Effects in Liquid Water Probed by X-Ray Absorption and Resonant X-Ray Emission Spectroscopy". *Physical Review Letters* **100** (2008), p. 027801.
- [107] T. Tokushima, Y. Harada, O. Takahashi, Y. Senba, H. Ohashi, L. Pettersson, A. Nilsson, and S. Shin. "High resolution X-ray emission spectroscopy of liquid water: The observation of two structural motifs". *Chemical Physics Letters* **460** (2008), pp. 387–400.
- [108] P. Wernet, D. Nordlund, U. Bergmann, M. Cavalleri, M. Odellius, H. Ogasawara, L. Nilsson, T. K. Hirsch, L. Ojamäe, P. Glatzel, L. G. M. Pettersson, and A. Nilsson. "The Structure of the First Coordination Shell in Liquid Water". *Science* **304** (2004), pp. 995–999.
- [109] J. D. Smith, C. D. Cappa, K. R. Wilson, B. M. Messer, R. C. Cohen, and R. J. Saykally. "Energetics of Hydrogen Bond Network Rearrangements in Liquid Water". *Science* **306** (2004), pp. 851–853.
- [110] K. M. Lange, R. Könnecke, M. Soldatov, R. Golnak, J. Rubensson, A. Soldatov, and E. F. Aziz. "On the Origin of the Hydrogen-Bond-Network Nature of Water: X-Ray Absorption and Emission Spectra of Water-Acetonitrile Mixtures". *Angewandte Chemie* **123** (2011), pp. 10809–10813.
- [111] K. M. Lange, R. Könnecke, S. Ghadimi, R. Golnak, M. A. Soldatov, K. F. Hodeck, A. Soldatov, and E. F. Aziz. "High resolution X-ray emission spectroscopy of water and aqueous ions using the micro-jet technique". *Chemical Physics* **377** (2010), pp. 1–5.

BIBLIOGRAPHY

- [112] M. Odelius. "Information Content in O_{1s} K-edge X-ray Emission Spectroscopy of Liquid Water". *The Journal of Physical Chemistry A* **113** (2009), pp. 8176–8181.
- [113] K. M. Lange, M. Soldatov, R. Golnak, M. Gotz, N. Engel, R. Könnicke, J.-E. Rubensson, and E. F. Aziz. "X-ray emission from pure and dilute H_2O and D_2O in a liquid microjet: Hydrogen bonds and nuclear dynamics". *Physical Review B* **85** (2012), p. 155104.
- [114] Y. Horikawa, T. Tokushima, Y. Harada, O. Takahashi, A. Chainani, Y. Senba, H. Ohashi, A. Hiraya, and S. Shin. "Identification of valence electronic states of aqueous acetic acid in acid-base equilibrium using site-selective X-ray emission spectroscopy". *Physical Chemistry Chemical Physics* **11** (2009), p. 8676.
- [115] L. J. Henderson. "Concerning the relationship between the strength of acids and their capacity to preserve neutrality". *American Journal of Physiology-Legacy Content* **21** (1908), pp. 173–179.
- [116] L. J. Henderson. "The theory of neutrality regulation in the animal organism". *American Journal of Physiology-Legacy Content* **21** (1908), pp. 427–448.
- [117] H. N. Po and N. M. Senozan. "The Henderson-Hasselbalch Equation: Its History and Limitations". *Journal of Chemical Education* **78** (2001), p. 1499.
- [118] Y. Horikawa, T. Tokushima, A. Hiraya, and S. Shin. "Pronounced polarization anisotropy in resonant X-ray emission from acetic acid molecules in solution". *Physical Chemistry Chemical Physics* **12** (2010), p. 9165.
- [119] T. Tokushima, Y. Horikawa, Y. Harada, O. Takahashi, A. Hiraya, and S. Shin. "Selective observation of the two oxygen atoms at different sites in the carboxyl group ($-COOH$) of liquid acetic acid". *Physical Chemistry Chemical Physics* **11** (2009), p. 1679.
- [120] J. Gråsjö, E. Andersson, J. Forsberg, L. Duda, E. Henke, W. Pokapanich, O. BjöÅårneholm, J. Andersson, A. Pietzsch, F. Hennies, and J.-E. Rubensson. "Local Electronic Structure of Functional Groups in Glycine As Anion, Zwitterion, and Cation in Aqueous Solution". *The Journal of Physical Chemistry B* **113** (2009), pp. 16002–16006.
- [121] O. Plekan, V. Feyer, R. Richter, M. Coreno, M. de Simone, K. Prince, and V. Carravetta. "An X-ray absorption study of glycine, methionine and proline".

- Journal of Electron Spectroscopy and Related Phenomena* **155** (2007), pp. 47–53.
- [122] D. C. Newbury, I. Ishii, and A. P. Hitchcock. “Inner shell electron-energy loss spectroscopy of some heterocyclic molecules”. *Canadian Journal of Chemistry* **64** (1986), pp. 1145–1155.
- [123] J. M. Friedman, D. L. Rousseau, M. R. Ondrias, and R. A. Stepnoski. “Transient Raman study of hemoglobin: structural dependence of the iron-histidine linkage”. en. *Science* **218** (1982), pp. 1244–1246.
- [124] M. D. Green and T. E. Long. “Designing Imidazole-Based Ionic Liquids and Ionic Liquid Monomers for Emerging Technologies”. *Polymer Reviews* **49** (2009), pp. 291–314.
- [125] P. Walden. “Über die Molekulargröße und elektrische Leitfähigkeit einiger geschmolzener Salze”. *Bull. Acad. Imper. Sci. St. Petersburg* **8** (1914), pp. 405–422.
- [126] N. V. Plechkova and K. R. Seddon. “Applications of ionic liquids in the chemical industry”. en. *Chemical Society Reviews* **37** (2007), pp. 123–150.
- [127] M. Maase. “Erstes technisches Verfahren mit ionischen Flüssigkeiten”. en. *Chemie in unserer Zeit* **38** (2004), pp. 434–435.
- [128] D. Nolting, N. Ottosson, M. Faubel, I. V. Hertel, and B. Winter. “Pseudoequivalent Nitrogen Atoms in Aqueous Imidazole Distinguished by Chemical Shifts in Photoelectron Spectroscopy”. *Journal of the American Chemical Society* **130** (2008), pp. 8150–8151.
- [129] M. J. Thomason, C. R. Seabourne, B. M. Sattelle, G. A. Hembury, J. S. Stevens, A. J. Scott, E. F. Aziz, and S. L. M. Schroeder. “Self-association of organic solutes in solution: a NEXAFS study of aqueous imidazole”. en. *Faraday Discussions* (2015).
- [130] L. Gontrani, R. Caminiti, L. Bencivenni, and C. Sadun. “Molecular aggregation phenomena in solution: an energy dispersive X-ray diffraction study of concentrated imidazole water solutions”. *Chemical Physics Letters* **301** (1999), pp. 131–137.
- [131] F. Peral and E. Gallego. “Self-association of imidazole and its methyl derivatives in aqueous solution. A study by ultraviolet spectroscopy”. *Journal of Molecular Structure* **415** (1997), pp. 187–196.

BIBLIOGRAPHY

- [132] Y. Luo, H. Ågren, and F. Gel'mukhanov. "Polarization anisotropy in resonant x-ray emission from molecules". *Physical Review A* **53** (1996), pp. 1340–1348.
- [133] H. Ågren, Y. Luo, F. Gel'mukhanov, and H. J. A. Jensen. "Screening in resonant X-ray emission of molecules". *Journal of Electron Spectroscopy and Related Phenomena* **82** (1996), pp. 125–134.
- [134] P. Skytt, P. Glans, K. Gunnelin, J. Guo, J. Nordgren, Y. Luo, and H. Ågren. "Role of screening and angular distributions in resonant x-ray emission of CO". *Physical Review A* **55** (1997), pp. 134–145.
- [135] R. C. C. Perera, R. E. LaVilla, P. L. Cowan, T. Jach, and B. Karlin. "Cl $K\beta$ (K-V) emission of CFCl_3 excited by synchrotron radiation below and above Cl_{1s} binding energy: perturbation effects in a highly excited neutral molecule". en. *Physica Scripta* **36** (1987), p. 132.
- [136] D. W. Lindle, P. L. Cowan, T. Jach, R. E. LaVilla, R. D. Deslattes, and R. C. C. Perera. "Polarized x-ray emission studies of methyl chloride and the chlorofluoromethanes". *Physical Review A* **43** (1991), pp. 2353–2366.
- [137] P. Skytt, P. Glans, J.-H. Guo, K. Gunnelin, C. S  the, J. Nordgren, F. K. Gel'mukhanov, A. Cesar, and H. Ågren. "Quenching of Symmetry Breaking in Resonant Inelastic X-Ray Scattering by Detuned Excitation". *Physical Review Letters* **77** (1996), pp. 5035–5038.
- [138] Y. Luo, H. Ågren, F. Gel'mukhanov, J. Guo, P. Skytt, N. Wassdahl, and J. Nordgren. "Symmetry-selective resonant inelastic x-ray scattering of C_{60} ". *Physical Review B* **52** (1995), pp. 14479–14496.
- [139] F. Gel'mukhanov and H. Ågren. "Channel interference in X-ray Raman scattering: parity selection rules, dephasing and localization of core holes". *Journal of Electron Spectroscopy and Related Phenomena* **93** (1998), pp. 31–37.
- [140] F. H. Stillinger. "Water Revisited". *Science* **209** (1980), pp. 451–457.
- [141] H. Ohtaki and T. Radnai. "Structure and dynamics of hydrated ions". *Chemical Reviews* **93** (1993), pp. 1157–1204.
- [142] Y. Marcus. "Effect of Ions on the Structure of Water: Structure Making and Breaking". *Chemical Reviews* **109** (2009), pp. 1346–1370.

-
- [143] J. Nordgren, L. P. Werme, H. Agren, C. Nordling, and K. Siegbahn. “The X-ray emission spectrum of water”. *Journal of Physics B: Atomic and Molecular Physics* **8** (1975), p. L18.
- [144] S. Kashtanov, A. Augustsson, Y. Luo, J.-H. Guo, C. S athe, J.-E. Rubensson, H. Siegbahn, J. Nordgren, and H.  gren. “Local structures of liquid water studied by x-ray emission spectroscopy”. *Physical Review B* **69** (2004), p. 024201.
- [145] J. Guo and Y. Luo. “Molecular structure in water and solutions studied by photon-in/photon-out soft X-ray spectroscopy”. *Journal of Electron Spectroscopy and Related Phenomena* **177** (2010), pp. 181–191.
- [146] T. D. K hne and R. Z. Khaliullin. “Electronic signature of the instantaneous asymmetry in the first coordination shell of liquid water”. en. *Nature Communications* **4** (2013), p. 1450.
- [147] M. P. Ljungberg, A. Nilsson, and L. G. M. Pettersson. “Semiclassical description of nuclear dynamics in x-ray emission of water”. *Physical Review B* **82** (2010), p. 245115.
- [148] A. Nilsson and L. Pettersson. “Perspective on the structure of liquid water”. *Chemical Physics* **389** (2011), pp. 1–34.
- [149] M. Leetmaa, K. T. Wikfeldt, M. P. Ljungberg, M. Odelius, J. Swenson, A. Nilsson, and L. G. M. Pettersson. “Diffraction and IR/Raman data do not prove tetrahedral water”. *The Journal of Chemical Physics* **129** (2008), p. 084502.
- [150] T. Head-Gordon and G. Hura. “Water Structure from Scattering Experiments and Simulation”. *Chemical Reviews* **102** (2002), pp. 2651–2670.
- [151] A. K. Soper. “Joint structure refinement of x-ray and neutron diffraction data on disordered materials: application to liquid water”. *Journal of Physics: Condensed Matter* **19** (2007), p. 335206.
- [152] C. J. Fecko, J. D. Eaves, J. J. Loparo, A. Tokmakoff, and P. L. Geissler. “Ultrafast Hydrogen-Bond Dynamics in the Infrared Spectroscopy of Water”. en. *Science* **301** (2003), pp. 1698–1702.
- [153] B. Winter and M. Faubel. “Photoemission from Liquid Aqueous Solutions”. *Chemical Reviews* **106** (2006), pp. 1176–1211.
- [154] L. Weinhardt, A. Benkert, F. Meyer, M. Blum, R. G. Wilks, W. Yang, M. B r, F. Reinert, and C. Heske. “Nuclear dynamics and spectator effects in resonant

- inelastic soft x-ray scattering of gas-phase water molecules”. *The Journal of Chemical Physics* **136** (2012),
- [155] J.-H. Guo, Y. Luo, A. Augustsson, J.-E. Rubensson, C. S athe, H.  gren, H. Siegbahn, and J. Nordgren. “X-Ray Emission Spectroscopy of Hydrogen Bonding and Electronic Structure of Liquid Water”. *Physical Review Letters* **89** (2002), p. 137402.
- [156] O. Fuchs, M. Zharnikov, L. Weinhardt, M. Blum, M. Weigand, Y. Zubavichus, M. B ar, F. Maier, J. D. Denlinger, C. Heske, M. Grunze, and E. Umbach. “A Reply to the Comment by L. G. M. Pettersson et al.” *Physical Review Letters* **100** (2008), p. 249802.
- [157] T. Tokushima, Y. Harada, Y. Horikawa, O. Takahashi, Y. Senba, H. Ohashi, L. G. Pettersson, A. Nilsson, and S. Shin. “High resolution X-ray emission spectroscopy of water and its assignment based on two structural motifs”. *Journal of Electron Spectroscopy and Related Phenomena* **177** (2010), pp. 192–205.
- [158] Y. Harada, T. Tokushima, Y. Horikawa, O. Takahashi, H. Niwa, M. Kobayashi, M. Oshima, Y. Senba, H. Ohashi, K. T. Wikfeldt, A. Nilsson, L. G. M. Pettersson, and S. Shin. “Selective Probing of the OH or OD Stretch Vibration in Liquid Water Using Resonant Inelastic Soft-X-Ray Scattering”. *Physical Review Letters* **111** (2013), p. 193001.
- [159] C. D. Cappa, J. D. Smith, K. R. Wilson, B. M. Messer, M. K. Gilles, R. C. Cohen, and R. J. Saykally. “Effects of Alkali Metal Halide Salts on the Hydrogen Bond Network of Liquid Water”. *J. Phys. Chem. B* **109** (2005), pp. 7046–7052.
- [160] C. D. Cappa, J. D. Smith, B. M. Messer, R. C. Cohen, and R. J. Saykally. “The Electronic Structure of the Hydrated Proton: A Comparative X-ray Absorption Study of Aqueous HCl and NaCl Solutions”. *The Journal of Physical Chemistry B* **110** (2006), pp. 1166–1171.
- [161] E. F. Aziz, A. Zimina, M. Freiwald, S. Eisebitt, and W. Eberhardt. “Molecular and electronic structure in NaCl electrolytes of varying concentration: Identification of spectral fingerprints”. *The Journal of Chemical Physics* **124** (2006), p. 114502.
- [162] B. Brena, D. Nordlund, M. Odelius, H. Ogasawara, A. Nilsson, and L. G. M. Pettersson. “Ultrafast Molecular Dissociation of Water in Ice”. *Physical Review Letters* **93** (2004), p. 148302.

- [163] E. Gilberg, M. J. Hanus, and B. Foltz. “Investigation of the electronic structure of ice by high resolution x-ray spectroscopy”. *The Journal of Chemical Physics* **76** (1982), pp. 5093–5097.
- [164] S. Thürmer, M. Ončák, N. Ottosson, R. Seidel, U. Hergenhahn, S. E. Bradforth, P. Slavíček, and B. Winter. “On the nature and origin of dicationic, charge-separated species formed in liquid water on X-ray irradiation”. *Nature Chemistry* **5** (2013), pp. 590–596.
- [165] H. J. Bakker. “Structural Dynamics of Aqueous Salt Solutions”. *Chemical Reviews* **108** (2008), pp. 1456–1473.
- [166] H. J. Kulik, N. Marzari, A. A. Correa, D. Prendergast, E. Schwegler, and G. Galli. “Local Effects in the X-ray Absorption Spectrum of Salt Water”. *The Journal of Physical Chemistry B* **114** (2010), pp. 9594–9601.
- [167] I. Waluyo, C. Huang, D. Nordlund, U. Bergmann, T. M. Weiss, L. G. M. Pettersson, and A. Nilsson. “The structure of water in the hydration shell of cations from x-ray Raman and small angle x-ray scattering measurements”. *The Journal of Chemical Physics* **134** (2011),
- [168] J.-H. Guo, A. Augustsson, S. Kashtanov, D. Spångberg, J. Nordgren, K. Hermansson, Y. Luo, and A. Augustsson. “The interaction of cations and liquid water studied by resonant soft-X-ray absorption and emission spectroscopy”. *Journal of Electron Spectroscopy and Related Phenomena* **144** (2005), pp. 287–290.
- [169] T. Petit, K. M. Lange, G. Conrad, K. Yamamoto, C. Schwanke, K. F. Hodeck, M. Dantz, T. Brandenburg, E. Suljoti, and E. F. Aziz. “Probing ion-specific effects on aqueous acetate solutions: Ion pairing versus water structure modifications”. *Structural Dynamics* **1** (2014), p. 034901.
- [170] J. Gråsjö, E. Andersson, J. Forsberg, E. F. Aziz, B. Brena, C. Johansson, J. Nordgren, L. Duda, J. Andersson, F. Hennies, J.-E. Rubensson, and P. Hansson. “Electronic Structure of Water Molecules Confined in a Micelle Lattice”. *The Journal of Physical Chemistry B* **113** (2009), pp. 8201–8205.
- [171] B. Winter, E. F. Aziz, N. Ottosson, M. Faubel, N. Kosugi, and I. V. Hertel. “Electron Dynamics in Charge-Transfer-to-Solvent States of Aqueous Chloride Revealed by Cl_{2p} Resonant Auger-Electron Spectroscopy”. *Journal of the American Chemical Society* **130** (2008), pp. 7130–7138.

BIBLIOGRAPHY

- [172] F. Gel'mukhanov, H. Ågren, M. Neeb, J.-E. Rubensson, and A. Bringer. "Integral properties of channel interference in resonant X-ray scattering". *Physics Letters A* **211** (1996), pp. 101–108.
- [173] S. Imoto, S. S. Xantheas, and S. Saito. "Molecular origin of the difference in the HOH bend of the IR spectra between liquid water and ice". *The Journal of Chemical Physics* **138** (2013), p. 054506.
- [174] F. Hennies, S. Polyutov, I. Minkov, A. Pietzsch, M. Nagasono, H. Ågren, L. Triguero, M.-N. Piancastelli, W. Wurth, F. Gel'mukhanov, and A. Föhlisch. "Dynamic interpretation of resonant x-ray Raman scattering: Ethylene and benzene". *Physical Review A* **76** (2007), p. 032505.
- [175] P. Ganguly, P. Schravendijk, B. Hess, and N. F. A. van der Vegt. "Ion Pairing in Aqueous Electrolyte Solutions with Biologically Relevant Anions". *The Journal of Physical Chemistry B* **115** (2011), pp. 3734–3739.
- [176] F. Guo and J. M. Friedman. "Charge Density-Dependent Modifications of Hydration Shell Waters by Hofmeister Ions". *Journal of the American Chemical Society* **131** (2009), pp. 11010–11018.
- [177] P. Koelsch, P. Viswanath, H. Motschmann, V. Shapovalov, G. Brezesinski, H. Möhwald, D. Horinek, R. R. Netz, K. Giewekemeyer, T. Salditt, H. Schollmeyer, R. von Klitzing, J. Daillant, and P. Guenoun. "Specific ion effects in physicochemical and biological systems: Simulations, theory and experiments". *Colloids and Surfaces A: Physicochemical and Engineering Aspects* **303** (2007), pp. 110–136.
- [178] P. Koelsch and H. Motschmann. "An experimental route to Hofmeister". *Current Opinion in Colloid & Interface Science* **9** (2004), pp. 87–91.
- [179] W. Kunz, P. Lo Nostro, and B. W. Ninham. "The present state of affairs with Hofmeister effects". *Current Opinion in Colloid & Interface Science* **9** (2004), pp. 1–18.
- [180] W. Kunz. "Specific ion effects in colloidal and biological systems". *Current Opinion in Colloid & Interface Science* **15** (2010), pp. 34–39.
- [181] Z. Yin, I. Rajkovic, K. Kubicek, W. Quevedo, A. Pietzsch, P. Wernet, A. Föhlisch, and S. Techert. "Probing the Hofmeister Effect with Ultrafast Core-ÅHole Spectroscopy". *The Journal of Physical Chemistry B* **118** (2014), pp. 9398–9403.

- [182] Y. Zhang and P. S. Cremer. “Interactions between macromolecules and ions: the Hofmeister series”. *Current Opinion in Chemical Biology* **10** (2006), pp. 658–663.
- [183] C. Schwanke, R. Golnak, J. Xiao, and K. M. Lange. “Electrochemical flowcell for in-situ investigations by soft x-ray absorption and emission spectroscopy”. *Review of Scientific Instruments* **85** (2014), p. 103120.
- [184] C. Escudero, P. Jiang, E. Pach, F. Borondics, M. W. West, A. Tuxen, M. Chintapalli, S. Carencio, J. Guo, and M. Salmeron. “A reaction cell with sample laser heating for in situ soft X-ray absorption spectroscopy studies under environmental conditions”. en. *Journal of Synchrotron Radiation* **20** (2013), pp. 504–508.

OWN PUBLICATIONS

- [A1] F. Meyer, L. Weinhardt, M. Blum, M. Bär, R. G. Wilks, W. Yang, C. Heske, and F. Reinert. “Non-equivalent carbon atoms in the resonant inelastic soft X-ray scattering map of cysteine”. *The Journal of Chemical Physics* **138** (2013), p. 034306.
- [A2] F. Meyer, M. Blum, A. Benkert, D. Hauschild, S. Nagarajan, R. G. Wilks, J. Andersson, W. Yang, M. Zharnikov, M. Bär, C. Heske, F. Reinert, and L. Weinhardt. “”Building Block Picture“ of the Electronic Structure of Aqueous Cysteine Derived from Resonant Inelastic Soft X-ray Scattering”. *The Journal of Physical Chemistry B* **118** (2014), pp. 13142–13150.
- [A3] Y. L. Jeyachandran, F. Meyer, S. Nagarajan, A. Benkert, M. Bär, M. Blum, W. Yang, F. Reinert, C. Heske, L. Weinhardt, and M. Zharnikov. “Ion-Solvation-Induced Molecular Reorganization in Liquid Water Probed by Resonant Inelastic Soft X-ray Scattering”. *The Journal of Physical Chemistry Letters* **5** (2014), pp. 4143–4148.
- [A4] D. Hauschild, F. Meyer, S. Pohlner, R. Lechner, R. Dietmüller, J. Palm, C. Heske, L. Weinhardt, and F. Reinert. “Impact of environmental conditions on the chemical surface properties of Cu(In,Ga)(S,Se)₂ thin-film solar cell absorbers”. *Journal of Applied Physics* **115** (2014), p. 183707.
- [A5] D. Hauschild, F. Meyer, A. Benkert, D. Kreikemeyer-Lorenzo, S. Pohlner, J. Palm, M. Blum, W. Yang, R. G. Wilks, M. Bär, C. Heske, L. Weinhardt, and F. Reinert. “Annealing-Induced Effects on the Chemical Structure of the In₂S₃/CuIn(S,Se)₂ Thin-Film Solar Cell Interface”. *The Journal of Physical Chemistry C* **119** (2015), pp. 10412–10416.
- [A6] L. Weinhardt, A. Benkert, F. Meyer, M. Blum, R. G. Wilks, W. Yang, M. Bär, F. Reinert, and C. Heske. “Nuclear dynamics and spectator effects in resonant inelastic soft x-ray scattering of gas-phase water molecules”. *The Journal of Chemical Physics* **136** (2012),

- [A7] A. Benkert, M. Blum, F. Meyer, R. G. Wilks, W. Yang, M. Bär, F. Reinert, C. Heske, and L. Weinhardt. “Setup for in situ investigation of gases and gas/solid interfaces by soft x-ray emission and absorption spectroscopy”. *Review of Scientific Instruments* **85** (2014), p. 015119.
- [A8] L. Weinhardt, M. Blum, O. Fuchs, A. Benkert, F. Meyer, M. Bär, J. Denlinger, W. Yang, F. Reinert, and C. Heske. “RIXS investigations of liquids, solutions, and liquid/solid interfaces”. *Journal of Electron Spectroscopy and Related Phenomena* **188** (2013), pp. 111–120.
- [A9] A. Benkert, F. Meyer, D. Hauschild, M. Blum, W. Yang, M. Bär, F. Reinert, C. Heske, and L. Weinhardt. “Isotope effects in the resonant inelastic soft x-ray scattering maps of gas-phase methanol”. *to be published* (2015).

DANKSAGUNG

An dieser Stelle ist es nun Zeit all jenen Menschen zu danken, die mich in den letzten Jahren tatkräftig unterstützt, motiviert, belehrt und mit Ideen gefüttert haben und damit maßgeblich am Gelingen dieser Arbeit beteiligt waren.

Mein Dank gilt an erster Stelle meinem Doktorvater Prof. Dr. Friedrich Reinert von der Experimentellen Physik 7 der Universität Würzburg, der mir in den letzten Jahren ein großzügiger Chef und Lehrer war, von dem ich sehr viel über die Leidenschaft an der Physik und die Begeisterung an der Wissenschaft gelernt habe. Ohne das Projekt der Deutschen Forschungsgemeinschaft und der Kooperation mit der Universität Heidelberg und dem Karlsruher Institut für Technologie (KIT) wäre diese Arbeit nie entstanden.

Zudem möchte ich mich bei Prof. Dr. Michael Zharnikov, Dr. Nagarajan Sankaranarayanan, und Dr. Jeyachandran Yekkoni von der Universität in Heidelberg für die außergewöhnliche Kooperation bedanken. Bei Dr. Nagarajan Sankaranarayanan möchte ich mich gesondert bedanken, da er mich geduldig in die Welt der Chemie und die Etikette im Chemielabor eingeführt hat und wir zusammen tolle Salz-Daten gemessen haben. Bei Dr. Jeyachandran Yekkoni möchte ich mich für die vielen Diskussionen, die letztendlich zur Veröffentlichung der Salz-Daten geführt haben bedanken.

Des Weiteren möchte ich mich bei Prof. Dr. Clemens Heske vom Karlsruher Institut für Technologie bedanken, der viele meiner Ergebnisse mit mir kritisch diskutiert hat und mich unter anderem durch zahlreiche Korrekturen, Kommentare und Anmerkungen in die hohe Kunst des Paper Schreibens eingewießen hat.

Als nächstes gilt mein Dank Dr. Lothar Weinhardt (IPS, KIT), für die exzellente Anleitung, das unerschöpfliche Vertrauen, die Motivation, die wissenschaftlichen Diskussionen und dein schon fast erschreckendes Gespür für Verbesserungen. Ob auf Messzeiten, beim Veröffentlichenden von wissenschaftlichen Artikeln, dem Programmieren von IGOR Prozeduren, oder dem Schreiben dieser Arbeit, durch deine Anleitung und dein Fingerspitzengefühl mich wieder auf den richtigen Weg zu schubsen sollte ich mich mal verrannt haben, habe ich in den letzten Jahren viel Dinge geschaffen auf die ich sehr stolz bin.

Der Grundstein dieser Arbeit wurde von Frau Dr. Monika Blum von der Universität in Las Vegas gelegt, die sowohl die Messapparatur samt Flüssigkeitszelle entworfen

DANKSAGUNG

hat, als auch erste fundamentale Experimente an Flüssigkeiten und organischen Molekülen durchgeführt hat. Vielen Dank für die vielen Tag- und Nachtschichten die wir zusammen bestritten haben, die vielen Diskussionen, die Anregungen und Erfahrungen, die du mit mir geteilt hast.

Gerade die auf den Messzeiten an der ALS entstandenen Daten sind nicht das Werk eines einzelnen sondern der Gruppe. An oberster Stelle steht hier Andreas Benkert, zwar haben wir uns auf Messzeit meistens nur zum Aufbauen, den Abendessen, der Übergabe des Laborbuchs und zum Abbau gesehen, aber so manches der hier gezeigte Spektrum entstand in seiner Schicht. Danke dafür.

Um beim Beamteam zu bleiben, ein großes Dankeschön für die Unterstützung, die Ratschläge und die Gelassenheit, wenn mal was schief ging, geht an Prof. Dr. Marcus Bär und Dr. Regan Wilks vom Helmholtz-Zentrum Berlin. Danken möchte ich auch Douglas Hanks, Dr. Kimberley Horsley und dem Rest der Gruppe der Universität aus Las Vegas, für die viele Hilfe im Chemielabor, bei Auf- und Abbau von SALSA und beim stundenlangen kalibrieren des Spektrometers.

Die gesamte Würzburger Arbeitsgruppe darf natürlich auch nicht fehlen. Allen voran geht mein Dank an Dirk Hauschild für die Hilfe bei den XPS Spektren, den vielen Diskussionen über Aminosäuren, Salze und Solarzellen und dafür, dass er mir immer mal wieder „seine“ Kammer anvertraut hat und auch nicht sauer war wenn ich die Schleuse mit einer neuen Aminosäure tapeziert habe. Ein Dankeschön geht an Judith Thoma, die eine Bachelorarbeit bei mir überlebt und tolle XPS Spektren von Prolin gemessen hat.

Ein dickes Danke geht an die besten Bürokollegen und Freunde die man sich nur wünschen kann: Holger Schwab, Andreas Benkert, Dirk Hauschild, Henriette Maaß. Danke für die ausgezeichnete wissenschaftliche Zusammenarbeit sowie die geile Zeit die wir auch abseits der Uni hatten.

Die anderen Kollegen dürfen natürlich auch nicht fehlen. Vielen Dank für eure Unterstützung ihr wart sowohl in der Uni als auch außerhalb der Uni immer da wenn es eng wurde.

Zu guter Letzt möchte ich mich bei meiner Familie und meinen Freunden bedanken die mich vielleicht mehr unterstützt haben als sie denken. Ein dickes Dankeschön geht an meine Schwester Sibylle Meyer fürs Korrigieren meiner etwas eigenwilligen englischen Kommasetzung. Danke an meine Eltern Gisela und Herbert Meyer und meine Freundin Verena Höfer für die viele Motivation und dass Ihr immer an mich geglaubt habt.